Influence of Nonlinear Irregular Wave Modeling on the Dynamic Response of an Offshore Wind Turbine

Master of Science Thesis

Author:	M.B. van der Meulen	
Committee:	Prof.dr. G.J.W. van Bussel	TU Delft - Chairman
	Prof.dr.ir. R.H.M. Huijsmans	TU Delft
	Ir. W.A.A.M. Bierbooms	TU Delft
	T. Ashuri, MSc.	Siemens Wind Power
	Ir. T. Subroto	Siemens Wind Power

October 24, 2012

TU Delft Delft University of Technology

- Confidential -

SIEMENS

Abstract

In the past decades, offshore wind energy has emerged as one of the most promising renewable alternatives to the traditional fossil sources of energy. Although the ocean has a vast potential, with higher wind speeds and lower turbulence levels than onshore, the required marine foundations make the realization of an offshore wind farm expensive. Partly, the high cost of a foundation is caused by the safety factor that is used to compensate for uncertainties in modeling the forces acting on the offshore wind turbine.

One way to reduce the safety factor, is to use a more accurate kinematic model for irregular waves. In order to simulate the fatigue life of an offshore wind turbine, traditional linear wave theory by Airy with Wheeler stretching is used to generate a large amount of stochastic irregular wave records. This method is accurate in deep water, but in the shallow water where offshore wind farms are sited, nonlinear interactions cause the waves to be sharp crested and flatter in the troughs. These nonlinear effects are expected to result in higher wave forces than what is currently modeled with linear wave theory, which is now compensated for by the safety factor. To be able to reduce the safety factor, the influence of using nonlinear rather than linear irregular waves on fatigue damage should be quantified.

This thesis project thus aims at quantifying the impact of a higher fidelity model for irregular wave kinematics, on the fatigue damage accumulation of a monopile supported offshore wind turbine. This requires a full set of load cases, comprising the entire range of sea states that can be expected during its lifetime, to be simulated by a dynamic response simulator. A hydrodynamic load calculation program was therefore developed, in which both the traditional linear wave theory and a 2^{nd}-order nonlinear model were implemented. It was assumed that the additional spectral power from the 2^{nd}-order model is small and hence does not need to be accounted for. The Morison equation with MacCamy-Fuchs correction for diffraction was used to obtain the hydrodynamic force on the monopile from the predicted wave kinematics. In order to make the research as realistic as possible, a recent wind farm in the German Bight with a water depth of 25 m. was chosen. The dynamic response simulations of the Siemens turbines and supporting structure was carried out by the aero-servo-elastic code BHawC.

The dynamic response simulations showed that the equivalent fatigue load in-

creases by maximally 4 to 6% when the 2nd-order wave model is used instead of the linear wave model. This load increase represents the additional fatigue damage that is accumulated during the entire lifetime of the offshore wind turbine. The maximum absolute equivalent fatigue load is achieved in the foundation, just below the seabed. The highest relative increase in fatigue load however, was observed in the vincinity of the mean sea level. It was found that the influence of nonlinear wave modeling is limited to the tower and the foundation, the blades and the nacelle did not show a significant difference in fatigue damage.

A closer inspection of the results reveiled that with nonlinear waves, a significantly larger portion of the fatigue damage due to fore-aft bending is accumulated when the turbine is idling. The reason for this increase is twofold. First, when the turbine is idling, aerodynamic damping is absent, which results in a poorly attenuated response. Second, some part of the idling time is spent in high wind speeds, which is accompanied by high waves. This results in a high degree of nonlinearity, and thus a significant load increase.

Furthermore, a sensitivity study was carried out. It was found that the choice for the wave spectrum has a large influence on the fatigue damage. Using standard linear wave theory, the maximum equivalent fatigue load due to fore-aft bending was found to increase by 10% if the Pierson-Moskowitz spectrum is used instead of a JONSWAP spectrum with peakedness of $\gamma = 3.3$. A value of $\gamma = 7$ on the other hand resulted in a 8% fatigue load reduction. The difference is contributed to the change in the amount of energy in the tail of the spectrum, in which the natural frequency of the support structure is situated. In both cases, the choice of the wave spectrum did not significantly influence the additional fatigue damage due to nonlinear wave modeling.

Also the influence of using different assumptions to account for a steady current was investigated. Instead of a current always co-flowing with the waves, the direction was alternated and a Doppler shift was accounted for rather than ignored. This did not result in significant differences in fatigue damage, neither due to linear nor from nonlinear waves. Furthermore, the effect of either one of the assumptions could not be isolated.

As expected, the 2nd-order model for irregular waves hence proved to result in higher fatigue loads. However, for the given wind farm the design would not be affected, since not fatigue life but ultimate loads from extreme waves were design driving. On the other hand, on a site in which the design is fatigue driven, a reconsideration of the safety factor is strongly advised when this model is used. Furthermore, this research shows that a proper wave spectrum selection, based on site-specific data, is important for a realistic fatigue damage estimation.

It was experienced that using the frequency-domain approach described in this report, the 2nd-order wave model performs very acceptably. Typical calculation times are only a small multiple of the time required for a linear wave calculation. In this light, the argument that this model would be too computationally demanding, is invalid. Henceforth, this method is a promising alternative for traditional linear wave theory.

Acknowledgements

When I decided to conclude my MSc. education in Aerospace Engineering with a graduation project on wave modeling for offshore wind turbines, I obviously must have raised some questions. Why on earth would you try to graduate without any prior knowledge of this topic at all? I first realized the challenges lying ahead of me when I was introduced to my future colleagues at the offshore Centre of Competence in the Siemens Wind Power office in The Hague. Only knowing the rather vague title of the project, explaining what I was set out to do already proved to be a difficult task. Looking back however, I am very pleased that I accepted this challenge and went for it.

First of all, I would like to sincerely thank David-Pieter Molenaar for offering the opportunity to graduate in collaboration with Siemens and allowing me in this great department. The enthousiastic group of people, which is said to surround you like a warm blanket, gave me a lot of inspiration and motivation to keep going. There are many people to thank within the department for their help and involvement in my work, but I would like to explicitly thank Toni for his enthousiastic supervision and his help to steer me in the right direction. Wouter, I think I owe you quite some *Audi-klusuren* for all the efforts to help me prepare and process the jungle of data from the BHawC simulations.

My special thanks go out to Turaj, who was my primary point of contact during this project. I was very pleased by the way you supervised my work, you really took the time to guide me and yet I got the complete freedom to shape this project the way that I thought would be best. Also, you constantly made sure that I put effort in the academic value of this work, rather than just focussing on the results.

Besides that, I would like to express my gratitude towards the large amount of MSc. students that lightened the burden of combining a student life with office hours. Tino, Marco, Roel, Renee, Jelle, Ouiam, Freek, Laurens, I am certainly going to miss the *academische bakkies*, but I'm sure we will still be able to spend some time drinking coffee and beer in the future.

From the TU Delft, I would like to thank Gerard van Bussel and Wim Bierbooms for taking me under their wing with this multidisciplinary project. Also, I thank Rene Huijsmans for sharing his knowledge and advise in an early stage of the project.

Of course I will not forget my friends and roommates, who were absolutely essential to take distance from my work from time to time. Writing this, I am already starting to miss the good old times in Delft, which in fact have not even passed!

Last but certainly not least: Pa, Ma en Suus, thanks very much for your confidence and support during all these months, but also during the past couple of years. I hope that for a change the result is worth forgetting your birthdays, but nonetheless the presents will still follow!

Finally, to answer the question I stated above: I guess I just caught this wave to surf in a different direction...

Michiel van der Meulen
October 2012

Contents

Abstract i

Acknowledgements iii

List of Figures viii

List of Tables xi

Nomenclature xiii

1 Introduction 1
- 1.1 Research motivation and objective . . . 1
- 1.2 Project approach . . . 2
- 1.3 Structure of the report . . . 3

2 Theoretical background 5
- 2.1 Introduction . . . 5
- 2.2 Wave kinematics . . . 6
  - 2.2.1 Describing the sea surface . . . 8
  - 2.2.2 Regular waves . . . 8
  - 2.2.3 Irregular waves . . . 9
  - 2.2.4 Linear wave theory . . . 16
  - 2.2.5 Nonlinear wave methods for regular waves . . . 24
  - 2.2.6 Nonlinear wave methods for irregular waves . . . 29
  - 2.2.7 Interaction of waves with a current . . . 35
  - 2.2.8 Coastal effects . . . 36
- 2.3 Wave kinetics . . . 38
  - 2.3.1 Steady viscous flow around a 2-dimensional cylinder . . . 38
  - 2.3.2 Unsteady viscous flow around a 2-dimensional cylinder . . . 43
  - 2.3.3 Flow around a 3-dimensional monopile due to wave motion 46
- 2.4 Offshore wind turbine response dynamics . . . 51
  - 2.4.1 Support structure dynamics . . . 51
  - 2.4.2 Support structure stiffness and damping . . . 54

2.5 Standards for offshore wind turbine design 56
2.5.1 Wave energy spectrum formulations 56
2.5.2 Wave kinematics model 57
2.5.3 Currents and still water level 58
2.5.4 Wave kinetics model 59
2.6 Trade-off for model selection 60
2.6.1 Kinematic wave model trade-off 60
2.6.2 Final remarks on the model selection 63

3 Model Formulation and Implementation 65
3.1 Introduction 65
3.2 Wave load calculation program structure 66
3.2.1 Wave kinematics module structure 67
3.2.2 Hydrodynamic load module structure 68
3.3 Model implementation 69
3.3.1 Kinematic model formulations 70
3.3.2 The Inverse Fast Fourier Transform (IFFT) 73
3.3.3 Using the IFFT with a Doppler shift due to a current 75
3.3.4 Fourier coefficients 78
3.3.5 MacCamy-Fuchs correction for diffraction 82

4 Verification 85
4.1 Introduction 85
4.2 Analysis of wave simulation results 86
4.2.1 Qualitative analysis of wave model output 87
4.2.2 Doppler-shifted frequency-domain method accuracy 89
4.3 Verification with an existing project 92
4.3.1 Description of the verification project 93
4.3.2 Comparison of Normal Sea State wave loads 93
4.3.3 Comparison of Severe Sea State wave loads 95
4.3.4 Comparison of dynamic response loads 96

5 Results and Analysis 101
5.1 Introduction 101
5.2 Overview of simulation cases 101
5.3 Results of dynamic response simulations 103
5.3.1 Comparison of linear and nonlinear waves 104
5.3.2 Sensitivity study 106
5.3.3 Case studies on deterministic waves 109
5.4 Analysis of simulation results 112
5.4.1 Influence of nonlinear irregular waves on fatigue 112
5.4.2 Sensitivity to wave modeling assumptions 113
5.4.3 Impact of low-quality deterministic wave modeling 114

6 Conclusion and Recommendations **115**
6.1 Introduction 115
6.2 Conclusion 116
6.2.1 Influence of nonlinear irregular waves on fatigue damage . 116
6.2.2 Sensitivity to wave modeling assumptions 117
6.2.3 Impact of poor deterministic wave modeling 118
6.2.4 Effect of nonlinear irregular waves on design 119
6.3 Recommendations for future work 119
6.4 Lessons learned during this project 121

A Linear wave theory derivations **123**
A.1 Equations of motion 123
A.2 Boundary conditions 125

B Deterministic extreme waves **127**
B.1 Analysis of a low quality deterministic wave 127
B.1.1 Influence of the MacCamy-Fuchs diffraction correction . . . 129
B.2 Nonlinear wave model: Fourier approximation 130
B.3 Insertion method 131
B.3.1 Identification of the optimal insertion point 132
B.3.2 Replacement surface elevation 133
B.3.3 Replacement wave kinematics 133

C Design Load Cases for Response Simulations **135**
C.1 Definition of the Design Load Cases 135
C.1.1 Number of wave load files per DLC 136
C.1.2 Definition of the sea environment 136

Bibliography **139**

Definitions **145**

List of Figures

2.1 Wave energy as a function of frequency and period 7
2.2 Creating an irregular wave by superposition 8
2.3 Definitions of a regular wave and the coordinate system in the space domain. 9
2.4 The discrete amplitude spectrum 11
2.5 Wave spectrum for a scenario in the North Sea 13
2.6 Creating a random wave record from a spectrum 15
2.7 Particle paths and velocities in a linear harmonic wave 20
2.8 Example of some kinematic stretching techniques 23
2.9 Range of applicability for regular wave theories 26
2.10 Stokes' second-order correction to a linear regular wave 27
2.11 Interaction components in a second-order nonlinear irregular wave 32
2.12 Phase modulation of a short wave riding a long wave 32
2.13 Overview of simplifications on Navier-Stokes equations 34
2.15 Lift and drag forces on a cylinder in a two-dimensional flow 39
2.16 Drag coefficient of a 2-dimensional cylinder as a function of the Reynolds number 40
2.17 Development of a boundary layer over a flat plate 41
2.18 Strouhal number of a 2-dimensional cylinder as a function of the Reynolds number 42
2.19 Response due to a vortex shedding induced lift force 48
2.20 MacCamy-Fuchs diffraction correction for C_M and phase 50
2.21 Regimes of dominant forces in hydrodynamic wave loading 51
2.22 Simple structural model of an offshore wind turbine 52
2.23 Response types of a mass-spring-damper system 53
2.24 Dynamic amplification factor and phase lag versus normalized frequency 54
2.25 Campbell diagram 55
2.26 Definition of water levels 59

3.1 Main program flowchart 66
3.2 Wave kinematics module flowchart 68

3.3 Wave kinetics module flowchart 69
3.4 Illustration of the Fourier Transform 73
3.5 Illustration of the aliasing effect 75
3.6 Doppler shift due to three different current magnitudes 76
3.7 Illustration of the frequency discretization 77
3.8 Doppler shift for evenly distributed apparent frequencies 78

4.1 Comparison of input and output wave spectra 87
4.2 2^{nd}-Order regular and irregular surface elevation 88
4.3 Comparison between time- and frequency domain results with Doppler shift 90
4.4 Comparison between time- and frequency domain results with Doppler shift 92
4.5 Comparison between time- and frequency domain results with Doppler shift 93
4.6 Verification of sea state simulations (NSS) 94
4.7 Verification of the overturning bending moment (NSS) 95
4.8 Verification of SSS deterministic wave simulations 96
4.9 The coordinate system used in BHawC 97
4.10 Eq. fatigue load distribution troughout support structure 97
4.11 Verification of equivalent fatigue loads 98

5.1 JONSWAP spectra used in sensitivity study 103
5.2 Influence of 2^{nd}-order waves on equivalent fatigue loads 104
5.3 Contribution of operation modes to fatigue damage accumulation . 105
5.4 Influence of wave spectrum with 1^{st}-order waves on fatigue damage 107
5.5 Influence of input spectrum on fatigue damage increase from 2^{nd}-order waves 108
5.6 Influence of assumptions in current modeling on fatigue damage . 108
5.7 Jump in deterministic wave load - effect on DLC 1.6 response . . . 109
5.8 Jump in deterministic wave load - effect on bending moment PSD . 110
5.9 Jump in deterministic wave load - effect on DLC 6.1 response . . . 110
5.10 Negative acceleration below deterministic wave - effect on DLC 6.1 response 111
5.11 Negative acceleration below deterministic wave - effect on bending moment PSD 112

A.1 Kinematic surface boundary condition 126

B.1 Example of a poorly inserted deterministic wave 128
B.2 Breaking limits of regular waves and an example wave 129
B.3 Influence of MacCamy-Fuchs correction on deterministic wave . . . 130
B.4 Insertion of a deterministic wave in a stochastic record 134

List of Tables

2.1 Flow characteristics in 2-dimensional cylinder flow 43
2.2 Base values for the drag coefficient C_D 60
2.3 Trade-off evaluation scores 61
2.4 Trade-off table for nonlinear regular wave models 62
2.5 Trade-off table for nonlinear irregular wave models 63
2.6 Selected models based on the trade-off 64

4.1 Bending moment power with and without Doppler shift 91
4.2 Bending moment power of 2^{nd}-order wave model with Doppler shift 94

5.1 Overview of simulation cases 102

C.1 Definition of Design Load Cases 138

Nomenclature

Latin symbols

a	wave amplitude	m
a	power law coefficient	-
A_{ij}, B_{ij}, C_0	coefficients in Fourier series	-
b	wave amplitude coefficient	m^2/s
B^+_{mn}, B^-_{mn}	transfer functions for amplitude of sum and difference components	-
c	wave speed / celerity	m/s
C	damping coefficient	Ns/m
C	normalizing factor (JONSWAP)	-
C_a	added-mass coefficient (2-dimensional flow)	-
C_d	drag coefficient (2-dimensional flow)	-
C_D	drag coefficient (3-dimensional flow)	-
$C_{D,eq}$	equivalent drag coefficient	-
$C_{D,0}$	primary structure drag coefficient	-
$C_{D,l}$	appurtenance drag coefficient	-
C_l	lift coefficient (2-dimensional flow)	-
C_m	inertia coefficient (2-dimensional flow)	-
C_M	inertia coefficient (3-dimensional flow)	-
$\hat{C}_M$	diffraction modified inertia coefficient (3-dimensional flow)	-
d	water depth	m
D	cylinder diameter	m
D	directional spreading distribution	$1/rad$
D^+_{mn}, D^-_{mn}	2^{nd}-order transfer functions	-
$\left.\begin{array}{l}(D/L)\\(\pi D/L)\\(kD/2)\end{array}\right\}$	diffraction parameter	-

e	relative roughness	-
E	expected value	$-$
E	Young's modulus	Pa
f	force	N
f	frequency	Hz
f	objective function	-
f_D	drag force per unit cylinder length	N/m
f_I	inertial force per unit cylinder length	N/m
f_L	lift force per unit cylinder length	N/m
$f_{Morison}$	resultant distributed force in flow direction in Morison equation	N/m
f_p	peak frequency	Hz
f_{st}	vortex shedding frequency of a body at rest	Hz
F	fetch	m
$\boldsymbol{F}$	body force vector	N
g	gravitational acceleration	m/s^2
h	water column below a wave through	m
H	wave height	m
H_1, H_{50}	wave height, 1 and 50 year reccurence period	m
H_∞	wave height at infinite water depth	m
H_d	wave height at finite water depth	m
H_{m_0}	significant wave height, estimated from wave spectrum	m
H_{MAX}	maximum wave height	m
$H_{\text{SWH}}, H_{\text{EWH}}$	severe/extreme wave height	m
H_S	significant wave height	m
i, j, n, m, p	indices	-
I	moment of inertia	m^4
J_1	1^{st}-order Bessel function of the first kind	m
k	empirical constant in wind-induced current model	-
k	wave number	rad/m
k	typical roughness height	m
K	gain factor	-
K	spring stiffness	N/m
K_{sh}	shoaling coefficient	-
$\mathcal{KC}$	Keulegan-Carpenter number	-
L	structure length	m
L	wave length	m

$\mathcal{L}$	length scale of a large eddy	m
m	magnitude of a complex function	-
m	Wöhler slope exponent	-
m_n	n^{th}-order spectral moment	-
M	moment	Nm
M	point mass	kg
M,N	number of terms in a summation	-
n	direction normal to a surface	-
N_b	number of rotor blades	-
$\mathcal{O}$	order of accuracy	-
p	pressure	Pa
p	probability	-
q	dynamic pressure	Pa
R	radius	m
R	reduced wave number	rad^2/m
$\mathcal{R}e$	Reynolds number	-
$\mathcal{R}e_{\mathcal{L}}$	Reynolds number of a large eddy	-
S	variance density	m^2/Hz
$\mathcal{S}t$	Strouhal number	-
t	time	s
t_p	discrete time vector	s
T	period of an oscillation	s
T_P	wave spectrum peak period	s
T_S	significant wave period	s
T_Z	zero-crossing wave period	s
$\boldsymbol{u}$	velocity vector	m/s
u, v, w	velocity components	m/s
$\dot{u}, \dot{v}, \dot{w}$	acceleration components	m/s^2
u_e	external flow velocity (outside boundary layer)	m/s
U	characteristic velocity	m/s
U_0	maximum velocity in a periodic cycle	m/s
U_{10}	wind velocity at 10m altitude	m/s
U_C	current velocity	m/s
$\widetilde{U}_C$	weighted depth-averaged current velocity	m/s
$U_{C,tide}$	tidal current velocity	m/s
$U_{C,wind}$	wind-driven current velocity	m/s
$\mathcal{U}r$	Ursell number	-

v_{ci}	cut-in wind velocity	m/s
v_{co}	cut-out wind velocity	m/s
V_b'	body volume per unit cylinder length	m^2
x, y, z	cartesian coordinates	m
$\dot{x}$	local monopile velocity	m/s
$\ddot{x}$	local monopile acceleration	m/s^2
x_{tr}	location of boundary layer transition point	m
X	Fourier coefficient	-
Y	single summation Fourier coefficient	-
Y_1	1st-order Bessel function of the second kind	m
z	argument of a complex function	rad
z_c	computational vertical coordinates	m
Z_{mn}^+, Z_{mn}^-	2nd-order wave kinematics amplitude	m/s

Greek symbols

α	dimensionless wave frequency	-
α	energy scale	-
β	dimensionless number for oscillating flow	-
β	dimensionless wave frequency parameter	-
β_l	appurtenance orientation angle wrt. incoming flow	rad
γ	peak-enhancement factor	-
ϵ	perturbation expansion parameter	-
η	sea surface elevation	m
θ	wave propagation direction w.r.t the x-axis	rad
μ	expected value	-
μ	mass per unit length	kg/m
ν	kinematic viscosity	m^2/s
ρ	density	kg/m^3
σ	peak-width parameter	-
ϕ	wave phase	rad
ϕ_{MCF}	phase-lag correction for diffraction (MacCamy-Fuchs)	rad
Φ	velocity potential function	m^2/s
Φ_s	scattered-wave velocity potential function	m^2/s
Φ_w	incident-wave velocity potential function	m^2/s
ψ	stream function	m^2/s
ψ	cosine/sine argument, short notation	-
ω	angular frequency	rad/s

Ω	curl	rad/s

Subscripts

$_0$	primary structure
$_\mathrm{A}$	apparent (wave frequency)
F	Fourier (deterministic wave model)
i, m, n	frequency component index
$init$	initial
j	propagation direction index
JS	JONSWAP
l	appurtenance
$_\mathrm{MCF}$	MacCamy-Fuchs
PM	Pierson-Moskowitz
$_\mathrm{R}$	relative (wave frequency)
R	replacement wave record
S	stochastic wave record

Superscripts

$^{(1)}$	First-order term
$^{(2)}$	Second-order term
$^{-}$	Difference contribution
$^{+}$	Sum contribution

Abbreviations

BHawC	Bonus Energy Horizontal axis wind turbine Code
CFD	Computational Fluid Dynamics
CPU	Central Processing Unit
DFSBC	Dynamic Free Surface Boundary Condition
DLC	Design Load Case
DNV	Det Norske Veritas
ESS	Extreme Sea State
HAT	Highest Astronomical Tide
HSWL	Highest Still Water Level
HWM	Hybrid Wave Model
IEC	International Electechnical Commission
(I)FFT	(Inverse) Fast Fourier Transform
JONSWAP	JOint North Sea WAve Project

KFSBC	Kinematic Free Surface Boundary Condition
LAT	Lowest Astronomical Tide
LHS	Left Hand Side
MSL	Mean Sea Level
NS	Navier-Stokes (equations)
NSS	Normal Sea State
PDF	Probability Density Function
PSD	Power Spectral Density
PM	Pierson-Moskowitz
RANS	Reynolds-Averaged Navier-Stokes (equations)
RHS	Right Hand Side
SSS	Severe Sea State
VIV	Vortex Induced Vibration

1 Introduction

1.1 Research motivation and objective

Offshore wind power is a rapidly growing industry, with hundreds of megawatts being installed at sea every year to accelerate the transition from the traditional fossil energy to clean renewables. Although wind turbines installed offshore benefit from the higher and steadier winds at sea, the marine foundations required to support the turbines still make offshore wind power more expensive than their onshore counterparts [1]. As the sea has a high potential for large scale wind energy projects, reducing the cost of the support structures is of fundamental importance to be able to realize offshore wind farms that can compete with traditional energy sources.

Currently, offshore wind farms are typically sited in coastal areas with water depths around or less than 30 m [2]. For these water depths, the monopile foundation type is by far the most popular. Due to the limited water depth, nonlinear effects cause the waves to become more sharp-crested while the troughs are flattened. Besides that, the magnitude of particle velocities and accelerations below the waves are higher due to the increased steepness of the wave. This in turn leads to higher hydrodynamic loads on the wind turbine support structure.

When designing an offshore wind turbine and its supporting structure, a distinction is usually made between ultimate loads due to extreme events and the accumulation of fatigue damage caused by cyclic loading of a lower magnitude. Design loads are estimated by an aero-servo-elastic simulation of the dynamic response in the time-domain, which uses hydrodynamic loads due to waves and currents as input. These hydrodynamic loads are usually estimated from wave kinematics using the Morison equation [3]. For the prediction of wave kinematics, several approaches are available. Again, a distinction between the simulation of fatigue and ultimate events is made. Ultimate load simulations are performed using a regular wave of a single frequency, while fatigue simulations employ irregular wave records with many frequency components of random amplitude and phase.

In the kinematic wave models used in offshore engineering, irregular waves are usually approximated with classical linear (Airy) wave theory [4]. Since this method only describes wave kinematics up to the mean sea level, Wheeler stretching [5] is often applied to redistribute the velocity and acceleration profiles up to the actual sea surface. This traditional approach, based on deep water experience from the oil and gas industry is accurate enough when the wave amplitude is small with respect to water depth, but in shallow water kinematics magnitudes are likely to be underestimated.

In order to be able to account for strong nonlinear effects in the highest waves that may occur during the lifetime of an offshore structure, a nonlinear regular wave model is commonly employed to model extreme events [6]. Such a deterministic extreme wave is calculated separately and then glued into a stochastic irregular wave record. By doing this, already some dynamics are already present in the wind turbine and the support structure when the deterministic wave passes by, which makes this empirical approach slightly more realistic.

Whereas in extreme wave events nonlinear effects are thus accounted for, a nonlinear model for random irregular waves is uncommon in engineering practice. To compensate for the lack of accuracy of linear wave theory in shallow water, a safety factor is therefore applied to obviate an underestimation of wave loads. Using a more accurate irregular wave model, the amount of uncertainty in fatigue load estimation could be lowered, which may lay the ground for a discussion on the safety factor that is used. Altough nonlinear irregular waves are expected to yield higher wave loads, the possible safety factor reduction might still result in a lower structural mass and hence reduced cost.

This potential cost reduction motivates the main objective of this thesis project: To quantify the influence of using nonlinear irregular wave models on the dynamic response of an offshore wind turbine. By analyzing the dynamic response loads, a prediction can be made on how nonlinearity in irregular waves will influence the fatigue loads.

1.2 Project approach

The project is started with a literature study on the hydrodynamics of wind turbines to classify different approaches to obtain wave kinematics and to compute the hydrodynamic force on the support structure. For this project, only monopile support structures will be considered. A round-up of the state-of-the-art of wave kinematics and kinetics shall be made, as well as an overview of more sophisticated nonlinear wave models that are available, from which the best candidate should be identified by a trade-off.

A hydrodynamic load calculation program for offshore monopile support structures is to be developed. The linear model for irregular wave kinematics, which is the current industry standard, should be realized to serve as a reference model. Besides that, the nonlinear model selected in the literature shall be developed. The reference wave model is to be verified by comparing the output of the model with certified wave loads created for an existing offshore wind farm.

To assess the influence of using nonlinear irregular wave models on fatigue life, the dynamic response of the wind turbine should be simulated. This requires a large number of simulations in the time-domain. These simulations will be performed by BHawC (Bonus Horizontal axis wind turbine Code), the aeroelastic simulation tool that has been developed in-house by Siemens to simulate dynamic response. A Siemens Wind Power turbine will be used for the dynamic response simulations. The sets of wave load files that are created with the hydrodynamic load model will be used as input for the BHawC simulations. Besides the comparison of offshore wind turbine fatigue life between linear and nonlinear wave models, a sensitivity study on variation of the input parameters is to be performed.

The research shall be concluded with an analysis of the results generated by the comparison and sensitivity study. Also, recommendations on the use and regions of validity of both linear and nonlinear wave models are to be given. Furthermore, a recommendation shall be made for future work and possible follow-up on this thesis project.

1.3 Structure of the report

In Chapter 2 an introduction to the theoretical aspects of the project is given. First, the theory of wave kinematics is treated and several methods of varying sophistication are discussed that are used to obtain the velocity field under a given sea surface elevation record. Second, the interaction of wave motion with a monopile support structure is studied and models are presented to compute the force acting on the structure. Furthermore, since ultimately the effects on the response of the offshore wind turbine need to be assessed, an introduction to structural response and dynamics is given. Finally, the calculation methods and procedures advised by design standards are discussed and a trade-off is made to identify the kinematic and kinetic models that are both accurate and have an acceptable computational load, such that plenty of simulation scenarios can be run and compared.

The selected methods are implemented in a computer program that is capable of simulating wave motion in linear and nonlinear irregular waves, and subsequently computes the hydrodynamic force due to the wave velocity. Chapter 3 describes the workflow of the code, the mathematical formulations used and details about the implementation. A method is proposed such that the Doppler shift due to a steady current can be accounted for, while using the efficient Inverse Fast Fourier Transform to perform the calculations in the frequency domain.

Chapter 4 describes the verification of the hydrodynamic load calculation program. First, the kinematic models are tested both qualitatively and quantitatively. Attention is also paid to the Doppler-shifted frequency-domain method proposed in Chapter 3. Second, the verification of an entire set of wave loads for a wide range of sea conditions is described. This verification has been performed using a Siemens wind farm project for which the hydrodynamic loads have been prepared by a third party foundation contractor.

The actual comparison between linear and nonlinear irregular wave modeling on offshore wind turbine fatigue life is described in Chapter 5. The required dynamic response simulations will be performed in BHawC, where the same input parameters will be used as for the verification project, in order to make a realistic comparison. Additionally, a sensitivity study is performed to investigate the influence of variation in the input parameters on wave nonlinearity and hence fatigue life.

The report finishes with a chapter on the conclusions that can be drawn from the results of the simulations. Also, recommendations for further development of the program and follow-up research are given. The chapter is concluded with a list of lessons learned during the project.

2 Theoretical background

2.1 Introduction

Challenged by the extreme environments in which offshore structures have to perform, engineers and scientists have developed various methods to deal with the prediction of the hydrodynamic forces that are created by the interaction of the structure with ocean waves. The problem can be divided into two branches of fluid mechanics: wave *kinematics* and *kinetics*. The way the water below the free surface interface is set into motion by a disturbance is the subject of study in wave kinematics, whereas in kinetics the hydrodynamic forces due to *interaction* of the fluid with the structure are considered.

A large variety of kinematic wave models and approaches to derive the force acting on the structure from the fluid motion is in use, depending on the required accuracy of the methods, the available computer time and of course the time available to implement the method. In order to understand the limitations of the methods, good knowledge of the physical principles and the impact of the assumptions that are made is essential. This chapter therefore introduces the basic theory behind wave kinematics and kinetics with the final aim to give an overview of the available methods and to discuss in which situations they can be applied, rather than going into the details of the methods itself.

The chapter is started with a treatment of wave kinematics in Section 2.2. The most important type of waves is identified and a statistical representation of the sea surface elevation is given. A very basic wave model based on linear theory is presented, together with a procedure to create an irregular random sea surface from standardized wave statistics. Next, various nonlinear methods for regular and irregular waves are discussed, including an introduction to the state-of-the-art methods based on Navier-Stokes solvers. Finally, the effects of a current and coastal features on the wave characteristics are presented.

The next section is devoted to kinetics, the study of hydrodynamic forces that result from the interaction of an object subject with fluid motion. As flow behavior is strongly dependent of the geometrical shape of the structure, this section is focussed on the most common type of offshore wind turbine foundation, the monopile support structure. To illustrate some fundamental features of the flow around a monopile, the section first treats a simple two-dimensional circular cylinder in a steady and unsteady, oscillating flow. The Morison equation is presented as a simple, yet popular empirical formula to estimate the in-line resistive force in an unsteady flow. Furthermore, attention is paid to factors that complicate the estimation of the time-dependent forces, such as vortex shedding and marine growth.

As the objective of this thesis is to quantify the influence of alternative wave models on the *dynamic response* of the offshore wind turbine, Section 2.4 provides a global introduction to general response dynamics. An overview is given of three characteristic types of responses due to harmonic loading, and important wind turbine specific excitations and natural frequencies of the components are discussed. Also, the influence of structural stiffness on the support structure design envelope and damping effects are treated.

In Section 2.5, the standards for the design of offshore wind turbines are discussed, with a distinct focus on the aspects that influence the hydrodynamic load on the support structure. Finally, in Section 2.6 the kinematic and kinetic models are compared and a trade-off is performed to determine which models are suitable to achieve the objective of this project.

2.2 Wave kinematics

One only has to shoot a glance at the ocean, to realize that the surface consists of many waves crossing their paths to create a chaotic, intriguing pattern. While most of the waves we observe by eye are generated by wind, ocean waves occur in many different forms. This is shown in Figure 2.1, where the energy of several classes of waves is shown as a function of their frequency and period. For the practical application of determining wave forces on an offshore structure, it is important to assess which classes of waves contribute significantly to the kinematics that are to be taken into account in the hydrodynamic model.

The *wind-generated wave* class is certainly the most important [8], as a high amount of energy is present in the frequency range in the order of 0.03-1 Hz, which coincides with the eigenfrequency of the monopile support structure ($\approx$ 0.3 Hz). If a series of waves happens to be in phase with one of the eigenfrequency modes of the support structure, the response may be amplified, thus increasing the structural loads severely.

Wind-generated waves can be further categorized into three types. A *wind sea* is created by the force exerted by wind on the sea surface, which is characterized by its random appearance. The small amplitude waves that are formed initially,

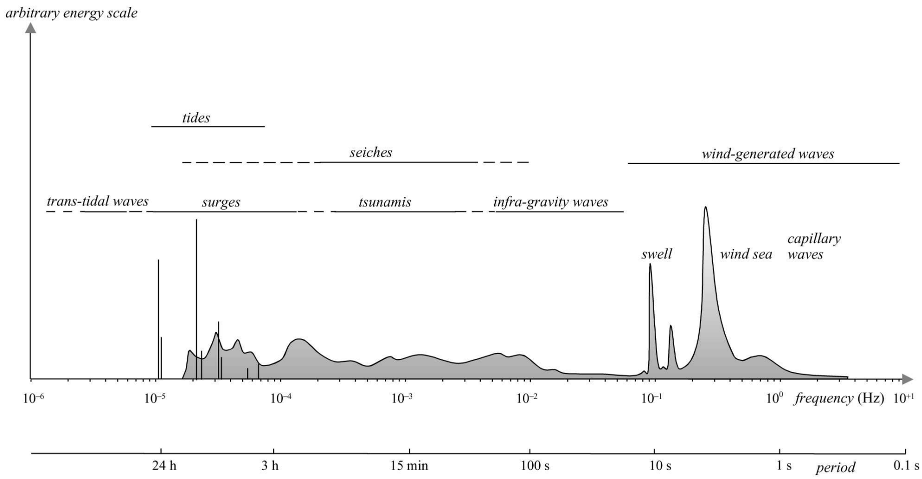

Figure 2.1: Wave energy as a function of frequency and period. [7]

called *capillary waves*, have a high frequency ($>$ 4 Hz) and are dominated by surface tension. As this type of wind-generated wave does not contain much energy, its effect on an offshore structure is minimal compared to longer wind-generated waves, and can therefore be ignored. Wind waves that have left the generation area create a smooth *swell*, which typically have a dominating long wave length. Furthermore, groups of wind-generated waves can form periodical *infra-gravity waves*, but their effect on a practical scale is negligible.

On the other end of the spectrum, *tides* are created by the gravitational force exerted by the moon and the sun, and the rotation of the earth. Depending on the geographical location, this low frequency wave may create strong tidal currents, which can be very significant compared to the kinematics of wind waves. Besides the tidal current, the change in sea level may have a noticeable effect on the resulting bending moment acting on the support structure. In this respect, *storm surges* need to be considered as well, as the local sea level rise due to a severe storm can be significant.

Whereas the waves described above are created by well predictable phenomena as the weather and tide, the remaining wave types in Figure 2.1 are harder or even impossible to predict, for various reasons. Besides, the effects are less pronounced as for the previously described waves. It is therefore a reasonable assumption that for this study, only wind-generated waves and tides need to be considered, where a storm surge is accounted for as an extreme load case.

2.2.1 Describing the sea surface

When considering wave loads on an offshore structure, a time record of the sea surface elevation is required such that for each moment in time the wave kinematics can be derived at the locations relevant for determining the wave forces. As information about tidal currents and water levels is usually available in reasonable detail, the problem reduces to finding the kinematics of wind-generated waves.

The most simplified way to describe a wave is by assuming it is a *regular* harmonic wave. This idealized wave can be made more realistic by creating an *irregular* sea surface through the addition of many independent harmonic waves of varying amplitude and phase, yielding the *random-phase/amplitude model*. An even more realistic model is created by giving each harmonic wave a propagation direction. An example of the sea state that is obtained from this superposition is shown in Figure 2.2.

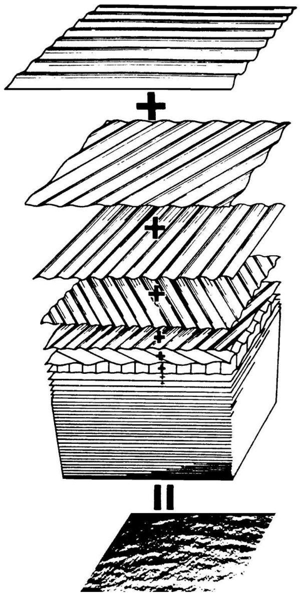

Figure 2.2: The superposition of many regular waves with varying amplitude, phase, frequency and propagation direction creates an irregular sea surface. [9]

2.2.2 Regular waves

Before moving on to a statistical description that can be used in a wave theory to create a sea surface, it is convenient to introduce some definitions. First, we assume a regular unidirectional sea, such that the surface elevation as a function of time, $\eta(t)$, can be modeled by a simple harmonic wave:

$$\eta(t) = a\cos(2\pi ft + \phi) \tag{2.1}$$

This simple wave has an amplitude a, a frequency f and a phase ϕ. The wave height H is defined as the difference in elevation between the wave *crest* and *trough*, and is twice the amplitude of the wave. A snapshot of such a regular harmonic wave and its definitions in the space domain is shown in Figure 2.3. A right-handed coordinate system is defined such that the wave propagates in the x-direction and the z-axis points toward the sky. Assuming the waves are unidirectional, the y-axis is fully parallel to the wave crests.

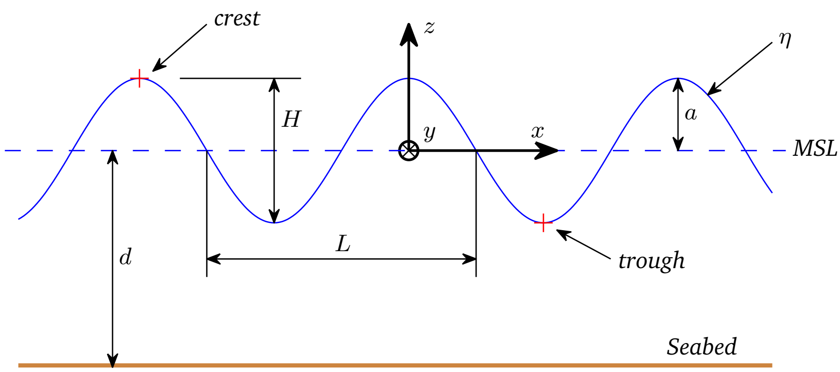

Figure 2.3: Definitions of a regular wave and the coordinate system in the space domain.

The wave period $T_Z(= 1/f)$ is commonly defined as the time passed between two consecutive up- or downward zero-crossings of the *Mean Sea Level* (MSL), which may be assumed constant in case the measurement period is small enough to neglect the influence of tides (typically 15-30 minutes) [7]. Alternatively, the wave period can be obtained from the wave length L and the wave speed or *celerity* c, using the relation $T_Z = L/c$.

It is quite obvious that by assuming a simple unidirectional regular wave, one will not create a realistic sea surface. Although the simplicity imposes certain limitations on the applicability of the regular wave model, it is also one of its major strengths, as will be shown in section 2.2.4. The regular wave model, combined with linear wave theory, can provide simple but powerful relations to describe the wave kinematics at any point.

2.2.3 Irregular waves

The first step towards a more accurate description of the sea surface is to consider an irregular wave model that is created by the summation of a large number of harmonic waves: the random-phase/amplitude model. The key assumption in this model is that the individual harmonic components are *linear*, such that they can be considered *independent* of one another and can thus be added together by superposition. The surface elevation for the irregular wave is now defined by:

$$\eta(t) = \sum_{i=1}^{N} \underline{a}_i \cos(2\pi f_i t + \underline{\phi}_i) \tag{2.2}$$

The index i represents a unique component of the discretized frequencies, which range from index $i = 1$ to N. The underlines indicate that the amplitude and phase of the wave are randomly drawn from the corresponding *probability density function* (PDF). In the random-phase/amplitude model, the phase is uniformly distributed, with a probability:

$$p(\phi_i) = \frac{1}{2\pi} \qquad \text{with:} \quad 0 < \phi_i < 2\pi \tag{2.3}$$

The amplitude on the other hand is characterized by a Rayleigh distribution with a frequency dependent expected value $\mu_i = E\{\underline{a}_i\}$, yielding the following probability:

$$p(a_i) = \frac{\pi}{2}\frac{a_i}{\mu_i^2} \exp\left(-\frac{\pi a_i^2}{4\mu_i^2}\right) \qquad \text{with:} \quad a_i \geq 0 \tag{2.4}$$

The expected values of the amplitude yield a unique Rayleigh distribution of the amplitude for each frequency. If all expected amplitudes are plotted against the frequency, the discrete *amplitude spectrum* is obtained (see Fig. 2.4). When a sufficient amount of frequencies is chosen in the correct range, a random time record of the sea surface elevation can be realized. It must be emphasized that the resulting wave record is stationary, so the influence of tides is not taken into account. Furthermore, it has been assumed that the harmonic components are completely independent, which is a reasonable assumption if interactions between the components are weak. In very shallow water or when waves are steep, this may no longer be the case, so one should be cautious when using the random-phase/amplitude model in coastal areas.

The wave energy spectrum

Although the amplitude spectrum can be employed to create a realistic irregular sea surface, the *variance density spectrum* or the *wave energy spectrum* is preferred. Rather than the amplitude, the expected value of the variance $E\{\frac{1}{2}\,\underline{a}_i^2\}$ is used in this spectrum, for two reasons. First, the variance is a commonly used statistical parameter, and second, the *energy* of a wave has been found to be proportional to the variance. Besides that, the wave energy spectrum can be made continuous rather than discrete by considering the limit case in which the difference between two frequencies approaches zero. This is desirable, because in nature all frequencies occur, rather than a finite number. The wave energy

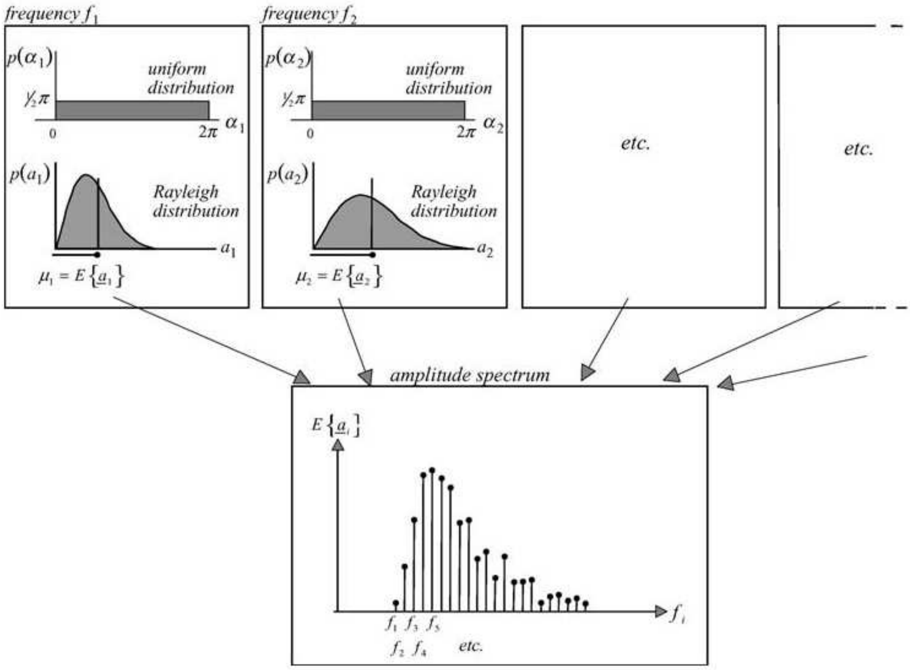

Figure 2.4: The discrete amplitude spectrum, constructed from many frequency component each with its unique expected value. [7]

spectrum $S(f)$ is now defined as:

$$S(f) = \lim_{\Delta f \to 0} \frac{1}{\Delta f} E\left\{\tfrac{1}{2}\,\underline{a}^2\right\} \tag{2.5}$$

The characteristics of the sea surface can be determined simply by drawing some conclusions from the wave energy spectrum. The narrower the spectrum, ie. the smaller the range of frequencies contributing to the variance, the more regular the waves are. The limit case occurs when only one frequency is present; then the spectrum consists of a single delta peak, and the wave is purely regular. On the other hand, a wide spectrum without obvious peaks represents a confused sea surface. The presence of a swell that has propagated from a distant storm can often be identified as a separate narrow-banded peak in the low frequency range.

Including the directional spreading

It must be noted that the wave energy spectrum described above, represents the time evolution of the surface elevation at a fixed location. In order to include the propagation direction with respect to the x-axis, θ, the surface elevation function has to be reformulated such that it includes the spatial coordinates x and y:

$$\eta(x, y, t) = a\cos(\frac{2\pi}{L}x\cos\theta + \frac{2\pi}{L}y\sin\theta - \frac{2\pi}{T_Z}t + \phi) \tag{2.6}$$

With the definitions of the angular frequency $\omega\,(= 2\pi/T_Z)$ and the wave number $k\,(= 2\pi/L)$, Eq. 2.6 can be reduced to:

$$\eta(x, y, t) = a\cos(kx\cos\theta + ky\sin\theta - \omega t + \phi) \tag{2.7}$$

The random-phase/amplitude model including the directional parameter can now be written as:

$$\underline{\eta}(x, y, t) = \sum_{i=1}^{N}\sum_{j=1}^{M} \underline{a}_{i,j}\cos\left(k_i x\cos\theta_j + k_i y\sin\theta_j - \omega_i t + \underline{\phi}_{i,j}\right) \tag{2.8}$$

The wave number and angular frequency can be assumed to be related through the so-called *dispersion relation* (see section 2.2.4), so they share the same index value i. The index j represents the discretized propagation directions. The wave spectrum can then be fully described by a two-dimensional frequency-direction model, with its wave energy spectrum defined as:

$$S(f, \theta) = \lim_{\Delta f\to 0}\lim_{\Delta\theta\to 0}\frac{1}{\Delta f\,\Delta\theta}E\left\{\tfrac{1}{2}\,\underline{a}^2\right\} \tag{2.9}$$

Integration of Eq. 2.9 with respect to θ from 0 to 2π again yields Eq. 2.5, the wave energy spectrum obtained earlier. In general, it makes sense to assume that the wave direction is spread more or less around the direction of the wind at the ocean surface, and do not travel against the wind. The shape of the directional spreading distribution $D(\theta)$ is therefore mostly approximated with the following $\cos^2\theta$ model:

$$D(\theta) = \begin{cases} \frac{2}{\pi}\cos^2\theta & |\theta| \leq 90^\circ \\ 0 & |\theta| > 90^\circ \end{cases} \tag{2.10}$$

The shape of the directional spreading has to be used with caution though, because the wave direction may vary substantially throughout the frequency range for example due to swell coming from a distant storm. This difference is illustrated by an example of the frequency-direction spectrum for a scenario in the North Sea, shown in Figure 2.5 on the top-right. The swell, besides having a different direction than the wind sea, clearly has a very profound propagation direction, whereas the wind sea has a much wider spreading. Integration of the frequency-direction spectrum with respect to the direction yields the 1-D frequency spectrum (bottom-right).

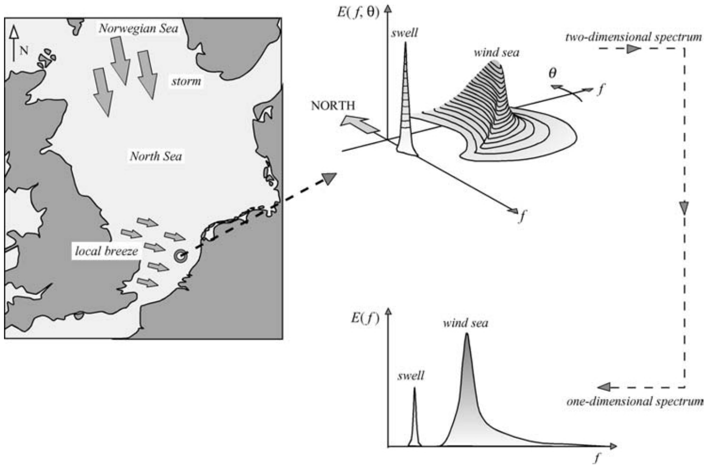

Figure 2.5: A scenario in the North Sea off the Dutch coast with a wind sea and an incoming swell. [7]

Significant wave height

As many harmonic waves with different phases and amplitudes are superposed in the random-phase/amplitude model, the crests and troughs no longer occur on the same elevation level. Also, the wave period is no longer a constant. It is therefore convenient to define a *mean wave height* and a *mean zero crossing wave period*, $\overline{H}$ and $\overline{T}_Z$ respectively. These are simply the averages of the wave heights and the time separations between consecutive downward zero-crossings:

$$\overline{H} = \frac{1}{N}\sum_{i=1}^{N} H_i \tag{2.11}$$

$$\overline{T}_Z = \frac{1}{N}\sum_{i=1}^{N} T_{Z_i} \tag{2.12}$$

In ocean engineering however, it is common practice to work with the *significant wave height*, H_S, which is defined as the mean of the highest one-third of waves:

$$H_S = \frac{1}{N/3}\sum_{j=1}^{N/3} H_j \tag{2.13}$$

The reason that the significant wave height is very popular is twofold: first, it is in much better agreement with visually estimated values of the mean wave height made in observations, and second, it can be estimated from the wave energy spectrum. Given a certain wave energy spectrum $S(f)$, the expression for the *estimated significant wave height* H_{m_0} reads:

$$H_{m_0} \approx 4\sqrt{m_0} \tag{2.14}$$

Here, m_0 is the *zeroth-order moment* of the spectrum, which in turn is defined by:

$$m_n = \int_0^\infty f^n S(f)\ \mathrm{d}f \tag{2.15}$$

As $n = 0$, the significant wave height is proportional to the area under the spectral curve.

Generalized spectral shapes for idealized conditions

The fact that an irregular wave can be constructed from the wave energy spectrum using the random-phase/amplitude model, has encouraged scientists to create generalized spectral shapes that can be tuned to match the desired conditions. The starting point for these spectra is an idealized situation in which a constant wind blows perpendicular off an infinitely long coastline, over infinitely deep water. Furthermore, the velocity of the wind U_{10}[1] is assumed to be constant and free of turbulence. Hence, the only remaining parameters that determine wave growth are the distance to the upwind coast, or *fetch* F, the duration t and gravitational acceleration g.

It was found that in a *young sea state* waves have a high growth rate, but when the celerity c approaches the wind speed, the development stops and the waves are considered *fully developed*. Furthermore, the spectrum has a *peak frequency* at which the wave energy is at its highest, Ω, which decreases as the waves develop. In the 60's, a general spectrum for fully developed wind seas was proposed:

$$S_{PM}(f) = \alpha_{PM} g^2 (2\pi)^{-4} f^{-5}\ \exp\left[-\frac{5}{4}\left(\frac{f_p}{f}\right)^4\right] \tag{2.16}$$

This spectrum is known as the Pierson-Moskowitz (PM) wave spectrum. In the expression for the PM spectrum, the relations for the *energy scale* α_{PM} and the peak frequency f_p can be expressed in terms of the significant wave height and the mean zero-crossing period. The PM spectrum describes a fully developed sea, but in reality, a change in wind velocity and direction is very likely along the fetch that is required to attain the fully developed state. Therefore, a spectrum for young sea states is desirable for many engineering cases. In the 70's, the JOint North Sea WAve Project (JONSWAP) took the *shape* of the PM spectrum and sharpened the peak with a peak enhancement function. The resulting spectrum has proven to be useful for both young seas and deep water influenced by storms

[1]The wind velocity at the surface is often expressed as U_{10}, the time-averaged velocity at 10 m above the surface.

[7]. The expression of the JONSWAP spectrum reads:

$$S_{JS}(f) = \alpha_{JS} g^2 (2\pi)^{-4} f^{-5} \exp\left[-\frac{5}{4}\left(\frac{f_p}{f}\right)^4\right] \gamma^{\exp\left[-\frac{(f-f_p)^2}{2\sigma^2 f_p^2}\right]} \tag{2.17}$$

Here, σ is a peak-width parameter and γ is a peak-enhancement factor, where σ depends on de frequency and the value of γ creates the desired peakedness of the spectrum. When the peak-enhancement factor is set to unity, the expression reduces to the PM spectrum (Eq. 2.16). The expressions for the PM and JONSWAP spectra presented here are very general, a more detailed and slightly different formulation of the spectra including the relations with respect to the characteristic wave parameters H_S and T_Z can be found in Section 2.5.

In case a significant swell component is present in the sea state, the single-peaked PM and JONSWAP spectra is not be the best representation of the spectral density of the sea surface elevation. A *two-peaked* spectrum as the Torsethaugen spectrum [10], taking into account both wind sea and swell, may in this case provide a better representation. The formulation of the Torsethaugen spectrum is less compact than the previously discussed spectra, therefore the reader is referred to for example DNV Recommended Practice [11] for more details.

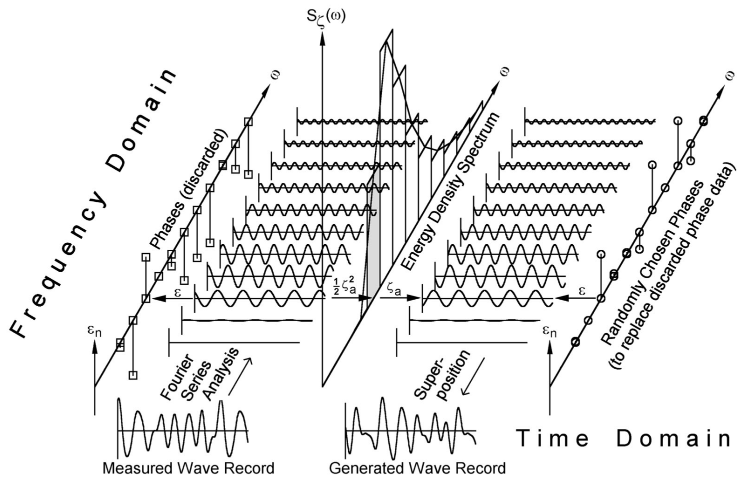

Figure 2.6: Creating a wave record by superposition of waves with varying frequencies and random phases. Although the generated record looks totally different from the measured record, the statistical properties are similar. NB: Spectral density, amplitude and phase are represented by the symbols S, ζ and ϵ respectively. [9]

Given a certain wave spectrum, a number of waves with discrete frequencies can be created by dividing the spectrum in *frequency bins*, where the amplitude depends on the spectral density of each frequency component, and the wave phases are uniformly distributed. The transformation from frequency domain (wave spectrum) to time domain (wave record) and the relation between both is shown in Figure 2.6.

2.2.4 Linear wave theory

In the previous section, methods were presented to create a wave record from generalized frequency spectra. With the sea surface elevation described as a function of time and space, the next step is to derive the kinematics that will ultimately be used to determine the forces acting on the wind turbine support structure. In this section, the linear wave theory, also known as *Airy* theory, is presented as a simple method to realize this step.

Equations of motion

To derive the kinematic relations, we start off with the basic equations of motion for a fluid, also known as the Navier-Stokes equations. The Cartesian coordinate system presented in Figure 2.3 is used, with the x-axis in the direction of the wave propagation, the y-axis pointing into the paper parallel to the wave crests, and the z-axis pointing upwards. The velocity field is described by the velocity components (u, v, w), or in vectorial notation $\boldsymbol{u} = \boldsymbol{u}(x, y, z, t)$.

Assuming the fluid is *incompressible*, the water density ρ is constant, such that conservation of mass in a volume is described by the *continuity equation*:

$$\boxed{\nabla \cdot \boldsymbol{u} = 0} \tag{2.18}$$

With the differential operator $\nabla = (\frac{\partial}{\partial x}, \frac{\partial}{\partial y}, \frac{\partial}{\partial z})$, the continuity equation thus states that the divergence of the velocity field is zero. A momentum balance is achieved in the *momentum equation*, in which the change in fluid momentum $\rho\boldsymbol{u}$ of a volume is required to be balanced by the body forces, pressure field and viscous forces acting on the fluid. The pressure field is described by the scalar field $p = p(x, y, z, t)$ and body forces are included in the vector $\boldsymbol{F}$. The momentum equation thus reads:

$$\boxed{\frac{\mathrm{D}\boldsymbol{u}}{\mathrm{D}t} = \boldsymbol{F} - \frac{\nabla p}{\rho} + \nu \nabla^2 \boldsymbol{u}} \tag{2.19}$$

Here, the diffusive viscous term contains the Laplace operator $\nabla^2 = \nabla \cdot \nabla \boldsymbol{u}$, which is the divergence of the gradient of the velocity field. The term is preceded by the kinematic viscosity ν. Furthermore $\frac{\mathrm{D}\boldsymbol{u}}{\mathrm{D}t}$ is the substantial derivative, containing the time derivative of the velocity field and a (nonlinear) advection term:

$$\frac{\mathrm{D}\boldsymbol{u}}{\mathrm{D}t} = \frac{\partial \boldsymbol{u}}{\partial t} + (\boldsymbol{u} \cdot \nabla)\boldsymbol{u} \tag{2.20}$$

Together, the system of conservation equations in Eqs. 2.18 and 2.19 are called the Navier-Stokes equations. A more detailed review of the Navier-Stokes equations and its simplified versions will be presented in the discussion of Computational Fluid Dynamics methods in Section 2.2.6. Analytical solutions for these equations exist only for very simple cases, so some idealizations are necessary to simplify the problem. First, the fluid is assumed to be *inviscid*, so the viscous term $\nu\nabla^2\boldsymbol{u}$ disappears from the right hand side (RHS) of Eq. 2.19. This assumption is valid as the wave lengths are long enough such that internal forces by viscosity can be neglected. Sea bottom friction due to viscosity can be ignored as well because the effects are limited to the boundary layer over the sea bed, which only has a very local effect on the water motion.

Second, the only external body force exerted on the fluid is assumed to come from the gravity potential, which acts in the vertical direction, such that $\boldsymbol{F} = g(z)$. Hence, the gravitational force only appears in the momentum equation in z-direction. Surface tension and the Coriolis force can be ignored if the wave lengths are in a range between a few centimeters to a few kilometers [7]. The momentum equation is thus simplified to:

$$\frac{\mathrm{D}\boldsymbol{u}}{\mathrm{D}t} = \boldsymbol{F} - \frac{\nabla p}{\rho} \tag{2.21}$$

For convenience, the equation is left in vectorial form for now, with the simplified body force vector $\boldsymbol{F} = g(z)$. Although the momentum equation has been simplified, it remains nonlinear. However, this is not a direct problem, as the boundary conditions that constrain the equation can be determined in nonlinear form as well, which is done later in this section. The advantage is that the nonlinearity of the equation and its boundary remains transparant as long as possible, up to the point when linearization is actually required in order to be able to solve the equations.

The continuity equation be rewritten in a convenient, alternative form. To achieve this, we assume the fluid to be free of *vorticity*, or *irrotational*:

$$\nabla \times \boldsymbol{u} = 0 \tag{2.22}$$

As vorticity is produced by viscous effects, the assuming irrotational flow is as reasonable as neglecting viscosity and its associated friction effects near the sea bed. The assumption is convenient, because it allows the velocity to be expressed in terms of a *velocity potential* $\Phi = \Phi(x, y, z, t)$, such that:

$$\boldsymbol{u} = \nabla\Phi \tag{2.23}$$

In other words, if a velocity potential function is found, the velocity components can be determined simply by taking the gradient of that function. Using the definition in Eq. 2.23, the continuity equation (2.18) can be rewritten in terms of the velocity potential:

$$\nabla^2\Phi = 0 \tag{2.24}$$

The velocity potential thus satisfies the Laplace equation (2.24).

Boundary conditions

To constrain the problem, boundary conditions need to be imposed to the problem. First, kinematic boundary conditions are considered, which will ensure that the fluid motions satisfy the physical constraints. At the sea bottom the vertical velocity $w = \partial\Phi/\partial z$ should be equal to zero, as the bottom is impermeable. This implies that at a the sea bottom $(z = -d)$ the following condition should be satisfied:

$$\frac{\partial \Phi}{\partial z} = 0 \qquad \text{at } z = -d \tag{2.25}$$

A second kinematic condition is imposed on the sea surface, the kinematic free surface boundary condition (KFSBC). Fluid particles should not leave the surface, hence the fluid velocity should be equal to the velocity of the sea surface:

$$\frac{\partial \Phi}{\partial z} = \frac{\partial \eta}{\partial t} + \frac{\partial \Phi}{\partial x}\frac{\partial \eta}{\partial x} \qquad \text{at } z = \eta \tag{2.26}$$

The third dimension, a variation in the y-direction can be included easily, but is discarded here for the sake of clarity. Besides the kinematic boundary conditions, a dynamic free surface boundary condition (DFSBC) is required, such that the wave is an unforced gravity wave. It follows from a derivation of the momentum equation 2.21 that the Bernouilli equation should be satisfied:

$$\frac{\partial \Phi}{\partial t} + \frac{1}{2}\left|\nabla\Phi\right|^2 + \frac{p}{\rho} + g\eta = 0 \qquad \text{at } z = \eta \tag{2.27}$$

For a detailed derivation of the boundary conditions, see Appendix A.

Linearization of the boundary conditions

Two of the three boundary conditions presented above contain nonlinear terms, for which obtaining an exact solution is only possible in some special cases. The trick therefore is to linearize the conditions by making assumptions such that the nonlinear terms can be neglected. By assuming the wave amplitude is small with respect to the wave length, the wave steepness H/L will also be small. The consequence is that a vector normal to the sea surface can be assumed to point purely in the z-direction. Besides, as the amplitude is small, the boundary condition has to be imposed at MSL, $z = 0$, rather than at the instantaneous level η. Boundary condition 2.26 can thus be linearized to:

$$\boxed{\frac{\partial \Phi}{\partial z} = \frac{\partial \eta}{\partial t}} \qquad \text{at } z = 0 \tag{2.28}$$

The kinematic boundary condition at the bottom (2.25) remains unchanged, but is repeated here for the sake of completeness:

$$\boxed{\frac{\partial \Phi}{\partial z} = 0} \qquad \text{at } z = -d$$

The dynamic surface boundary condition, Eq. 2.27, contains a nonlinear velocity term, which with the small amplitude approximation can be neglected. Furthermore, the pressure in Eq. 2.27 should be equal to the atmospheric pressure, to satisfy the free surface condition. In this case we take $p = 0$. The boundary condition then reduces to:

$$\boxed{\frac{\partial \Phi}{\partial t} + g\eta = 0} \qquad \text{at } z = 0 \tag{2.29}$$

Solution of the Laplace equation

As shown above, wave motion can be described by a velocity potential, which is gouverned by the Laplace equation 2.24 and satisfies the dynamic (2.29) and the two kinematic (2.25,2.28) boundary conditions. Through separation of variables (see for example [12]), one of the solutions that can be derived is that of a propagating wave:

$$\Phi = \frac{ag}{\omega}\frac{\cosh k(z+d)}{\cosh kd}\sin(kx - \omega t + \phi) \tag{2.30}$$

Substitution of the velocity potential in the dynamic surface boundary condition (2.29) yields the surface elevation for a propagating harmonic wave:

$$\eta(x,t) = a\cos(kx - \omega t + \phi) \tag{2.31}$$

The fluid particle velocity components can now be found from the gradient of the velocity potential:

$$u = \frac{agk}{\omega}\frac{\cosh k(z+d)}{\cosh kd}\cos(kx - \omega t + \phi) \tag{2.32}$$

$$w = \frac{agk}{\omega}\frac{\sinh k(z+d)}{\cosh kd}\sin(kx - \omega t + \phi) \tag{2.33}$$

Differentiation of the velocity components with respect to time gives the acceleration of the fluid particles:

$$\dot{u} = agk\frac{\cosh k(z+d)}{\cosh kd}\sin(kx - \omega t + \phi) \tag{2.34}$$

$$\dot{w} = -agk\frac{\sinh k(z+d)}{\cosh kd}\cos(kx - \omega t + \phi) \tag{2.35}$$

In deep water where $d/L > 1/2$, the fluid particles follow a circular path with a velocity that decays exponentially for increasing depth. In shallow waters where $d/L < 1/20$, the particle paths are much more restricted to horizontal motion, and the velocity experiences less variation magnitude with depth. In the intermediate regime, $1/20 \leq d/L \leq 1/2$, the particles follow an elliptic path [13]. An illustration of the particle paths and the corresponding velocities is given in

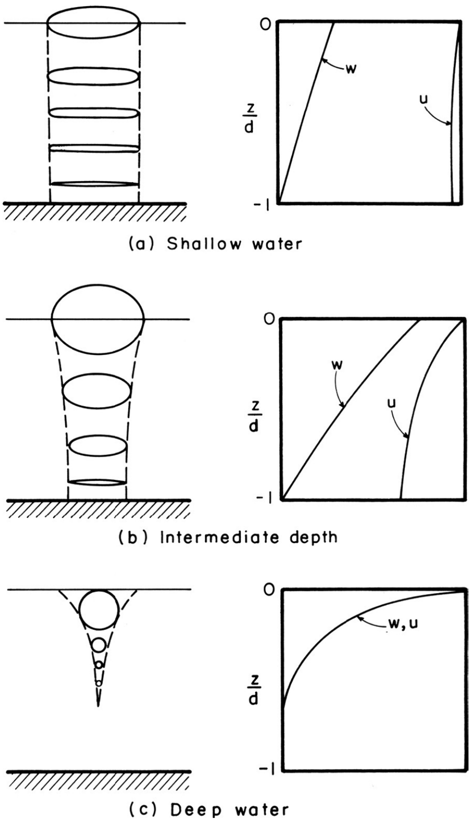

Figure 2.7: Particle paths (left) and velocities (right) in a linear harmonic wave, for different depths. [13]

Figure 2.7. Furthermore, it can be concluded that the particle accelerations have a $90°$ phase lead compared to the velocities.

Another useful property that can be derived is the *dispersion relation*, which is obtained when the velocity potential is substituted in the Laplace equation, Eq. 2.24:

$$\omega^2 = gk \tanh kd \tag{2.36}$$

The wave celerity can be expressed in terms of the wave number, using $c = L/T_Z = \omega/k$ and the dispersion relation:

$$c = \sqrt{\frac{g}{k} \tanh kd} \tag{2.37}$$

In deep water, where $\tanh kd \to 1$, this expression shows that the celerity is related to the wave number as $c = \sqrt{\frac{g}{k}}$. In other words, waves with a large wave length (low k) will travel faster than shorter waves. As depth decreases, the dispersion relation shows that the constant frequency forces the wave number to increase. Finally, in very shallow water, the linear approximation $\tanh kd \approx kd$ is allowed, such that the wave celerity no longer depends on the wave number or frequency but solely on the water depth: $c = \sqrt{gd}$ [13].

Extending the velocity profile

In order to linearize the boundary conditions, the amplitude of the wave was assumed small. This implies, that the velocities at the surface are actually described on MSL, without any variation in elevation. On the actual surface level however, measured kinematics have shown to deviate from linear theory predictions significantly, particularly near the wave crest and trough. Furthermore, when the interaction of waves with a structure is considered, the error in the hydrodynamic force distribution that is made by using the kinematics on a fixed sea level may be significant if the wave height is substantial compared to the height of the structure. These two aspects illustrate the need for a modification of the linear wave theory such that the prediction provides a better match with measurements and describe the velocities at the actual elevation level.

A collection of popular velocity extension methods is presented below. As the sea surface happens to be the region where both the uncertainty of the predictions and the magnitude of the kinematics are at its highest, the absolute error is likely to be significant. It should therefore be stressed that although the modified predictions are more accurate than linear theory, neither of the methods discussed here are capable of describing the kinematics fully accurate.

- **Constant extension**
  This method is also referred to as vertical stretching. It simply assumes that the velocity at any point above MSL is equal to the velocity at MSL, and below MSL linear theory is applied without change:

  $$u(x,z,t) = \begin{cases} u(x,z,t) & z \leq 0, \\ u(x,0,t) & 0 \leq z \leq \eta. \end{cases} \tag{2.38}$$

  Due to the simplicity of the method, this approximation is quite popular in the offshore industry, despite the large errors that have been observed in comparison with experiments [14].

- **Linear extrapolation**
  The linear extrapolation method assumes that the velocity profile above MSL can be approximated by using the velocity gradient $\frac{\partial u}{\partial z}$ at MSL for a linear extension of the profile. Below MSL, the velocities predicted by linear theory are used:

  $$u(x,z,t) = \begin{cases} u(x,z,t) & z \leq 0, \\ u(x,0,t) + z\left(\frac{\partial u}{\partial z}\right)_{z=0} & 0 \leq z \leq \eta. \end{cases} \tag{2.39}$$

  In comparisons with measurements, the linear extrapolation method has shown to severely overpredict the wave kinematics near the crest and to slightly underpredict the velocity near the trough [14].

- **Wheeler stretching**
  A very popular method for velocity profile stretching has been developed by Wheeler [5], based on measurements on wave elevation time series. Instead of extending the velocity profile like the methods presented above, the velocity at an elevation z is replaced by the velocity at a computational, stretched coordinate z_c:

$$u(x, z, t) = u(x, z_c, t) \qquad\qquad 0 \le z \le \eta \tag{2.40}$$

  where

$$z_c = \frac{d(z - \eta)}{d + \eta} \tag{2.41}$$

  The results that are achieved with the Wheeler stretching method are more accurate than the extension methods presented above, although the method has a tendency to underestimate the kinematics, particulary close to MSL [15]. Despite this imperfection, the straightforward implementation and use of the method has lead to wide acceptance of Wheeler stretching in the offshore industry. An example of Wheeler stretching, compared with linear and constant extension is presented in Figure 2.8.

- **Delta stretching**
  The Delta stretching method [16] was devised as an alternative to reduce the excessive overpredictions of linear extrapolation, and is basically an empirical average of a Wheeler stretching and a linear extrapolation. Although an improvement is achieved over the extension method, the results are less satisfactory than using Wheeler stretching.

- **Gudmestad stretching**
  This method is a second-order expansion of a stretching method that was proposed by Chakrabarti [17], first derived by Gudmestad and Connor for regular waves [18] and later extended to irregular waves by Gudmestad [19]. The reader is referred to the respective literature for details about the approach and the equations involved. For regular waves, the Gudmestad approach performance is very well comparable to the Wheeler stretching method, whereas for irregular waves the second-order stretching method yields slightly better results [14]. The method however requires more effort to implement than the straightforward Wheeler stretching method.

The Wheeler method is generally conceived to be the preferable method, due to its robustness and the acceptable accuracy of the results [15]. In irregular linear wave theory, Wheeler stretching is less accurate and Gudmestad stretching may improve the solution slightly. For a comparison of several velocity extension methods with measurements, the reader is referred to the detailed discussion by Gudmestad [14].

Although irregular waves can be modeled conveniently using linear theory with a stretching technique, the solution suffers from *high frequency contamination*, oscillations in the kinematics near the wave crest due to the contribution of high frequency components in the hyperbolic terms of the velocity expressions [20]. This effect can be attenuated to some extent by introducing a low-pass filter which blocks higher frequencies that contaminate the solution, but it should be stressed that the stretching methods are engineering approximations that are not based on hydrodynamic theory.

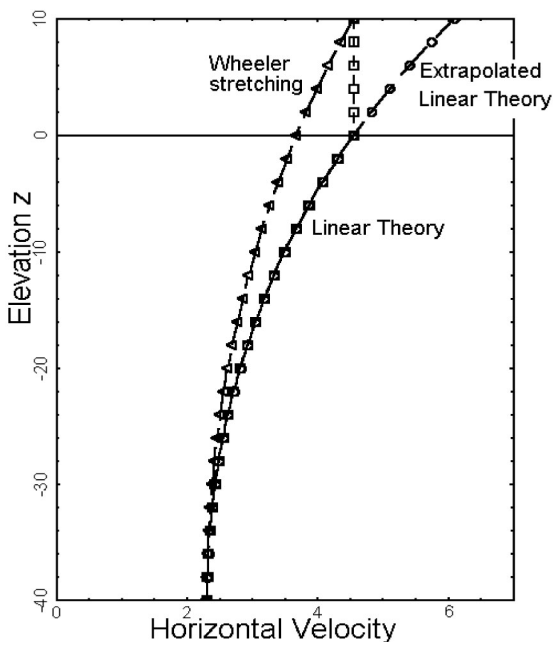

Figure 2.8: Example of some kinematic stretching techniques applied to linear theory. Constant extension (□) and linear extrapolation (○) only extend the velocity profile from MSL to surface level, whereas Wheeler stretching (◁) redistributes the velocities from linear theory on a stretched coordinate. [9]

Wave description using a Lagrangian coordinate system

So far, the methods to determine kinematics from linear irregular waves employed an *Eulerian* description of the flow field, which means that the motion is observed from a coordinate system that is fixed in space. Alternatively, the flow field can be considered from a *Lagrangian* perspective, where the coordinate system moves and deforms with the fluid and as such, the free surface is fixed. Whereas the Eulerian description provides the kinematic properties at known and fixed locations, the position of the Lagrangian solution has to be derived, which fairly complicates the method.

Although retreiving the kinematics to an Eulerian coordinate system is a challenge, the Lagrangian description is attractive because the stretching techniques that are required in linear irregular wave theory to obtain a solution at finite amplitude and the high frequency contamination of the solution can be avoided. Gjøsund [21] derived a linear Lagrangian wave model for irregular waves, that is correct to first order in wave amplitude at any surface elevation. The method is based on a linearization of the inviscid Euler equations, which contrary to the potential flow equations used in linear wave theory are rotational. To obtain the solution in an Eulerian frame of reference, Gjøsund suggests an iterative scheme.

In experiments, the kinematics obtained by the Lagrangian method are in good agreement with measurements, and the method seems to outperform irregular linear wave theory with Wheeler stretching [21].

2.2.5 Nonlinear wave methods for regular waves

Currently, offshore wind farms are mostly sited in coastal areas with water depths smaller than 30 meters, with only a few exceptions [2]. In deep water and when the wave steepness H/L is small, a wave can be described by the linear theory presented above with reasonable accuracy, whereas in the relatively shallow water where offshore wind farms are located waves tend to become more sharp crested with flatter troughs and slightly higher crests, violating the small amplitude and steepness assumption of linear wave theory. Shallow water waves therefore are no longer harmonic but periodic, where the sea surface spends most of its time below the MSL, with short but sharp upward excursions. Besides the change in shape, the fluid particles no longer travel on closed ellipsoid orbits like in linear theory, but they gradually drift in the direction of the wave propagation. This phenomenom is known as Stokes drift.

The main difficulty with gravity waves is found at the free surface interface, where nonlinear kinematic and dynamic boundary conditions (Eqs. 2.26 and 2.27) have to be satisfied. Hence the exact solution is unknown, which causes a certain degree of uncertaincy exists towards the free surface, which is especially inconvenient considering the fact that the wave kinematics reach their maximum values near the surface.

For regular nonlinear waves, several wave theories have been developed that can be used for various types of waves when linear wave theory is of insufficient accuracy. Better fidelity can be achieved by applying higher order corrections to the wave profile, which is the basic idea behind the *Stokes* and *cnoidal* theory. A more recent attempt to describe nonlinear regular waves is a numerical *Fourier approximation method*, which was developed with the objective to find a more generally applicable method, avoiding the regions of uncertainty of the Stokes and cnoidal theories.

In contrast to linear theory, which because of the simplifications is easy to grasp and implement in engineering practice, nonlinear wave theories are far less transparent. Often, this is due to the confusing amount of coefficients and equations involved, and the variety in mathematical formulation and definition of reference frames, dimensionless variables and perturbation parameters that exist in literature. After the Stokes and cnoidal theories had been extended to fifth order more accurate results were obtained, leading to more consistent formulation of the methods, as described in literature by Fenton and Goodwin *et al.* [22, 23].

In the discussion of nonlinear theories for regular waves, a *steady* wave train is considered, which means that the shape of the wave does not evolve in time. This means that any high frequency waves that are superposed as higher-order corrections are locked onto the profile of the 'primary' wave and propagate with the same wave speed. Below, a brief description of the three nonlinear regular wave methods is given.

Stokes theory

In order to create a periodic wave profile that features a sharp crest and a flat trough rather than a purely harmonic shape, Stokes (1847) proposed adding a perturbation correction of second-order to a harmonic regular wave, with a frequency and wave number twice that of the original wave. Fenton [24] further extended the method to fifth-order such that the solution remains of acceptable accuracy towards the wave breaking limit. The expression for the sea surface elevation expanded to N$^{\text{th}}$-order is given as follows:

$$k\eta(x,t) = kd + \sum_{i=1}^{N} \epsilon^i \sum_{j=1}^{i} B_{ij} \cos j(kx - \omega t) + \mathcal{O}(\epsilon^{N+1}) \tag{2.42}$$

In this approximation, $\epsilon = kH/2$ is a small parameter based on the nondimensional amplitude of the wave and B_{ij} are amplitude coefficients, for which the expressions can be found in literature [24]. Like for linear wave theory, a velocity potential can be derived, which will yield the velocity components by taking the gradient of the function. For an N$^{\text{th}}$-order Stokes theory, the velocity potential in the $(x,z)-\mathrm{plane}$ reads:

$$\phi(x,z,t) = U_C x + C_0 \left(\frac{g}{k^3}\right)^{1/2} \sum_{i=1}^{N} \epsilon^i \sum_{j=1}^{i} A_{ij} \cosh jkz \sin j(kx - \omega t) + \mathcal{O}(\epsilon^{N+1}) \tag{2.43}$$

In the above formulation, A_{ij} and C_0 are coefficients and U_C represents the current velocity. The coefficients can be calculated using the water depth d, the wave height and wave length. In general, the wave number k is not known and has to be found numerically or by an approximation provided that the wave period and height, depth and current velocity are known. With the wave number known, the value of the expansion parameter ϵ can be calculated, after which the surface elevation and velocity potential can be found. As the collection of coefficients and equations is quite extensive, they will not be stated here, but the reader is referred to [24] or [22] instead.

It must be noted that for the shallow water limit ($kd \to 0$), the coefficients of the higher order terms behave as $(kd)^{-3}$, which means that these terms will dominate the solution. Because of this inconvenient complication, the *effective* expansion parameter of the higher order terms has been found to be $\epsilon/(kd)^{-3}$ rather than ϵ [24]. Therefore, in shallow water the Stokes method tends to become inaccurate and one should carefully monitor both ϵ and the effective expansion parameter to make sure that both remain small. The range of applicability of the Stokes wave is therefore limited by the shallowness of the water and the breaking limit of the wave, as shown in Figure 2.9.

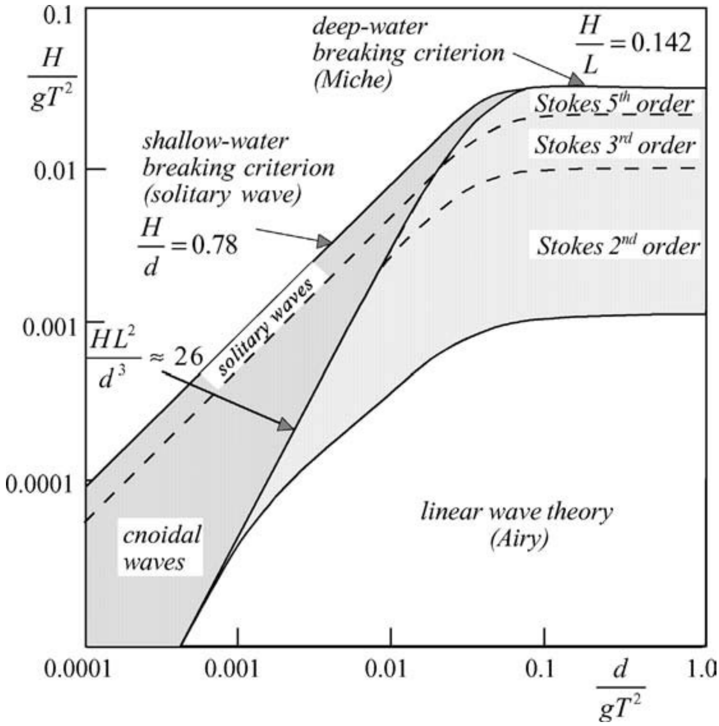

Figure 2.9: Range of applicability for regular wave theories. [7]

The Stokes correction to second-order is visualized in Figure 2.10. A regular harmonic wave is corrected with a wave that has twice the frequency of the primary wave, and has an amplitude that is substantially smaller than that of the primary wave. Provided the expansion parameter is small, higher-order corrections will have progressively smaller amplitudes and thus only have a small contribution to the final shape of the wave.

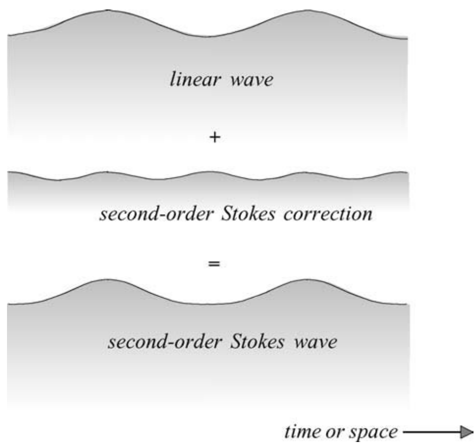

Figure 2.10: Adding a perturbation correction of twice the frequency of the primary linear regular wave yields the second-order Stokes wave. [7]

Cnoidal theory

The second regular nonlinear wave theory that is considered here is cnoidal theory, developed by Korteweg and De Vries in 1895. The Jacobian elliptic function $cn(z|m)$ is the basis for the expressions of the wave characteristics, hence the name *cnoidal theory*, where z is the argument and m the magnitude of the cn-function. Fenton [25] showed that the effective expansion parameter in his fifth-order cnoidal theory is H/hm, in which h is the height of the water column below the trough. In the limit $m \to 1$, the wave throughs become infinitely long and the wave solution corresponds to the *solitary* wave. The short wave limit on the other hand introduces problems, as the effective expansion parameter can be shown to be proportional to $(d/L)^2$ [22], due to which especially in deep water the higher order terms will dominate the solution, leading to errors in the approximation. In this case, Stokes theory yields better results and therefore is the preferred method in the short wave limit.

As the equations involved in cnoidal theory are littered with a large amount of coefficients, stating the equations may lead to confusion rather than better understanding of the method. Hence for more details, the reader is referred to Fenton [22], where the most up-to-date modifications to the cnoidal theory are presented. More information about Jacobian elliptic functions can be found in [26].

Fourier approximation method (stream function)

Both the Stokes and cnoidal theories described above use coefficients that are obtained by analytical approximations. Although these theories yield good results in their range of applicability, the two methods lack a uniform validity and thus have to be used as complementary methods in order to be able to describe most types of weakly nonlinear waves. A numerical alternative that has a larger range of applicability, is a collection of methods that use Fourier approximation techniques. Similar to the Stokes theory approach a Fourier series expansion is used to correct the sea surface profile, but rather than deriving analytical approximations for the Fourier coefficients, they are approximated numerically by substitution of the series expansion in the nonlinear boundary conditions.

Whereas Chappelear [27] used the familiar velocity potential function in his Fourier approximation method, Dean [28] derived a simpler set of equations by using the *stream function* $\psi(x,z)$ instead, which is valid if the flow is two-dimensional and incompressible. The velocity components can be found by taking the curl of the stream function:

$$\boldsymbol{u} = \nabla \times \psi \tag{2.44}$$

The original equations of motion and the boundary conditions (Eqs. 2.24-2.27 only change slightly using the stream function. If the fluid is assumed irrotational, like in potential flow the Laplace equation has to be satisfied:

$$\nabla^2 \psi = 0 \tag{2.45}$$

The kinematic boundary conditions become:

$$\frac{\partial \psi}{\partial x} = 0 \qquad \text{at } z = -d \tag{2.46}$$

$$\frac{\partial \psi}{\partial x} = \frac{\partial \eta}{\partial t} + \frac{\partial \psi}{\partial z}\frac{\partial \eta}{\partial x} \qquad \text{at } z = \eta \tag{2.47}$$

And the dynamic boundary condition reads:

$$\frac{\partial \psi}{\partial t} + \frac{1}{2}\left|\nabla \psi\right|^2 + \frac{p}{\rho} + g\eta = 0 \qquad \text{at } z = \eta \tag{2.48}$$

For consistency throughout this discussion, the equations are considered in a *stationary* frame of reference, whereas in literature a moving frame of reference that is locked to the wave is sometimes used, which allows the unsteady time derivative in 2.48 to be omitted. An example of a stream function representation of the equations of motion considered from a moving reference frame can be found in [29].

As Fourier series are very capable of approximating period quantities, a series expansion of the stream function is introduced to obtain a higher-order solution. Rienecker and Fenton [29] approached the problem by approximating the solution of the nonlinear equations using Newton's method, for which the numerous equations will not be shown here to keep the discussion concise. A more simple approach including a Fortran computer program is presented in [30]. Recently, this numerical Fourier approximation method has been implemented in C++ by

Fenton [31]. Due to the use of a stream function rather than a velocity potential, the Fourier approximation method is often referred to as the stream function method.

Results show that Fouries series approximations are capable of giving accurate solution with 10-20 terms, although higher waves may converge to the wrong solution. This inconvenience can be solved by using a sequence of wave height steps to achieve the desired height [22]. Considering the computer power available nowadays and the large region in which the Fourier series approach can be applied, the method is an attractive alternative to the analytical Stokes and cnoidal theories.

Applicability of regular nonlinear wave methods

The range of applicability of each method depends on the wave steepness and water depth, as is shown in Figure 2.9. For waves that are short relative to the water depth Stokes theory is accurate, while in shallower water the method fails and cnoidal theory gives better results. Towards the demarcation line that separates the cnoidal and Stokes theory regimes both methods lose a small amount of their accuracy [22] and converge more slowly. The Fourier approximation method can be used in a wider range that overlaps both previous methods, only in very shallow water cnoidal theory is to be used instead. As an aid to characterize the wave, the Ursell number is often used:

$$\mathcal{U}r = \frac{\text{“Steepness”}}{\text{“Relative depth”}} = \frac{H/d}{(d/L)^2} = \frac{HL^2}{d^3} \tag{2.49}$$

Although the value of the Ursell number can give useful insight into the character of the wave, the number itself does not give any warning that the wave breaking criteria (Fig. 2.9) are exceeded. Therefore, the complete set of validity criteria corresponding to each method should be carefully monitored.

2.2.6 Nonlinear wave methods for irregular waves

The most realistic description of the ocean surface and kinematics is realized if the waves can be represented by an irregular model that accounts for nonlinear interaction effects, most notably the sharper crests and flattened troughs. Linear irregular wave theory provides a reasonable approximation, but the high frequencies need to be omitted in order to limit the error. Unfortunately, the extension to include nonlinearity is not straightforward and many different approaches are possible, which is the reason for the existence of a large variety of methods. The second-order perturbation model is the most basic amongst them, and is discussed here together with a few more sophisticated methods. Furthermore, state-of-the-art numerical wave tank approaches which employ the recent advances in computational fluid dynamics are discussed.

Second-order perturbation model

A nonlinear irregular wave model that has found wide acceptance is a second-order perturbation extension of linear wave theory by Sharma and Dean [32], still under the hypothesis of irrotational and inviscid flow. Although this method has been derived for directional waves, the presentation here is limited to unidirectional waves, to keep the expressions as concise as possible. The modified sea surface elevation η is obtained by adding a second-order perturbation $\eta^{(2)}$ to the first-order surface $\eta^{(1)}$:

$$\eta = \eta^{(1)} + \eta^{(2)} \tag{2.50}$$

The first-order approximation of the sea surface level was presented in the discussion of linear irregular wave theory, and is repeated here in unidirectional form:

$$\eta^{(1)} = \sum_{i=1}^{N} a_i \cos(\psi_i) \tag{2.51}$$

The term in the cosine has been abbreviated to $\psi_i = k_i x - \omega_i t + \phi_i$, not to be confused with the stream function. Furthermore, the term to indicate that η is a function of (x, t) and the underlines that was used earlier to indicate that the amplitudes and phases are drawn from a PDF, have been omitted. The second-order *mode-coupled* expansion of the wave surface reads:

$$\eta^{(2)} = \sum_{n=1}^{N} \sum_{m=1}^{N} a_n a_m \left\{ B_{mn}^{-} \cos(\psi_n - \psi_m) + B_{mn}^{+} \cos(\psi_n + \psi_m) \right\} \tag{2.52}$$

where B^+ and B^- represent the positive and negative interaction kernels of the sum- and difference contributions respectively, also referred to as super- and subharmonics. Expressions for the velocity potential and kernels are omitted here for the sake of clarity and can be found in literature, eg. [32] or [33].

The interactions can be understood by considering a sea state composed by two wave components of almost identical frequencies. In this case, the positive interaction term has a frequency approximately twice of the first-order wave, and because the interaction travels with the primary wave, this results in the well known sharper crests and flattened troughs. The negative interaction term has a frequency of the difference of the two components, which produces a very long wave also known as *slow drift* that tends to decrease the water level under wave groups. The interaction effects become stronger in shallow water [33]. In Figure 2.11, an irregular linear wave of 11.2 m significant wave height and a peak period of 12 s is shown together with the second-order interaction components it causes.

Other second-order methods and variations

Several attempts have been made to devise mode-coupled methods that are capable of modeling the nonlinear interaction between wave components. The most notable among these are the nonlinear Schrödinger method [34] and the Hybrid Wave Model (HWM) [35].

The nonlinear Schrödinger method is attractive as the predictions show a better match with measurements than linear theory with Wheeler stretching, while the required computer power is minimal. Although the model predictions are promising, the method has received little attention in literature.

In Figure 2.11, the nonlinear interaction effects that occur between almost identical frequency components in an irregular sea surface are shown. This type of interaction is handled properly by a second-order perturbation model, but when the frequencies are completely different, phase modulation occurs which remains unaccounted for in the second-order model. The effect of phase modulation is depicted in Figure 2.12. A phase modulation method was developed, amongst others, by Zhang and Melville [36], to model the interactions occuring in the case of a short wave traveling a long wave. The HWM [37] has been devised to combine the conventional second-order perturbation model with the phase modulation model to account for both interactions. Despite combining both models in a sophisticated way results in an accurate prediction of kinematics, according to comparisons with measurements (for example [38, 39], the method has not been widely accepted due to the semi-empirical nature of the model [40].

Many variations of the second-order method exist, each with its advantages and limitations. A more detailed treatment and overview of second-order and comparable irregular nonlinear wave models is presented by Forristal [41] and Johannessen [42].

Boussinesq irregular waves

With the methods discussed up to this point, the error made for a certain wave steepness depends on the order of the method. Using higher-order models, waves with a higher degree of nonlinearity can be approximated, but all methods run into problems when the wave steepness increases to the breaking criterion. A more computationally demanding method that can handle waves up to the point of breaking is the Boussinesq model, named after the Boussinesq wave equations. Besides the demands on computer power, the equations involved in this method are fairly complex, which has prevented the method from being adopted as an engineering method [44], although the accuracy of the predictions are very promising. Details about the Boussinesq method are omitted here and can be found in the publication by Madsen [45].

Computational Fluid Dynamics methods

In the case of an overturning wave, neither of the mentioned methods will produce acceptable predictions as rotational and viscous effects become increasingly important. This has lead to the development of methods that numerically approximate the solution of the governing equations by discretizing the flow field on a

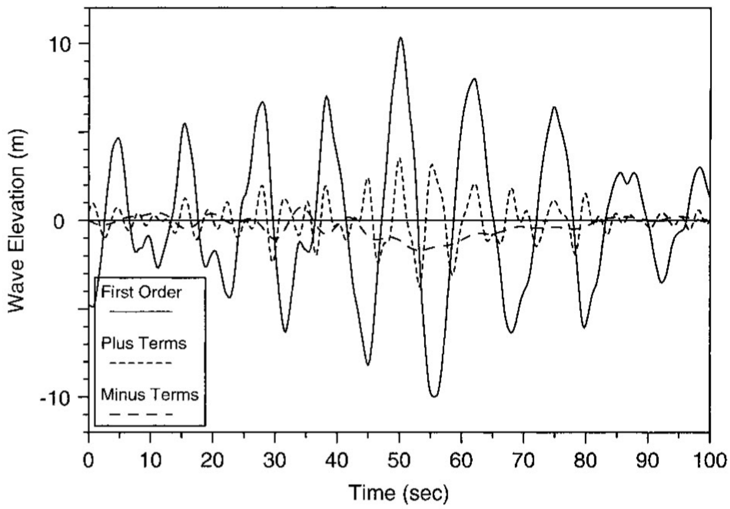

Figure 2.11: An example of the second-order interactions in an irregular wave. The solid line represents the first-order linear wave, the contribution of the positive interaction terms (--------) cause sharpened crests and flatter troughs while the negative interactions (– – – –) yield a setdown of the water level during the passage of the high wave group. [33]

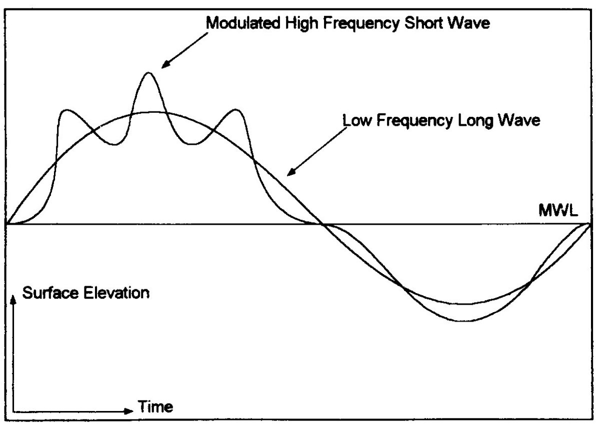

Figure 2.12: Phase modulation of a short wave riding on top of a long wave. The amplitude and the frequency of the high frequency wave increase on the wave crest, and decrease towards the trough. [43]

3-dimensional numerical grid. These *Computational Fluid Dynamics* (CFD) models applied to ocean surface waves are often referred to as *Numerical Wave Tanks* (NWT). Many different realizations have been published, where lots of variation can be found in the simplifications of the Navier-Stokes equations and the way the fluid, including the free surface are discretized. The main objective of this discussion is to list the types of equations such that a global understanding is achieved. A detailed round-up of state-of-the-art methods, including a discussion of advanced surface tracking methods as the Volume of Fluid method that can handle overturning and splashing waves can be found in publications by Fenton or Gopala [6, 46].

As CFD methods employ various types of governing equations depending on the required level of detail and characteristics of the flow, it might be confusing what level of physical detail the models actually have. To give an overview, the most elementary forms that can be derived from the Navier-Stokes (NS) equations are presented here. In its fully time-dependent form, the NS-equations can be discretized on a 3-dimensional grid to represent all unsteady turbulent features of the flow. This approach is called *Direct Numerical Simulation* (DNS), which requires that the governing equations are approximated up to the very smallest spatial and temporal scales of turbulence, known as Kolmogorov scales [47]. The essential nondimensional parameter in these scales, is the Reynolds number:

$$\mathcal{R}e = \frac{ux}{\nu} \tag{2.53}$$

where u and x are a characteristic velocity and length scale, respectively. The Reynolds number can be seen as the ratio between inertial and viscous forces in the flow and therefore gives a qualitative indication of the flow characteristics. The computational cost is proportional to the number of time steps times the number of grid cells. Using the Kolmogorov scales, the cost for a 3-dimensional DNS including all features of turbulence is proportional to the Reynolds number of the large vortices or *eddies*, $\mathcal{R}e_{\mathcal{L}} = \frac{\mathcal{U}\mathcal{L}}{\nu}$, as follows:

$$cost \propto (\mathcal{R}e_{\mathcal{L}})^3 \tag{2.54}$$

where $\mathcal{U}$ and $\mathcal{L}$ are typical velocity and length scales of the large eddies respectively. This implies that the number of equations to be solved and hence the computational burden of DNS is enormous, especially for practical problems on a full scale. This limits the application of DNS to fundamental research with low Reynolds numbers. A slightly less demanding simulation is obtained by using a model for the smallest eddies while the large eddies are fully simulated; this particulary method is referred to as *Large Eddy Simulation* (LES).

A method that abandons the direct simulation of turbulence is based on the *Reynolds-Averaged Navier-Stokes* (RANS) equations, in which a turbulent perturbation is added to the variables and the NS-equations are averaged. This yields an additional unknown, the turbulent shear stress or *Reynolds stress*, due to which the method needs an auxiliary equation to provide closure. Often, the Reynolds stress term is modeled using an expression derived from the conservation of energy law or by expressing the term as a function of an *eddy viscosity*. A de-

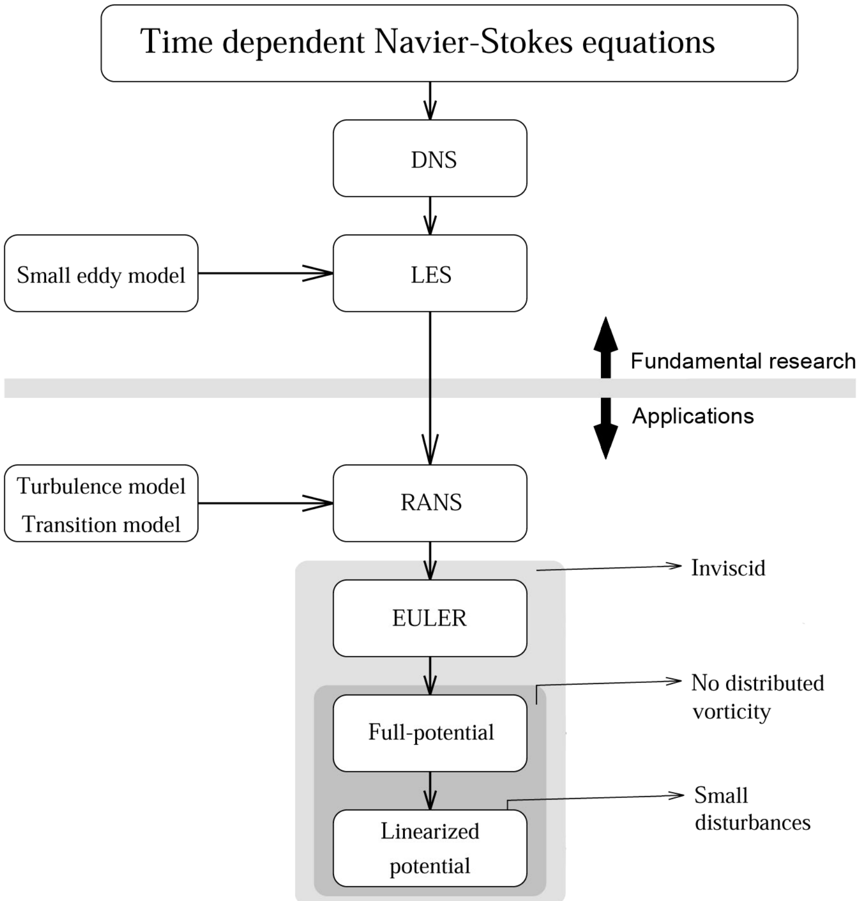

Figure 2.13: Overview of various degrees of simplification of the full time-dependent Navier-Stokes equations (after Gerrtisma, [48]).

tailed treatment of turbulent flows and appropriate Reynolds stress models can be found in the book of Pope [47].

Although the RANS-equations avoid the expensive direct simulation of turbulence, the models are complex and solving the system of equations remains quite computationally demanding. By neglecting the viscosity of the fluid, vorticity of the fluid is preserved whereas internal fluid friction is ignored, which simplifies the equations significantly. The inviscid form of the NS-equations is referred to as the *Euler* equations. A further simplification is obtained if the fluid is assumed to be irrotational, which gives the potential flow equations. As was shown in the derivation of equations of motion for linear theory, Section 2.2.4, potential flow allows the continuity equation to be written as the Laplace equation with a velocity potential. As the boundary equations contain nonlinear terms in case of a sea surface wave, linearization was employed to arrive at the linearized potential flow equations, which ultimately yielded the simple expressions for the wave kinematics. A graphical illustration of the various forms of the Navier-Stokes equations including the simplifications is presented in Figure 2.13.

The high demands on computer power and the complexity of discretizing the flow field and the governing equations has prevented CFD models from breaking through as engineering methods for predicting wave kinematics. However, quite recently a 3-dimensional potential flow method has been developed using a finite-difference scheme on a robust multigrid [49], which has shown good agreement with measurements. A very interesting development, besides the increasing sophistication of the methods itself, is the clever use of modern computer hardware by parallelizing the computations and running them on multi-core central processing units (CPU). A very recent study has shown that graphics processing units (GPU) take computations to a whole new level, employing the many-core architecture of the GPU to achieve a speedup of more than an order of magnitude compared to a single-core CPU [50], which can be considered striking at least.

2.2.7 Interaction of waves with a current

Most of the kinematic models described above are based on the assumption that a current is absent. In tidal waters however, a current can have a significant contribution to the velocity and hence the hydrodynamic force experienced by a structure. Consider a wave train traveling on a steady current that has a velocity U_C, where the current velocity is taken positive when the current flows with the waves. As the waves are convected with the current, an observer in a stationary reference frame notices a change in the wave frequency. This *apparent* frequency ω_{A} is related to the *relative* frequency of the waves ω_r observed in a *moving* reference frame as follows:

$$\omega_{\text{A}} = \omega_{\text{R}} + k\widetilde{U}_C \tag{2.55}$$

This frequency change is recognized as the Doppler shift. The term $\widetilde{U}_C$ is the weighted depth-averaged current [51], which for an arbitrary current U_C is expressed as:

$$\widetilde{U}_C = \frac{2k_m}{\sinh k_m d} \int_{-d}^{0} U_C(z) \cosh 2k_m(z+d) \ \mathrm{d}z \tag{2.56}$$

In the hypothetical situation that the current in the observation area is equal to the current in the area where the waves were created, the wave shape and kinematics, as observed from the relative coordinate system traveling with the current, remain unchanged from wave theory predictions. In many cases however, current conditions change as waves propragate into a different area, causing interaction between the current and wave properties. As this effect is difficult to model, wave kinematics are often superimposed to a current profile, assuming no interaction [52].

Different types of currents can be distinguished, which generally are added together by linear superposition. Tidal currents are often dominant as they may reach a maximum of 1 m/s at the surface, but higher magnitudes are not uncommon. The tidal current velocity profile $U_{C,tide}$ is a function of the depth and the surface current and generally follows a power law [53]:

$$U_{C,tide}(z) = \left(1 + \frac{z}{d}\right)^a \cdot U_{C,tide}(0) \tag{2.57}$$

where a is an empirical power law coefficient. The additional current due to wind friction at the sea surface $U_{C,wind}$ is usually assumed to decrease linearly with increasing depth:

$$U_{C,wind}(z) = \left(1 + \frac{z}{d}\right) \cdot U_{C,wind}(0) \tag{2.58}$$

Other contributions to the total current are due to large scale ocean circulations, local water density differences, *longshore* currents due to waves breaking at angle on the shore and extreme events like tsunamis [11].

2.2.8 Coastal effects

Especially in coastal areas, interaction of waves with physical objects have a pronounced effect on the characteristics of the waves. Three phenomena that are important in coastal waters or are considered here.

- **Shoaling**
  When a wave approaches the coast, the water depth decreases. The wave retains its frequency, but as the dispersion relation (2.36) remains valid, the wave length will decrease. Additionally, as energy has to be conserved in a vertical plane parallel to the wave crests, it can be derived [7, 9] that the ratio of the wave height near the coast, H_d, to the wave height at infinite water depth, H_∞, is equal to:

  $$\frac{H_d}{H_\infty} = K_{sh} = \sqrt{\frac{1}{\tanh kd \cdot \left(1 + \frac{2kd}{\sinh 2kd}\right)}} \tag{2.59}$$

  Here, K_{sh} represents the *shoaling coefficient*. With decreasing water depth, the wave height first *decreases* slightly, and finally when the depth approaches zero, in theory the wave height goes to infinity. Of course, long before this occurs, the wave will break. The above confirms that especially if the water depth is small with respect to the wave length, shoaling may affect the wave height and thus the assumptions made in linear theory may be violated.

- **Refraction**
  When a wave approaches a straight coastline at an incidence angle, it can be observed that the propagation direction changes slowly, such that the wave turns towards the coast. This phenomenon is called *refraction*, and can be explained by the dependance of wave celerity on the water depth. In Section 2.2.4 the expression for the wave celerity was derived using the dispersion relation, and is repeated here for completeness:

$$c = \sqrt{\frac{g}{k} \tanh kd} \tag{2.60}$$

  As the water depth varies in the direction parallel to the wave crests, this relation shows that the part of the wave that is in relatively shallower water is slowed down, which effectively turns the wave towards the coast.

- **Diffraction**
  The phenomenon of *diffraction* can be shown by considering a unidirectional wave train traveling through water with a uniform depth, approaching a straight breakwater or headland that extends into the sea (see Figure 2.14). Diffraction causes the waves to enter the *shadow zone* behind the headland in a circular pattern, and as the energy of the waves entering the shadow zone is spread over a large region, the amplitude of the waves decays quickly. The influence of diffraction on wave behaviour is not limited to large scale land extensions, also near an offshore structure with a significant characteristic length compared to the wave length, the kinematics are influenced by diffraction [13].

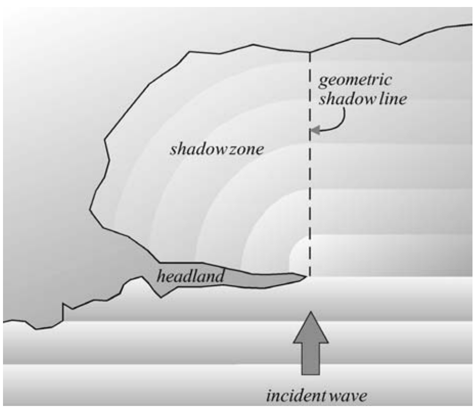

Figure 2.14: The phenomenon of diffraction around a headland. Waves propagate into the shadow zone in an almost circular pattern, with a strongly decaying amplitude. [7]

2.3 Wave kinetics

The previous section dealt purely with the problem of obtaining expressions for the velocity and acceleration of the water below a given sea surface profile, where the interaction of the fluid with physical objects was completely ignored. In the end, the objective of this research is to study the dynamic response of a wind turbine due to wave loading using more sophisticated wave models, therefore this section is devoted to obtaining the forces that are caused by the interaction of the fluid with the monopile support structure. In current offshore engineering, the two most widely used methods are the empirical *Morison equation* for slender structures where viscous effects play an important role, and *diffraction theory* based on potential flow for structures where diffraction effects dominate [54].

Except for diffraction dominated flows, the effect of fluid viscosity has a significant effect on the characteristics of the flow around a monopile, and hence on the exerted hydrodynamic force. The formation of an unsteady and turbulent *wake* with large eddies makes any method that ignores fluid viscosity and rotation inadequate. Hence, when considering flow problems that are not dominated by diffraction, including viscous effects is of fundamental importance, which indicates the desire to be able to perform a full approximation of the NS-equations by DNS (see Section 2.2.6). However, the astronomical computational demands of CFD solutions like DNS or even slightly simplified RANS methods make them infeasible for large scale practical use. Although increasing computer power will eventually make sophisticated solutions based on approximations of the NS-equations feasible in the future, the main focus of the discussion of wave kinetics will be put on the existing engineering methods and the concept of CFD is kept in mind.

The discussion of wave kinetics is started with a simple steady 2-dimensional flow around a cylinder, to illustrate important viscous flow effects like the boundary layer, flow separation and vortex shedding. Then, the problem is extended to an unsteady 2-dimensional flow, which introduces an additional inertia force due to fluid accelerations. Also, the Morison equation is introduced as an empirical method to estimate hydrodynamic forces due to drag and fluid inertia. Finally, the full 3-dimensional problem of a monopile subject to wave motion is considered, in which the effects of marine growth and diffraction are addressed and diffraction theory is presented. Finally, the range of applicability of the Morison equation and diffraction theory is discussed.

2.3.1 Steady viscous flow around a 2-dimensional cylinder

The steady flow around a 2-dimensional cylindrical object is a classic problem in the study of fluid dynamics, and although the object itself is straightforward, the complexity of the governing Navier-Stokes (NS) equations (Eqs. 2.18 and 2.19) has prevented the development of a simple but physically sound solution for the force acting on the cylinder. In linear wave kinematics, the NS-equations were

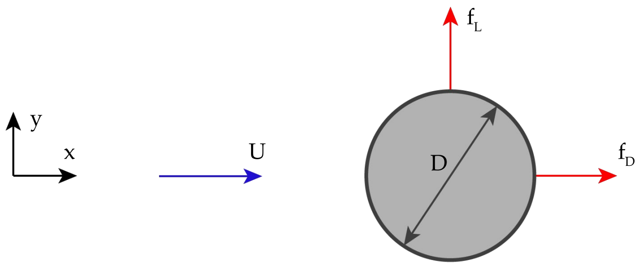

Figure 2.15: Lift and drag forces acting on a cylinder in a two-dimensional flow.

simplified to potential flow relations based on an (unphysical) idealized rotation-free and inviscid fluid, which resulted in a simple solution with acceptable accuracy in deep water. In a steady flow these fluid idealizations make absolutely no sense, since ignoring fluid viscosity will result in a friction free flow, which means that a *drag force* remains absent. This theoretical phenomenon is known as *D'Alembert's paradox*.

For the introduction to viscous fluid flow, consider a 2-dimensional circular cylinder of a diameter D submerged in a fluid with a *steady* velocity U and a kinematic viscosity ν, as illustrated in Figure 2.15. The resistive drag force per unit cylinder length f_D is defined in the direction of the flow, while the lift force per unit length f_L represents the force component acting perpendicular to the flow. The ratio between inertia and viscous forces is represented by the Reynolds number, which for a circular cylinder is given by:

$$\mathcal{R}e = \frac{UD}{\nu} \tag{2.61}$$

The drag and lift force per unit cylinder length can be expressed as a function of the empirical, dimensionless drag and lift coefficients C_d and C_l, times the dynamic pressure $q = \frac{1}{2}\rho u^2$ and the frontal area D:

$$f_D = \frac{1}{2}\rho C_d D u^2 \quad \text{and} \quad f_L = \frac{1}{2}\rho C_l D u^2 \tag{2.62}$$

As the dimensionless coefficients are only dependent on the Reynolds number and a vast amount of measurement data on cylinders is available in literature, the drag force in a steady flow can be predicted rather well. A typical $(C_d - \mathcal{R}e)$-curve for a 2-dimensional cylinder steady flow is shown in Figure 2.16, where a large variety in the value of C_d can be observed. To understand these large differences, understanding of the development of instabilities in the thin *boundary layer* on the upstream side of the cylinder and the related effects of *flow separation* are elementary. Below, these viscous effects are addressed.

Boundary layers and flow separation

When a fluid flows over a flat horizontal surface, it needs to satisfy the *no-slip condition*, which requires the horizontal fluid velocity to be zero on the surface. This condition yields a velocity gradient in a thin layer above the surface that is dominated by shear forces due to viscosity, the boundary layer. The skin friction experienced on the surface is proportional to the velocity gradient in the direction normal to the surface. In the outer flow above the boundary layer, the viscous effects are almost negligible. As the flow evolves in space, the boundary layer grows in thickness and small instabilities appear on the surface. In an early stage the boundary layer is *laminar*, which means that the instabilities are dampened out. Further down, the instabilities will be amplified up to the point where larger scale vortices appear throughout the boundary layer. This is the *transition point*, after which the boundary layer rapidly grows thicker and the flow inside the boundary layer is *turbulent*.

The development of the boundary layer over a flat plate in a flow with an external flow velocity u_e is shown in Figure 2.17. Here, the transition point is marked as x_{tr}. The position of the transition point is influenced by many variables, such as the Reynolds number, the pressure gradient, the level of turbulence in the incoming flow and the roughness of the surface, amongst others. The exact point of transition is hard to predict due to the many factors that play a role in the onset of turbulence, although some methods exist to make an approximation (see [55]).

When fluid flows over a convex surface rather than a flat plate, an adverse pressure gradient can cause the flow to *separate* from the surface. This causes a

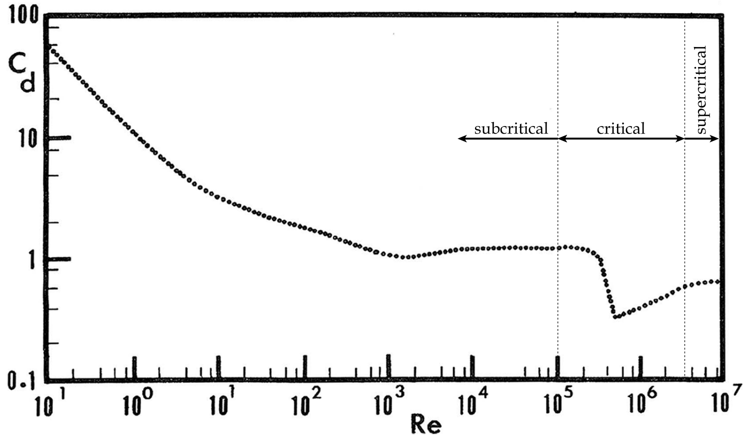

Figure 2.16: Drag coefficient of a cylinder in 2-dimensional steady flow as a function of the Reynolds number (after Sarpkaya, [13]). More details about the flow characteristics in the different Reynolds number regions can be found in Table 2.1.

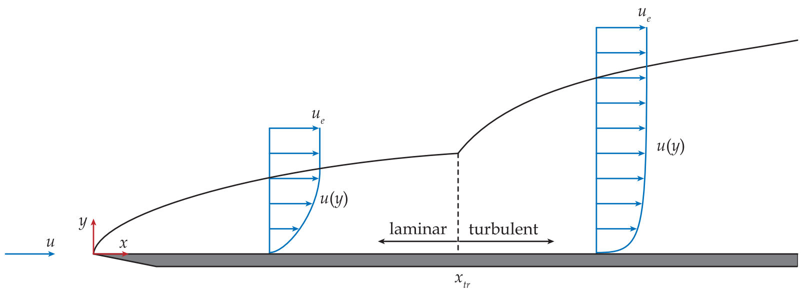

Figure 2.17: The development of a boundary layer over a flat plate.

backflow at the surface downstream of the separation point and the formation of a turbulent wake with large eddies behind the object. Although the skin friction drag may even be negative locally due to backflow at the surface, the pressure drag caused by the turbulent wake increases the total drag force on the object significantly. The location of the separation point largely depends on the Reynolds number, but also the state of the boundary layer has a massive impact on flow separation.

To illustrate this, consider the cylinder in a 2-dimensional flow again, for which the drag coefficient as a function of the Reynolds number is presented in Figure 2.16. In the *subcritical* low Reynolds number flows range ($\mathcal{R}e < 1{\cdot}10^5$), the boundary layer is laminar up to the point of flow separation. For a narrow *critical* range of somewhat higher Reynolds numbers ($1{\cdot}10^5 < \mathcal{R}e < 3.5{\cdot}10^6$), the flow still undergoes *laminar separation* but shortly downstream of the separation point, the boundary layer transitions to a turbulent state after which the flow will *reattach* to the surface. This *turbulent reattachment* is made possible by the better mixing characteristics of the turbulent boundary layer. The small region of separated flow between laminar separation and turbulent reattachment is known as the *laminar separation bubble*. Further downstream, the turbulent boundary layer will eventually fail to follow the curvature of the cylinder, after which the flow completely separates and a wake is formed. As turbulent reattachment reduces the width of the wake, the drag coefficient drops significantly. This critical region of reduced drag is also known as the *drag crisis*. In the *supercritical* range of higher Reynolds numbers ($\mathcal{R}e > 3.5 \cdot 10^6$), the transition to a turbulent boundary layer has moved upstream of the separation point, such that the flow undergoes turbulent separation and the drag coefficient rises slightly. An overview of the character of the flow for various Reynolds numbers is presented in Table 2.1.

Like the prediction of transition to turbulent flow inside a boundary layer, the dependance of the onset of flow separation on the Reynolds number, turbulence level of the flow, surface roughness and many more factors, the exact position of the separation point is hard to predict.

Vortex shedding

As can be observed in Table 2.1, for very low Reynolds numbers the wake behind a cylinder is stable. For most practical situations however, Reynolds numbers are much higher and the wake becomes unsteady. Even while the incoming flow may be perfectly steady and laminar, separation creates vortices on the upper and lower side of the cylinder, that move away from the cylinder in an alternating pattern. This phenomenon, called *vortex shedding*, causes an unsteady assymetric pressure distribution about the x-axis which in turn yields an oscillating lift force acting on the cylinder.

Apart from the critical Reynolds number regime ($10^5 < \mathcal{R}e < 3.5 \cdot 10^6$), the vortex shedding occurs at a preferred frequency which depends on the velocity of the ambient flow and the cylinder diameter. The vortex shedding frequency of a body at rest f_{st} can be represented as a nondimensional number by the *Strouhal number*:

$$\mathcal{S}t = \frac{f_{st} D}{U} \tag{2.63}$$

Like the drag coefficient, the Strouhal number depends on the Reynolds number, although the variation is less pronounced. A graph with the approximate preffered Strouhal number as a function of the Reynolds number is shown in Figure 2.18. Although the Strouhal number is fairly well known outside the critical Reynolds regime, the lift coefficient is very scattered, even for constant Reynolds numbers. The variation is especially present in the high subcritical regime where lift coefficients have shown to range from 0 to 1.4 in experiments, which is mainly

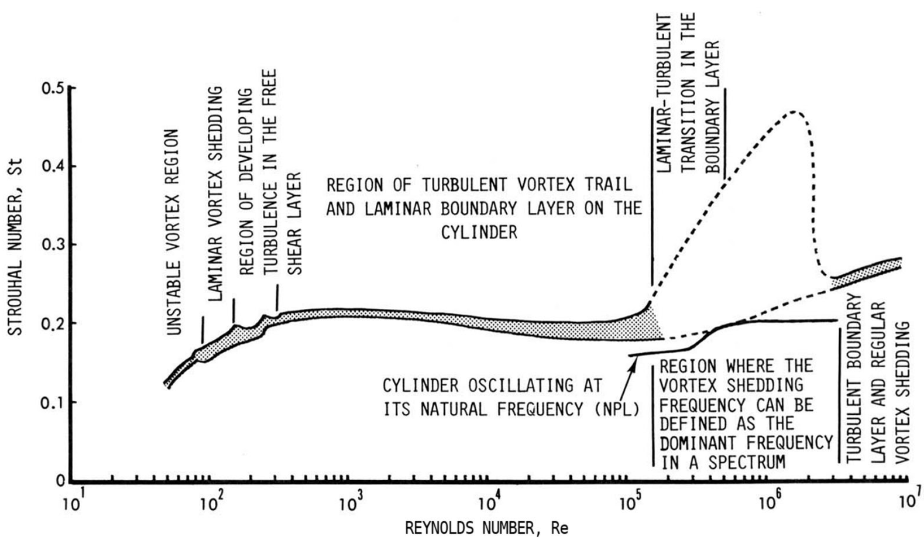

Figure 2.18: Strouhal number of a cylinder in 2-dimensional steady flow as a function of the Reynolds number. [13]

Table 2.1: The different flow characteristics of 2-dimensional cylinder flow for various Reynolds numbers (after Schlichting, [56]).

Reynolds number regime	Flow regime	Flow form	Flow characteristics
$\mathcal{R}e \to 0$	Creeping flow		Steady, no wake
3-4 $< \mathcal{R}e <$ 30-40	Vortex pairs in wake		Steady, symmetric separation
30-40 $< \mathcal{R}e <$ 80-90	Onset of Karman vortex street		Laminar, unstable wake
80-90 $< \mathcal{R}e <$ 150-300	Pure Karman vortex street		Karman vortex street
150-300 $< \mathcal{R}e < 1 \cdot 10^5$	Subcritical regime		Laminar, with vortex street instabilities
$1 \cdot 10^5 < \mathcal{R}e < 3.5 \cdot 10^6$	Critical regime		Laminar separation Turbulent reattachment Turbulent separation Turbulent wake
$\mathcal{R}e > 3.5 \cdot 10^6$	Supercritical regime		Turbulent separation

caused by the strong dependance of separation behavior on the amount of free-stream turbulence [13]. The large scatter makes a prediction of the oscillating lift force by the use of a lift coefficient very prone to errors.

2.3.2 Unsteady viscous flow around a 2-dimensional cylinder

Although the vortex shedding described above clearly is an unsteady phenomenon, it occurs even in a completely steady turbulence-free ambient flow. When we consider an unsteady flow, for example an oscillatory flow due to wave motion, wake formation due to separation and vortex shedding remain to occur, but as the Reynolds number varies throughout the flow cycle, the behavior of separation and vortex shedding becomes increasingly difficult to predict. Furthermore, as the turbulent wake formed in the first stage of the cycle may be swept past the cylinder again during the return stage, the *history* of the motion introduces yet another complication which makes the prediction of a simple drag coefficient something that is very likely to produce large errors.

Besides the effects of varying initial flow conditions and changing flow characteristics during the cycle, an object in an unsteady flow experiences an additional force in the flow direction that is not experienced in steady flow, due to the presence of accelerations in the fluid motion. Below, this acceleration force is addressed and an extension of the empirical drag relation (Eq. 2.62) that includes this force, known as the Morison equation, is presented.

Added inertia and the Morison equation

The additional drag force due to fluid acceleration can be understood best if an object in a stationary medium is considered. When the object is accelerated, one experiences that the required force is higher than what would be expected based on Newton's second law and the instantaneous drag force due to the object motion. In other words, the object appears to have an *added mass*, but of course as mass is conserved the actual mass of the object stays constant. What is experienced here is a force required to accelerate the fluid surrounding the object, or alternatively to achieve a change in fluid inertia or kinetic energy. As this change can be negative as well, the term *added inertia* is more appropriate than added mass.

The relative contribution of added inertia to the total force in flow direction depends on the magnitude and direction of the acceleration compared to the viscous drag force. In the case of an oscillating flow around a stationary 2-dimensional cylinder, the ratio between drag and inertial forces is expressed by the dimensionless Keulegan-Carpenter number:

$$\mathcal{KC} = \frac{U_0 T}{D} \tag{2.64}$$

where T is the period of the oscillating flow and U_0 the maximum fluid velocity during the cycle. For a *stationary body*, the inertial force per unit cylinder length f_I can be expressed as the function of a dimensionless inertia coefficient C_m, the fluid density ρ, the body volume per unit cylinder length (cross-sectional area) V_b' and the fluid acceleration $\dot{u} = \frac{\partial u}{\partial t}$:

$$f_I = \rho C_m V_b' \dot{u} = \rho C_m \frac{\pi D^2}{4} \dot{u} \tag{2.65}$$

For a body that *moves* with the oscillating flow, the expression becomes slightly more complicated. This can be explained by splitting the inertia force f_I into two terms:

- **Froude-Krylov force:** Regardless whether or not a body is present in the flow, a pressure gradient will exist in an oscillatory flow. A fluid acceleration changes the pressure distribution, which gives rise to the Froude-Krylov force ($\rho\frac{\pi D^2}{4}\dot{u}$).

- **Hydrodynamic added mass force:** The presence of a body modifies the flow, which causes a hydrodynamic force. When besides the fluid, the body itself undergoes an acceleration $\ddot{x}$, this force is proportional to the *relative* acceleration ($\rho C_a\frac{\pi D^2}{4}(\dot{u}-\ddot{x})$)

Body motion thus only influences the added mass force, which is written in terms of the added mass coefficient C_a. In case of a stationary body, the terms can be combined, hence it is recognized that the inertia coefficient C_m is related to C_a as:

$$C_m = 1 + C_a \tag{2.66}$$

Using this definition, the total inertia force can be rearranged to the following expression:

$$f_I = \rho\frac{\pi D^2}{4}\left[C_m\dot{u} + (1 - C_m)\ddot{x}\right] \tag{2.67}$$

Recognizing the contributions of viscous and inertial forces to the total in-line resistive force, Morison *et al.* [3] were able to devise a simple empirical relation using the formulations drag and added inertia forces with dimensionless coefficients (Eqs. 2.62 and 2.65), which has become widely known as the Morison equation. Using the

$$f_{Morison} = f_I + f_D = \rho C_m\frac{\pi D^2}{4}\dot{u} + \frac{1}{2}\rho C_d D\left|u\right|u \tag{2.68}$$

where the absolute sign in the drag term make sure that the direction of the force is preserved and C_m and C_d are the *cycle-averaged* force coefficients. Besides dependance on the Reynolds number, both force coefficients are also a function of the Keulegan-Carpenter number. The representation of inertial and drag forces by simple relations with empirical coefficients gives the suggestion that the two are not related and thus they can be added together in a linear fashion, which is the principle behind the Morison equation. However, it should be stressed that both forces modify each other, as the state of the wake and viscosity influence the inertial force and in turn fluid inertia affects the drag force [13]. Although this linear addition of the two force components is physically incorrect, a better formulation that satisfies hydrodynamic principles and is able to account for both viscous and inertial forces has not been devised yet.

Because of the strong dependance of the inertia and drag coefficient on $\mathcal{R}e$ and KC and on the roughness of the monopile, determination of cycle averaged values for the coefficients is a difficult task, although measurements and the introduction of the number $\beta = \frac{\mathcal{R}e}{\mathcal{KC}}$ by Sarpkaya yielded some useful graphs to estimate the values for flows up to the critical Reynolds regime (see [57] or [13]). In practical applications however, Reynolds numbers are often higher, which means that coefficients from laboratory measurements are inadequate. Therefore, force coefficients are often determined based on experience and design standards [58], which are discussed in Section 2.5.

2.3.3 Flow around a 3-dimensional monopile due to wave motion

So far, merely steady and unsteady 2-dimensional flow around a circular cylinder were considered in order to isolate fundamental phenomena that also occur in a real 3-dimensional flow caused by wave motion around the monopile foundation of an offshore wind turbine. As was observed in Section 2.2, the particle velocity and acceleration below a wave is a function of depth and time. The result is that the Reynolds number and hence separation behavior and vortex shedding frequency are also a function of depth and time. As vortices are continuous in the vertical direction, similar to a tornado that may occur in an unstable atmosphere, this obviously creates highly complex 3-dimensional vortical structures that may interact with each other and affect the flow in a way that simply can not be expressed by an empirical relation like the Morison equation. Furthermore, as fluid motion below a wave is morealess circular or ellipsoidal, the particle velocity is far from purely horizontal which further complicates the problem.

The Morison equation fails to give a physically correct description of the flow, but considering the fact that a more physical approach which is less complex and computationally demanding than a typical CFD approximation does not exist, using the Morison equation is the only feasible option in many situations. Using the expressions from previous sections, the Morison equation can be modified to include currents and structure movement. As discussed in Section 2.2.7, a current is assumed to only cause a Doppler shift in the apparent wave period while the kinematics of the waves remain unaffected. The current can therefore simply be added to the wave velocity, whereas the local monopile velocity $\dot{x}$ has to be subtracted such that the effective *relative* water velocity is used to calculate the drag force. The acceleration of the monopile $\ddot{x}$ can be taken into account using the expression of the inertial force as presented in Section 2.3.2. Including the current and the motion of the monopile yields the modified Morison equation for the in-line force per unit length:

$$f_{Morison} = \rho \frac{\pi D^2}{4} \left[C_M \dot{u} + (1 - C_M)\ddot{x} \right] + \frac{1}{2} \rho C_D D \left| u + U_C - \dot{x} \right| (u + U_C - \dot{x}) \tag{2.69}$$

Although the current has been added to the total apparent velocity in a linear fashion, the relative strength of the current with respect to the wave induced velocity may have significant influence on the character of the flow. Suppose the current velocity is comparable to the wave particle velocities, the flow will have an intermittent rather than an oscillatory character. As the flow is moving in the same direction for a longer sustained time and maximum velocities are higher, vortex shedding and wake development are promoted. This leads to a higher importance of viscous drag effects and different values for the force coefficients, which should thus be chosen with the effect of the current in mind.

Vortex shedding

The Morison equation provides an approximation for the in-line hydrodynamic load, but as was shown above, vortex shedding introduces transverse forces as well. Especially in situations in which a steady current dominates the flow or when the wave period is large (high Keulegan-Carpenter number), vortex shedding can yield significant lift forces which cause *vortex induced vibrations* (VIVs) in the support structure. When the vortex shedding frequency corresponds to a natural mode of the support structure, *lock-on* occurs, which means that resonance of the structure amplifies the VIVs. As the vortex shedding frequency varies with depth and time, only a section of the monopile will undergo lock-on for a certain amount of time, given that vortex shedding develops sufficiently and reaches the lock-on frequency.

In Figure 2.19, the wave-induced velocity, development of the transverse lift force and the vortex shedding response due to this force are shown as a function of time, during the passage of a regular wave. It can be seen that the response due to the vortex shedding induced lift force is mostly damped, only when lock-on occurs the response is amplified. To estimate the lift force, an approximate relation similar to the empirical lift equation 2.62 may be used, although the dependance on the vortex shedding frequency makes the approximation fairly difficult. The modeling of vortex shedding induced forces is considered to be outside the scope of this thesis, the reader is referred to literature [59, 13] for a more detailed discussion and a suitable modeling approach.

Influence of marine growth on the hydrodynamic force

On the surface of an offshore support structure various forms of marine excrescences can grow during its lifetime, which significantly roughen the surface of the structure. The geographic location of the site is important, as different ocean climates have different types of marine growth, ranging from hard mussels to soft seaweeds that may sweep back and forth with the waves.

Marine growth has a few influences on the loading on an offshore structure. First, the effective diameter of the structure increases, which causes a higher drag and inertial force due to the larger frontal area and displaced fluid volume. Second, the increased roughness causes a higher drag coefficient in the supercritical Reynolds regime, due to early transition to a turbulent boundary layer and higher profile drag of the surface itself. Third, separation behavior is strongly influenced by local roughness effects and the early transition to turbulent flow, hence the vortex strength, time-dependent lift force and the structure of the wake are different [60]. Fourth, the mass added by the marine growth and the increased effective diameter cause a reduction of the natural frequency

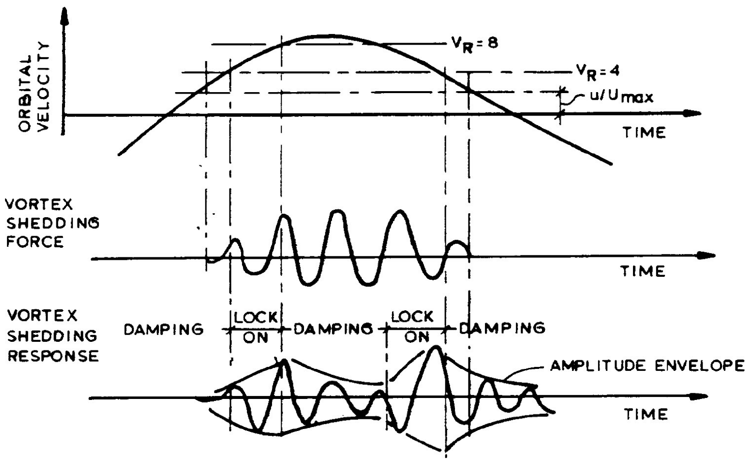

Figure 2.19: The development of the lift force and structural response due to vortex shedding during the passage of a regular wave. Top: wave-induced velocity. Middle: lift force due to vortex shedding. Bottom: response, showing amplification (lock-on) when the forcing frequency corresponds to a natural mode of the structure. [11]

of the support structure [61, 13]. Finally, considering the difference between soft and hard growth, a cylinder covered in long seaweed has shown to experience significantly higher forces, because the motion of the weed with the flow has an additional inertial effect on the loading [13].

Simply accounting for marine growth by using force coefficient values from measurements on cylinders in a steady flow would be inappropriate, as an oscillatory flow has shown to have a different effect of roughness on hydrodynamic loading [62]. The influence of roughness on the coefficients C_D and C_M is often presented in graphs where for different values of the *relative roughness* the coefficient is plotted against the Reynolds number. The relative roughness e is defined as the typical roughness height of the marine excrescence k divided by the cylinder diameter D:

$$e = \frac{k}{D} \tag{2.70}$$

Typical graphs for both coefficients can be found in [13]. An overview of the different types of marine growth and a typical growth profile as a function of depth for a foundation in the North Sea is presented in [63]. Good knowledge of the type and amount of marine growth and the appropriate force coefficients is important as the highest amount of growth is found near the sea surface, where the wave kinematics reach their peak values and hence the influence on the loading is the most significant.

Diffraction effects and diffraction theory

Especially for structures that are relatively large with respect to the wave length, diffraction effects significantly alter the form of the wave field in its vincinity. As a rule of thumb, diffraction effects should be taken into account when the *diffraction parameter* $(\pi D/L)$ is larger than 0.5 [58]. A slightly different definition of the diffraction parameter in which π is omitted, is sometimes found in literature as well [53]. It can also be concluded that for diffraction dominated flows, the Keulegan-Carpenter number is small, and hence viscous effects are less significant, which raises the question whether a different kinetic model than the Morison equation would be more appropriate. Diffraction theory is a method which exploits the insignificance of turbulence in diffraction dominated flows and focusses on the inertial forces due to accelerations in the flow.

If the viscous effects and fluid vorticity are assumed to be completely negligible, the interaction of waves with the structure can be modeled with a simplified potential flow, where a velocity potential satisfies the Laplace equation $\nabla^2\Phi = 0$. The surface of the structure is replaced by a finite number of panels that each carry a source, hence the method is often referred to as the panel method, or in offshore engineering as the Boundary Element Method (BEM). The sources on the individual panels are of such strength that the impermeability condition of the body is satisfied:

$$\frac{\partial \Phi}{\partial n} = 0 \qquad \text{at body surface} \tag{2.71}$$

where $\frac{\partial}{\partial n}$ represents the gradient normal to the surface panel. The simplest solution is obtained when linear diffraction is assumed, in which the boundary conditions from linear wave theory (Section 2.2.4) and the additional impermeability condition at the body surface define the problem. The procedure then is to write the velocity potential Φ as the linear sum of an "incident-wave" potential Φ_w and a "scattered-wave" potential Φ_s, which both satisfy the boundary conditions.

Force components can be found from the pressure distribution, which is derived from the linearized Bernouilli equation and is a function of the time-derivative of the velocity potential and the hydrostatic fluid pressure. It must be emphasized once more that because the force only includes inertial contributions, as viscous drag forces due to friction and wake formation are ignored, the method is only applicable in the diffraction dominated regime. Solutions for diffraction theory applied to a circular cylinder and higher-order diffraction methods are presented in Sarpkaya [13].

In order to account for linear diffraction effects in the Morison equation, the empirical MacCamy-Fuchs correction [64] can be applied to the inertia force. This correction comprises a modification of the inertia coefficient C_M and a phase-lag on the inertia force. This modified force coefficient $\hat{C}_m$ and phase-lag

ϕ_{MCF} are a function of the diffraction parameter $(kD/2)$ and are given as:

$$\hat{C}_M = \frac{4}{\pi(kD/2)^2\sqrt{[J_1'(kD/2)]^2 + [Y_1'(kD/2)]^2}} \tag{2.72}$$

$$\phi_{\text{MCF}} = \arctan\frac{J_1'(kD/2)}{Y_1'(kD/2)} \tag{2.73}$$

where J_1' and Y_1' are the derivatives of the first order Bessel function of the first and second kind, respectively. In Figure 2.20, $\hat{C}_m$ and ϕ_{MCF} are shown as a function of the diffraction parameter $(kD/2)$. The modified inertia coefficient $\hat{C}_M$ is calculated for the theoretical value of C_M in potential flow, $C_M = 2$ [13]. It can be observed that the modification to the inertia coefficient effectively works as a low-pass filter on the inertia force.

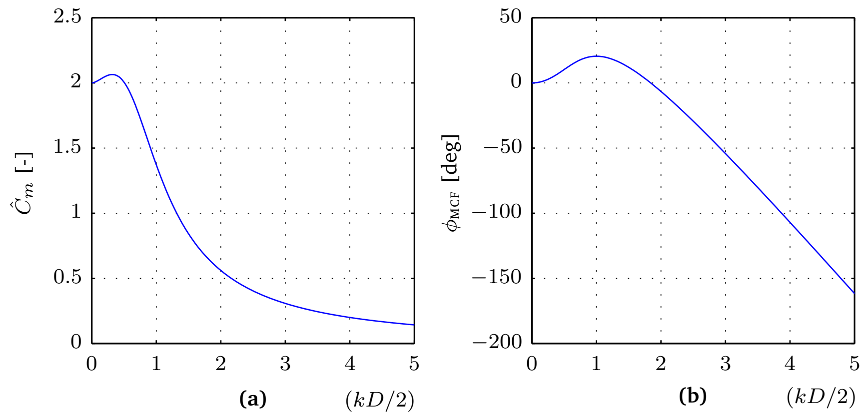

Figure 2.20: The MacCamy-Fuchs diffraction correction for the inertia coefficient C_M (a) and phase lag ϕ_{MCF} (b) as a function of the diffraction parameter $(kD/2)$.

Range of validity of the Morison and diffraction methods

The above mentioned value of the diffraction parameter that separates the regime of validity of the Morison equation and diffraction theory ($\pi D/L = 0.5$) is not hard. In fact, a somewhat different definition is used in literature as well, suggesting a demarcation line at $(D/L) = 0.2$ [53]. For the individual methods, several regimes can be identified to indicate the dominant features in the flow, as is shown in Figure 2.21. The lower right part of the graph indicates that diffraction theory should be used, while left of the demarcation line at $(\pi D/L) = 0.5$ the Morison equation is more appropriate. For low wave heights with respect to the structure diameter, drag forces are small or even negligible, while for high wave heights inertia becomes less significant. Identifying the regime in which the Morison equation is used is helpful to determine which coefficient is dominant and should thus be chosen with care.

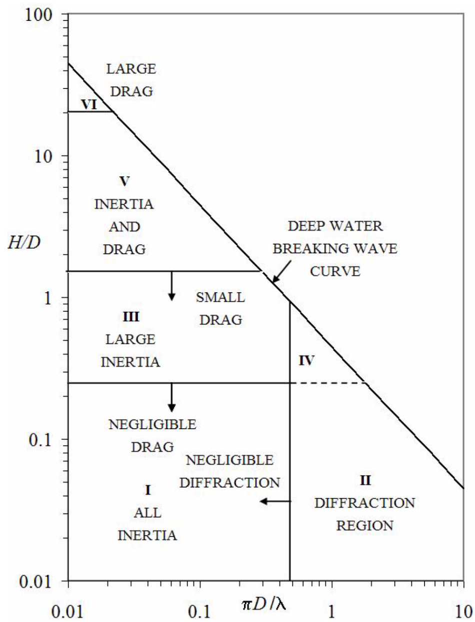

Figure 2.21: Regimes of dominant forces in hydrodynamic wave loading. Here, the wave length is represented by λ. [11]

2.4 Offshore wind turbine response dynamics

The final objective of this thesis is to quantify the influence of using more sophisticated wave models and the relative motion of the support structure on the dynamic response of the offshore wind turbine system. In order to be able to critically assess this influence, fundamental knowledge of structural modeling and response dynamics is required. This section therefore serves as a very global introduction to these topics. First, a simple structural model is introduced and basic response characteristics are discussed and typical excitation frequencies and natural frequencies of the wind turbine system are presented. Second, the frequencies are compared to illustrate the options for the support structure stiffness in the design space and damping forces that attenuate the response are discussed.

2.4.1 Support structure dynamics

A simple way to model the support structure of an offshore wind turbine is to consider it as a clamped pile on which the rotor and nacelle are represented by a point mass M, as depicted in Figure 2.22a. The pile has a certain Young's modulus E, moment of inertia I and a mass per unit length μ. The structure supporting the mass can alternatively be modeled as a large number of coupled mass elements that are connected to a fixed wall by a spring and a viscous damper. To introduce response dynamics, a single spring-mass-damper system is considered, where the motion of the mass is restricted to translation in line with the spring and the damper. This simple system is therefore referred to as a single *degree-of-freedom* (DOF) system. An example of such a spring-mass-damper system, loaded by a time-dependent force $f(t)$, is shown in Figure 2.22b. The response of this

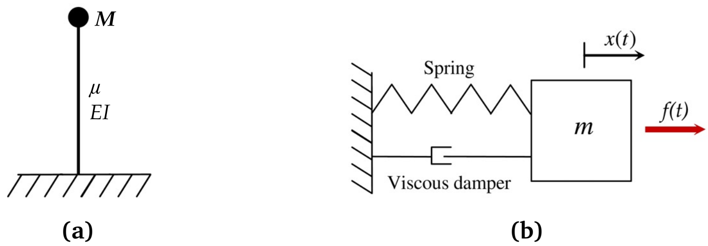

Figure 2.22: Simple structural model of an offshore wind turbine (a) and an element of the support structure modeled as a mass connected to a wall by a spring and a damper (b). [66]

simple single DOF system is governed by the following equation of motion:

$$M\ddot{x} + C\dot{x} + Kx = f \tag{2.74}$$

Here, x represents the relative position of the mass with respect to its position in rest, C is the damping coefficient and K denotes the spring stiffness. To illustrate the different types of forced response behavior that this mass-spring-damper system can show, a simple harmonic force $f(t)$ is applied to the mass, which results in a harmonic excitation $x(t)$. As shown in Figure 2.23, responses characteristics can be divided into three categories:

a) **Quasi-static**
For a harmonic force lower than the natural frequency of the system, the mass responds with an excitation that is similar to the response due to a static load. The mass follows the time-dependent force almost instantly, without significant phase lag.

b) **Resonance**
When the force is applied with a frequency close to the system's natural frequency, the inertia and spring force almost cancel. The excitation is therefore significantly larger than in the quasi-static case, and the amplification of the response is only limited by the amount of damping present in the system. The phase lag of the resonating system compared to the force is around 90 degrees in this narrow regime.

c) **Inertia dominated**
For a force with a higher frequency than the natural frequency of the sys-

tem, the system inertia prevents large excitations as the mass cannot follow the force anymore. The amplitude of the excitation is therefore very limited and almost in counter-phase with the force.

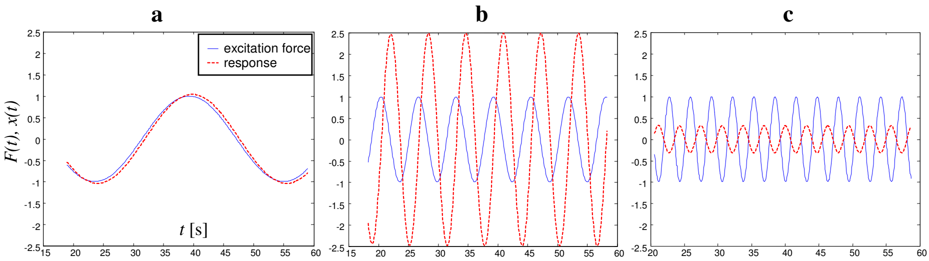

Figure 2.23: Response types of the forced mass-spring-damper system from Figure 2.22b. The blue lines represent the applied harmonic force, while the red lines show the excitation of the mass. Response types that can be distinguished are: **a)** Quasi-static **b)** Resonance **c)** Inertia dominated. [67]

The amplification and phase lag of the response of the single DOF system can alternatively be shown in the frequency domain. In Figure 2.24 the dynamic amplification factor (DAF) and the phase lag are plotted against the excitation frequency, which is normalized with the system's natural frequency. The DAF indicates the amplification of the dynamic response with respect to the response to a static load of the same magnitude. Clearly visible in these graphs are the sharp amplification peak and the sudden change in phase lag when the frequency of the force is close to the natural frequency of the system. Although adequate damping can prevent excessive amplification of the excitation, time-varying loads need to be assessed carefully, especially if the frequency is close to the natural frequency of the system. This can result in an extreme load cases or even failure, but perhaps even more important is the impact on fatigue life of the structure when high cycle fatigue loads operate in the critical frequency range.

Rotor and blade dynamics

Besides the dynamics of the tower, the response of an offshore wind turbine is also influenced by the rotor. The first excitation frequency of the rotor is the rotation frequency, often referred to as 1P. This excitation can be experienced if there is a mass unbalance in the rotor, which introduces an oscillating loading in the rotation plane. A second important excitation frequency is the blade-passage frequency or N_bP, where N_b is the number of rotor blades. This excitation mode represents the response when a blade passes a disturbance in the flow, for example the tower or a local turbulence or wind shear field, which temporarily changes the load on the blade. Higher frequency modes are due to flapping and lead-lag bending of the rotor blades, the latter referring to the elastic back and

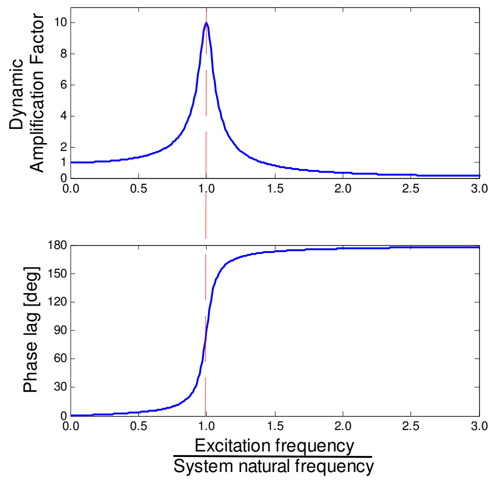

Figure 2.24: The dynamic amplification factor (top figure) and the phase lag (bottom figure) of the excitation versus the normalized frequency. [67]

forth motion of the blade in the rotation direction.

In case the rotational speed of the rotor is constant and does not depend on the wind speed, the 1P and N_bP frequencies are constant, but when the rotor speed is variable the frequencies are proportional to the wind velocity, which makes the design envelope slightly more complex. In order to compare the excitations with the natural frequencies of wind turbine components, the Campbell diagram (Figure 2.25) is used to depict the frequencies as a function of the wind velocity. As a wind turbine is only producing energy and hence the rotor is only operational in the wind regime between the *cut-in* and *cut-out* wind velocity, v_{ci} and v_{co} respectively, the 1P and N_bP frequencies are only relevant inside this regime.

2.4.2 Support structure stiffness and damping

To avoid resonance of the support structure with the 1P and N_bP frequencies, the support structure should be designed such that its stiffness does not result in a natural frequency that is close to the 1P and N_bP frequencies. The stiffness depends on the elastic modulus of the material E, the moment of inertia of the cross section I and the length of the structure L.

Three approaches for the tower stiffness are available to avoid coinciding frequencies. First, a very stiff structure can be used, with a natural frequency well above the 1P and N_bP frequencies. To achieve this *stiff-stiff* design, a high support structure diameter is required, which makes the procurement of the structure more difficult and causes higher wave loads. A *soft-stiff* design with a natural

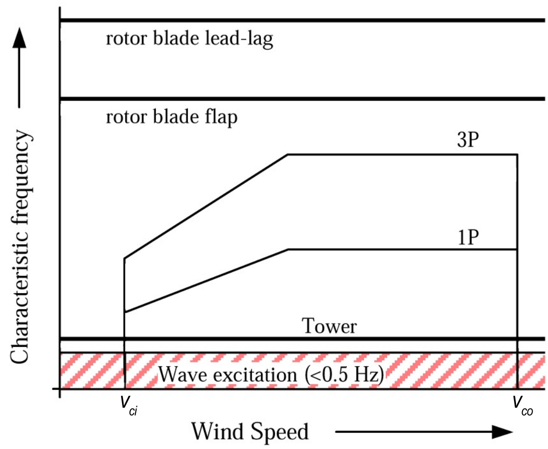

Figure 2.25: The Campbell diagram, showing the natural and excitation frequencies of an offshore wind turbine as a function of the wind velocity. After Nijssen, [68]

frequency that lies between the 1P and N_bP frequencies will result in a more slender structure, but especially when the rotor speed is variable, the frequency interval may be small or even absent. In theory this would render a design in this region infeasible, however, by tuning the rotor controller such that the natural frequencies are skipped, a soft-stiff design can be realized after all. Finally, a *soft-soft* structure has a natural frequency lower than the 1P and N_bP frequencies and therefore is more sensitive to resonance due to wave loads, as these typically have a low frequency.

Attenuation of the response

Except for excitations in the resonance regime, several factors will damp the response of the support structure. Even if no external damping forces act on the structure, an unforced oscillation will decay due to energy losses in the elastic deformation of the structure. External forces that attenuate the structural response include hydrodynamic damping of the submerged section of the support structure, damping of the foundation due to interaction of the structure with the soil and aerodynamic damping from the rotor.

When excitations of the support structure are in line with the wind direction, the motion is slightly damped by a temporal change in the aerodynamic force. Assuming the rotor blades instantly follow the motion of the support structure, the motion of the blade introduces a change in the angle of attack of the incoming flow, which results in a different aerodynamic force. As the angle of attack *increases* when the blade translates towards the wind, the aerodynamic force *increases*, which effectively opposes the direction of motion of the structure. Vice versa, a motion in the direction of the wind results in a *decrease* of the aerodynamic force. Hence, the change in aerodynamic force due to structural motion acts as a convenient damping force if the motion is aligned with the wind. When the motion is strongly misaligned with the wind direction, aerodynamic damping is absent and the structural response can be significantly more severe. Misalignment occurs when wave loads are dominated by a swell that propagates perpendicularly to the wind direction.

Except for the wind-wave misalignment case, aerodynamic damping dominates the attenuation of the wind turbine response. The influence of structural, hydrodynamic and soil damping are assumed to be comparable and small [69], although recent research suggests that the soil has a larger effect on damping than is assumed in the industry today [70].

2.5 Standards for offshore wind turbine design

As was shown in the previous sections, there are several approaches available to model the wave kinematics and kinetics. Besides that, a significant amount of empirical relations are used in practice, where the determination of characteristic coefficiens and variables often involves a combination of results from measurements and engineering experience. Prior to performing a trade-off to decide which models are appropriate, it is therefore convenient to inspect the engineering standards that have been developed over the years. For this study, two wind turbine design standards were considered: the International Standards (IEC 61400-3) by Danish Standards [71] and the Offshore Standards (DNV-OS-J101) by Det Norske Veritas [72]. Throughout this thesis, these will be referred to as IEC standards and DNV standards respectively. Furthermore, reference is made to DNV Recommended Practice (DNV-RP-C205), [11].

2.5.1 Wave energy spectrum formulations

In Section 2.2.3, the Pierson-Moskowitz (PM) and JONSWAP wave spectra were introduced, which can be used with a directional distribution to create a 3-D sea surface. In general, as wave propagation direction is hard to measure, unidirectional sea states should be used, especially in shallow water. The PM-spectrum is to be used in case the sea is fully developed, while in coastal waters and fetch-limited situations the JONSWAP spectrum is more appropriate. For a wind sea where swell components are significant, DNV suggests considering the two-peaked Torsethaugen spectrum (see DNV Recommended Practice [11]). The following formulations of the PM and JONSWAP spectra are prescribed by IEC standards:

$$S_{PM}(f) = 0.3125 \cdot H_S^2 \cdot f_p^4 \cdot f^{-5} \cdot \exp\left[-\frac{5}{4}\left(\frac{f_p}{f}\right)^4\right] \tag{2.75}$$

$$S_{JS}(f) = C(\gamma) \cdot S_{PM}(f) \cdot \gamma^{\exp\left[-\frac{(f-f_p)^2}{2\sigma^2 f_p^2}\right]} \tag{2.76}$$

The peak-width parameter σ depends on whether the frequency is smaller or larger than the peak frequency f_p. The following empirical values are to be used:

$$\sigma = \begin{cases} 0.07 & \text{for} \quad f \leq f_p \\ 0.09 & \text{for} \quad f > f_p \end{cases} \tag{2.77}$$

The peak-enhancement factor γ in the JONSWAP-spectrum depends on the peak period T_P and the significant wave height H_S:

$$\gamma = \begin{cases} 5 & \text{for} \quad \frac{T_P}{\sqrt{H_S}} \leq 3.6 \\ \exp\left(5.75 - 1.15\frac{T_P}{\sqrt{H_S}}\right) & \text{for} \quad 3.6 \leq \frac{T_P}{\sqrt{H_S}} \leq 5 \\ 1 & \text{for} \quad \frac{T_P}{\sqrt{H_S}} > 5 \end{cases} \tag{2.78}$$

The normalizing factor $C(\gamma)$ is defined as follows:

$$C(\gamma) = 1 - 0.287 \ln \gamma \tag{2.79}$$

In case $\gamma = 1$, the normalizing factor is unity and the PM spectrum is recovered. Rearranging and collecting terms, the JONSWAP spectrum expression can be written as:

$$\begin{aligned} S_{JS}(f) = &0.3125 \cdot H_S^2 \cdot T_P \cdot \left(\frac{f}{f_p}\right)^{-5} \cdot \exp\left[-\frac{5}{4}\left(\frac{f}{f_p}\right)^{-4}\right] \dots \\ &\cdot (1 - 0.287 \ln \gamma) \cdot \gamma^{\exp\left[-\frac{(f-f_p)^2}{2\sigma^2 f_p^2}\right]} \end{aligned} \tag{2.80}$$

The peak period T_P is related to the mean zero-crossing period T_Z using the following approximate relationship:

$$T_P = T_Z \sqrt{\frac{11 + \gamma}{5 + \gamma}} \tag{2.81}$$

2.5.2 Wave kinematics model

Various options are available to obtain wave kinematics from a certain sea surface elevation profile, as was shown in Section 2.2. The required wave model mainly depends on the type of load case that is to be investigated and the degree of nonlinearity of the waves. For ultimate load cases due to the passage of an extreme, deterministic wave, a nonlinear regular wave model such as the Fourier approximation method is often used. For fatigue load analysis, a stochastic series of irregular waves is used corresponding to the wave spectrum that follows from the significant wave heights and wave periods from metocean data. To simulate the full effects of an extreme wave however, the deterministic nonlinear regular wave is usually smoothly *pasted* into a linear irregular wave record of a normal sea state, such that the turbine dynamics are already present in the simulation at the time that the extreme wave passes by.

For regular waves, both IEC and DNV standards advise to use the regimes of applicability as presented in the discussion of nonlinear regular wave theories (Figure 2.9) as a guideline to select the appropriate wave model. In contrast with regular waves, none of the standards advises the use of a nonlinear wave theory to model *irregular* waves. In IEC standards the Boussinesq model is considered, but due to the slow convergence and long simulation time, only the linear irregular wave model with Wheeler stretching is advised as a viable option. In DNV Recommended Practice however, the second-order irregular wave model discussed in Section 2.2.6 is recommended as an appropriate model to account for nonlinear effects in irregular waves.

2.5.3 Currents and still water level

Unless detailed field data is available, the current can be modeled as described in Section 2.2.7, by superposition of a current due to tide and a wind-induced current. The velocity profile of the tidal current as a function of depth is described by a power law, with a power law coefficient of $1/7$. The variation of the wind-induced current with depth is approximated by a linear relationship. This results in the following current model:

$$U_C(z) = U_{C,tide}(z) + U_{C,wind}(z) \tag{2.82}$$

$$= \left(1 + \frac{z}{d}\right)^{1/7} \cdot U_{C,tide}(0) + \left(1 + \frac{z}{d}\right) \cdot U_{C,wind}(0) \tag{2.83}$$

The tidal current at $z = 0$ is usually known, and unless indicated otherwise, the wind-induced current at the surface may be estimated from the wind velocity at 10 m altitude U_{10} using the following expression:

$$U_{C,wind}(0) = kU_{10} \tag{2.84}$$

where k is an empirical constant in the range $0.015 \leq k \leq 0.03$.

As discussed at the beginning of this chapter, the water level is influenced by astronomical tides and storm surges. Tides fluctuate between the lowest and highest astronomical tide (LAT and HAT respectively) and storm surges can either have a negative or a positive contribution. The extremes of the still water level that may occur when tides and storm surges combine are shown Figure 2.26. According to standards, these levels shall be determined from site-specific metocean data, where correlation techniques may be necessary to derive the contribution of storm surges.

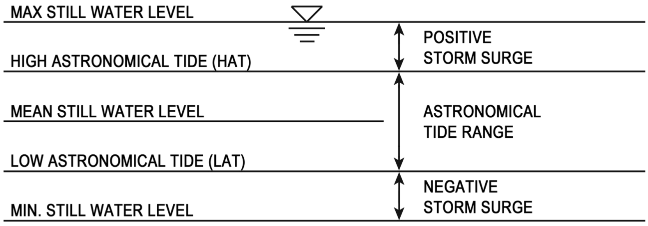

Figure 2.26: Definition of water levels. After DNV, [72]

2.5.4 Wave kinetics model

Unless hydrodynamic loading is dominated by wave diffraction ($D/L > 0.2$), the Morison equation is considered to be the only feasible option to approximate wave kinetics. The main problem with the Morison equation is the selection of the values of the drag and inertia coefficients, C_D and C_M, which strongly depend on the Reynolds number, Keulegan-Carpenter number, surface roughness and the relative influence of the current. The force coefficients are often assumed constant, where the appropriate values are selected for two types of surface roughness, smooth and rough. Sections affected by marine growth are classified as rough, whereas the remaining sections are assumed to be smooth.

For the inertia coefficient, the MacCamy-Fuchs correction for diffraction effects as described in Section 2.3.3 is applied. Typical values for the inertia coefficient are $C_M = 2.0$ for smooth sections and $C_M = 1.7$ for rough sections. For the drag coefficient, individual values of the support structure components and appurtenances are specified, as tabulated in Table 2.2. As the position of the appurtenances with respect to the support structure influences the drag contribution of that component, an *equivalent drag coefficient* that replaces C_D in the Morison equation (Eq. 2.69) can be used to account for the additional component drag:

$$C_{D,eq} = C_{D,0} + \sum_{l=1}^{N} C_{D,l} \frac{D_l}{D_0} \left[\left(1 + \frac{R_0^2}{R_l^2} \right) \sin \beta_l \right]^2 \tag{2.85}$$

Here, subscript ($_0$) refers to the primary structure and subscript ($_l$) to the appurtenance. R_0 and R_l denote the radius of the primary structure and the distance between the center lines of the appurtenance and primary structure, respectively. The angle between the fictitious line R_l and the incoming flow is represented by β_l. It can be observed that an appurtenance that is in-line with the flow and the primary structure is assumed not to contribute to the drag.

The straightforward coefficient selection procedure described above is frequently used by foundation designers and complies with IEC standards, however, more detailed empirical relations are available to take into account the influence of the Keulegan-Carpenter number, Reynolds number, VIVs and variation in

Table 2.2: Base values for the drag coefficient C_D of support structure components

		Monopile	Transition Piece	Fender	Ladder
C_D	rough	1.1	1.1	1.1	1.2
	smooth	0.7	0.7	0.7	1.2

the degree of surface roughness. These expressions are described in DNV Recommended Practice [11], but due to the approximate nature and complexity of these relations, implemenation is considered outside the scope of this thesis.

2.6 Trade-off for model selection

In the previous sections, various methods to obtain wave kinematics and hydrodynamic forces from the wave motion were presented. With the project objective in mind, in this section a trade-off between the available kinematic and kinetic approaches will be made to select the appropriate methods for this thesis project. The selection procedure for a kinetic method does not require a formal trade-off. It was already shown in the previous sections that the Morison equation is the only viable and recommended option for monopiles, as the influence of diffraction effects is often small and can be accounted for by the MacCamy-Fuchs correction, and CFD methods based on the approximation of the Navier-Stokes equations are too computationally demanding due to the dominance of turbulent features in the flow.

2.6.1 Kinematic wave model trade-off

What remains, is a trade-off to select an appropriate kinematic wave model. As one of the objectives of this thesis is to quantify the influence of using alternative (nonlinear) wave models, the linear Airy wave model will be used for comparison, since it is straightforward to implement and has been widely used in the offshore industry and scientific research. Wheeler stretching will be applied to stretch the velocity profile up to the actual surface, as this is the most commonly used and one of the best performing methods available. The methods that will be used should satisfy a number of demands:

- High accuracy
- Flexible
- Computationally inexpensive

- Straightforward implementation

For this thesis, only non-breaking waves will be considered. Within this regime, a wave model is to be used that has acceptable accuracy up to the breaking point. Furthermore, the method should be flexible, such that it is valid in both shallow and deeper water. Computational efficiency is rather important for this study for two reasons. First, the assessment of fatigue life requires a large number of simulations to capture all the contributions of individual load cases to fatigue damage. Second, the wave model is to be tested on sensitivity to changes in its input variables. Finally, since the emphasis of this thesis project should be on investigating the impact of using more sophisticated wave models rather than the implementation, the feasibility of realizing a model in the available time needs to be assessed.

Reformulating the demands leads to four criteria which can be evaluated in a trade-off table; Accuracy, flexibility, performance and complexity. Each criteria can then be given a score using the formulation in Table 2.3, after which the highest total score will indicate what method is the most appropriate for this thesis.

Table 2.3: Trade-off evaluation scores

Evaluation	$--$	$-$	$+/-$	$+$	$++$
Score	-2	-1	0	1	2

Nonlinear regular wave model trade-off

For nonlinear regular waves, three models were presented in Section 2.2.5. The analytical methods (Stokes and cnoidal theory) have been extended to 5^{th}-order, while the numerical Fourier approximation method can be used with any desired order. In Table 2.4, the evaluation of the three kinematic methods for nonlinear regular waves is shown.

The accuracy of the analytical methods is comparable, at least in the range in which they are valid. The Fourier method performs slightly better in the region where both Stokes and cnoidal theory lose some of their accuracy. As the analytical methods are complementary to each other, they receive a lower score than the Fourier method, which is more globally applicable except for the very shallow water limit. Considering the computer power available nowadays, the performance penalty when using the numerical Fourier method is almost negligible, so no distinction is made here. Finally, in terms of ease of implementation, cnoidal theory is clearly more complex than Stokes' method. The Fourier method is not as straightforward as Stokes method either, but the availability of an open-source C++ code by Fenton, based on his Fortran program described in [30], re-

Table 2.4: Trade-off table for nonlinear regular wave models

	Nonlinear regular wave model		
	Stokes 5$^{\text{th}}$-order	Cnoidal theory	Fourier approx.
Accuracy	$+/-$	$+/-$	$+$
Flexibility	$-$	$-$	$+$
Performance	$+/-$	$+/-$	$+/-$
Complexity	$+/-$	$-$	$+/-$
Final score	$\mathbf{-1}$	$\mathbf{-2}$	**2**

duces the required amount of programming considerably. As shown in Table 2.4, the Fourier method is the most appropriate method for nonlinear regular waves.

Nonlinear irregular wave model trade-off

By far the most frequently mentioned nonlinear irregular wave model in literature is the 2$^{\text{nd}}$-order perturbation model presented in Section 2.2.6. Different methods that have received moderate attention are the Hybrid wave and Boussinesq model, and various CFD approaches. Many alternatives exist, but since they are only seldomly referred to by researchers these methods are omitted in the trade-off. The CFD approach that is considered here, is the full-potential method [49] mentioned in Section 2.2.6, which has recently emerged as a relatively fast yet accurate method. The trade-off between the four selected methods is shown in Table 2.5.

Contrary to the nonlinear regular wave models, comparison between irregular nonlinear wave models in literature is scarce which makes the evaluation of the trade-off criteria more ambiguous. The accuracy of the hybrid wave model has been reported to be higher than the 2$^{\text{nd}}$-order model, although since it is a semi-empirical interpretation of the latter, scientists doubt the physical correctness of the method [40] and hence they score equally. Boussinesq and CFD method score higher, as these are able to accurately describe nonlinear waves up to the point of breaking. In terms of flexibility, these methods therefore also receive a higher score. Considering the computational performance no direct comparison has been found, although it is generally accepted that Boussinesq methods are very expensive and hence no engineering application is known to this date. The full-potential method is reasonably fast compared to more expensive CFD methods, but still more expensive than the hybrid and 2$^{\text{nd}}$-order method. Although tweaking is required [44], the 2$^{\text{nd}}$-order model is the least complex to implement,

Table 2.5: Trade-off table for nonlinear irregular wave models

	Nonlinear irregular wave model			
	2^{nd}-order	Hybrid wave	Boussinesq	CFD full-potential
Accuracy	$+/-$	$+/-$	$+$	$+$
Flexibility	$+/-$	$+/-$	$+$	$+$
Performance	$+/-$	$+/-$	$--$	$-$
Complexity	$+$	$+/-$	$--$	$-$
Final score	**1**	**0**	**-2**	**0**

followed by the hybrid wave model, which requires slightly more effort. The CFD method is considered complex, although the required discretization techniques are a well covered subject in literature, which is less valid for the at least equivalently complex Boussinesq method. It follows from the scores in the trade-off table that the 2^{nd}-order model is the preferable method to use for nonlinear irregular waves.

2.6.2 Final remarks on the model selection

In this chapter, the basic theory of wave kinematics and kinetics was presented, together with an overview of the available and most commonly used computational models and a discussion of design standards. A trade-off was performed to identify the most appropriate methods. Considering the limited time available in this thesis project for both implementation and running simulations and the requirement to be able to test a large amount of load cases, the selection procedure has been such that the emphasis of this thesis can be put on testing and analyzing various scenarios rather than the realization of a cutting-edge model for hydrodynamic loads.

Besides the nonlinear methods that were selected, the linear Airy wave model with Wheeler stretching will be implemented to be able to make comparisons with the traditional linear calculation procedure. As the use of nonlinear regular wave methods is already widely used in the industry, this thesis will mainly focus on the influence of a nonlinear wave model in *irregular* waves. An overview of the selected methods is presented in Table 2.6.

Table 2.6: Selected models based on the trade-off

<table>
<tr><th></th><th>Wave kinematics</th><th>Wave kinetics</th></tr>
<tr><td>Irregular waves (stochastic)</td><td>2^{nd}-order + Wheeler stretching</td><td rowspan="2">Morison equation + MacCamy-Fuchs correction</td></tr>
<tr><td>Regular waves (deterministic)</td><td>Fourier approximation</td></tr>
</table>

3

Model Formulation and Implementation

3.1 Introduction

In the previous chapter, an overview of the traditional and state-of-the-art methods to predict wave kinematics and hydrodynamic forces on an offshore support structure was presented. A trade-off was performed to select the most appropriate models to answer the research questions of this thesis. This resulted in the choice for a 2nd-order kinematic model, combined with the Morison equation to predict the hydrodynamic force. In order to be able to make a comparison with the traditional prediction techniques, the 1st-order linear model (Airy) is implemented to serve as a reference. The implementation of the methods results in a computer program which is able to produce wave load time series for a given set of input data. These wave load time series can subsequently be used as input for the aeroelastic wind turbine simulation tool BHawC, which is able to simulate the dynamic response of the complete wind turbine system.

This chapter describes in detail how the models have been implemented in a digital computing environment. The scientific environment Matlab®was used to realize the program, using object oriented programming. In Section 3.2 the structure of the program and its components is illustrated with flowcharts. Details about the implementation of the program components are given in Section 3.3. In that section, the efficient Inverse Fast Fourier Transform (IFFT) is introduced to increase computational performance, by performing the calculations in the frequency-domain. A Doppler shift due to a steady current however prohibits the direct use of the frequency-domain method. Therefore a method is proposed to account for the Doppler shift in the frequency discretization, such that the IFFT can be used.

3.2 Wave load calculation program structure

In this section, the basic structure of the program that has been realized will be shown. As was introduced in Chapter 2, the prediction of wave loads for a given sea condition can be divided into two main processes. For convenience, this separation between wave *kinematics* and *kinetics* is maintained in the structure of the wave load program, as shown in the flowchart in Figure 3.1. The most fundamental input parameters are those defining the sea conditions and structural geometry. Many more variables need to be specified, but for brevity these are omitted in this discussion. The typical output of the program is a wave load time series, containing the force per unit length acting on a number of vertical coordinates. This *wave load file* will subsequently serve as an external load input for the time-domain response simulations of the wind turbine generator in BHawC.

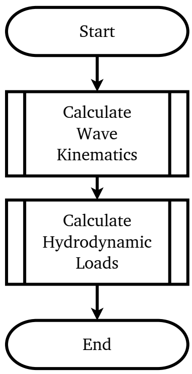

Figure 3.1: Flowchart of the wave load calculation program.

Besides being convenient from a programming point of view, the sharp division between the calculation of wave kinematics and hydrodynamic load is beneficial in terms of computational performance. One can assume that the presence of a support structure does not modify the particle velocities and accelerations that are to be used in the Morison equation in the kinetic module. In this case, kinematics for a given sea state only need to be calculated once, even if iterative hydrodynamic load calculations are to be carried out in a structural optimization routine. Since calculations on the wave kinematics are by far the most computationally expensive of the two modules, structural optimization can thus be performed without a high performance penalty.

As will be shown in Section 3.2.1, the structural diameter actually *does* enter the calculation of wave kinematics when the MacCamy-Fuchs diffraction correction on acceleration terms is applied. This in fact implies a violation of the assumption made above, but this is not severe for two reasons. First, the change of the diameter during structural optimization will often be relatively small compared to its initial design value. Second, for the currently common monopile diameters, the MacCamy-Fuchs correction mainly affects the higher frequency waves, which have a relatively low spectral density and hence have a small contribution to the total particle acceleration. Therefore, it is safe to assume that the changes in structural diameter during optimization do not modify wave kinematics.

3.2.1 Wave kinematics module structure

The first module in the wave load calculation program is the prediction of wave kinematics. In Figure 3.2, an global overview of the steps that are taken is presented in a flow chart. The most important input parameters are those that define the sea state, which are the significant wave height and the peak period of the wave spectrum. Also, the current is a significant input parameter, as this will influence both the fluid velocities and the frequency of encounter as experienced by the monopile. The output of the kinematics module is a time series of the horizontal flow velocities and accelerations, for a predefined number of vertical coordinates.

Following the flowchart, first a discrete range of N frequencies is defined. It is generally advised to use at least $N = 200$ frequency components to ensure the randomness of the wave simulation [58]. By introducing a maximum or cut-off frequency, the frequency range is limited and hence a denser frequency discretization can be achieved with the same amount of frequencies. Typically, a safe cut-off frequency is four times the peak frequency of the wave spectrum [33]. Although some energy from the wave spectrum is lost, the effect on the wave record realization is minimal since the energy of these high frequency waves is minimal and its contribution to the sea surface elevation is insignificant.

The summation of both linear 1st-order and the nonlinear 2nd-order model wave components to a time series is performed by the efficient Inverse Fast Fourier Transform (IFFT). All calculations required for the wave kinematics are therefore done in the frequency domain. The working principle of the IFFT and the model formulation in both time- and frequency-domain are discussed in Section 3.3. In that section it is also shown how the MacCamy-Fuchs diffraction correction can be applied to the kinematics.

In the flowchart, a decision model is included to decide whether an extreme deterministic wave is to be smoothly inserted into the stochastic wave record. Although the corresponding regular wave model and the insertion of the deterministic wave is not a subject of this thesis, it is included in the wave load model since the realization of an engineering tool is one of the goals of this project. The nonlinear regular wave model that is involved is discussed in Appendix B. Also, an insertion algorithm is proposed, since it has been experienced that wave load files from external parties often contain badly inserted extreme waves. This leads to strong jumps in the wave load distribution, which may have undesirable effects on the wind turbine response behavior.

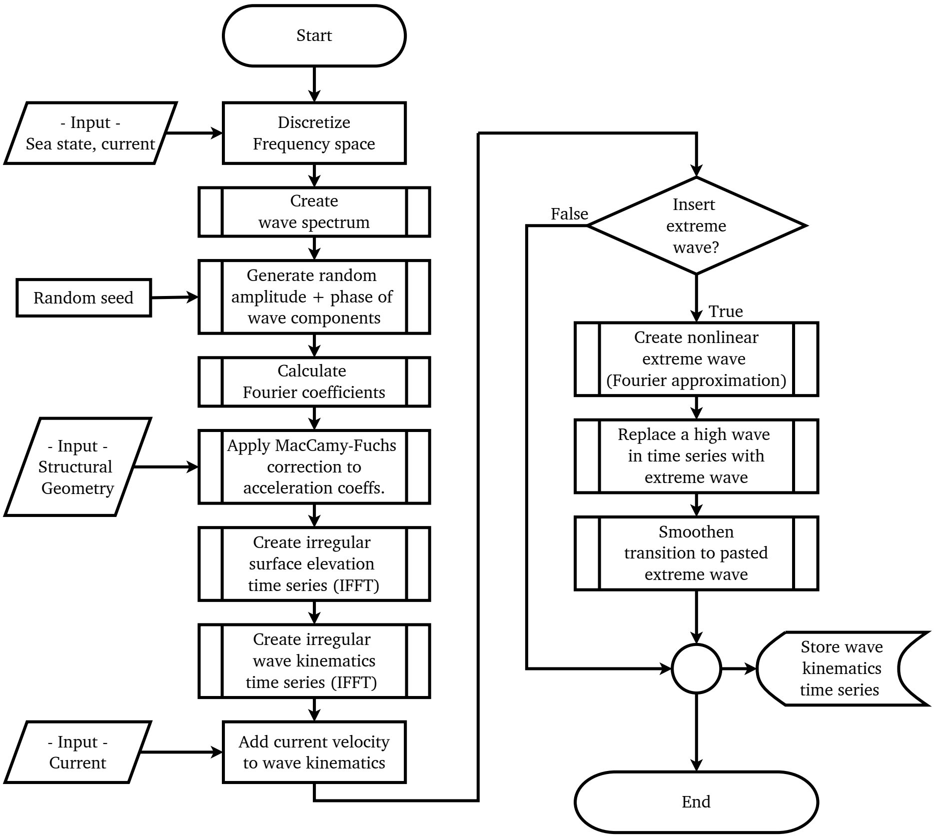

Figure 3.2: Flowchart of the wave kinematics module.

3.2.2 Hydrodynamic load module structure

The hydrodynamic load module is the second and final part in the wave load calculation program. The flowchart of this module is presented in Figure 3.2. This module calculates the distributed wave load time series from the wave kinematics, using the Morison equation (Eq. 2.69), and presents the output in a wave load file that can be processed by BHawC.

If structural motion is to be taken into account, the wave load of each time step is modified by the structural response. Since the wave load depends on the output from the response simulation in BHawC, the program should loop trough each time step and update the wave load file accordingly. In this thesis however, the wave load is assumed not to be coupled to the wind turbine response, so it is sufficient to generate the wave load file directly.

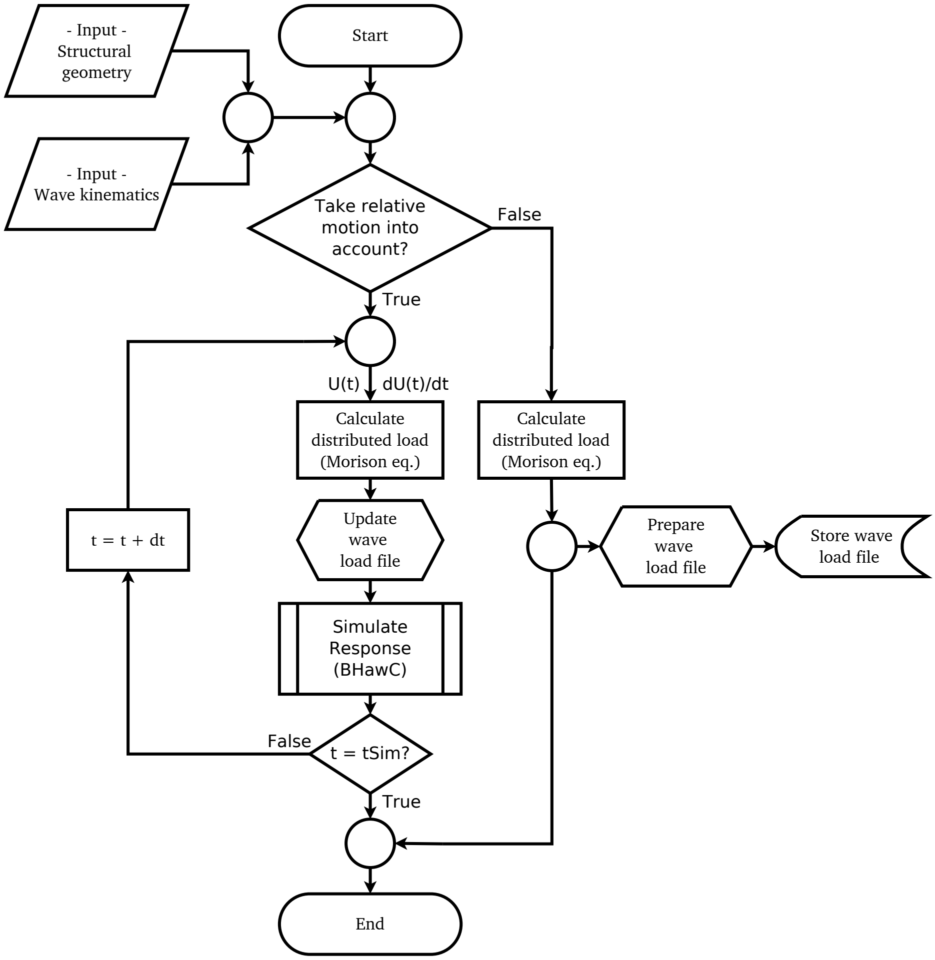

Figure 3.3: Flowchart of the wave kinetics module.

3.3 Model implementation

In this section, the realization of the wave load model is discussed. This starts with an overview of the analytical formulations of the 1^{st}- and 2^{nd}-order kinematic models. Since computational efficiency is strived for, the Inverse Fast Fourier Transform is introduced as an efficient way to perform summations in the frequency domain. As stated in the introduction of this chapter, the IFFT can not be used directly if the Doppler shift due to a steady current is to be taken into account. Therefore, a workaround is proposed which prepares the frequency components in a way that the IFFT can be used. Two possible sources of error which may affect the accuracy of the 1st- and 2nd-order simulations when using this method are identified.

3.3.1 Kinematic model formulations

As mentioned in the introduction of this chapter, the kinematic model comprises the linear Airy wave model with an additional second-order perturbation correction. As such, the second-order accurate surface elevation $\eta(x,t)$ is given by:

$$\eta(x,t) = \eta^{(1)}(x,t) + \eta^{(2)}(x,t) \tag{3.1}$$

where $\eta^{(1)}$ is the 1st-order accurate elevation from linear wave theory and $\eta^{(2)}$ is the 2nd-order contribution, which consists of a sum and a difference contribution. Analogous to the surface elevation, the velocity potentials corresponding to the surface elevation can be

$$\Phi(x,z,t) = \Phi^{(1)}(x,z,t) + \Phi^{(2)}(x,z,t) \tag{3.2}$$

For a monopile support structure the wave properties can be assumed to be independent of the spatial coordinate x, therefore x can be set to zero. The surface elevations and velocity potentials are therefore simply written as $\eta(t)$ and $\Phi(z,t)$, respectively. Below, the analytical expressions for the first- and second-order surface elevation and velocity potential are given. For convenience, the arguments in all trigonometric functions are given radians. It is assumed that a current has to be taken into account, and therefore a distinction is made between apparent and relative frequencies.

First-order linear wave model expressions

The 1st-order surface elevation can be expressed as follows:

$$\eta^{(1)}(t) = \sum_{m=1}^{N} a_m \cos(\omega_{\mathrm{A},m} t - k_m x - \phi_m) \tag{3.3}$$

Although $x = 0$ in the case of a monopile support structure, the x-dependent term is left in the expression for completeness, since the related velocity potential needs to be derived with respect to x to obtain an expression for the velocity. The wave number k_m is related to the relative frequency $\omega_{\mathrm{R},m}$ through the dispersion relation:

$$\omega_{\mathrm{R},m}^2 = g k_m \tanh(k_m d) \tag{3.4}$$

A unique solution for $k_m > 0$ can be found numerically, for example with Newton's method [73]. To accelerate convergence of the algorithm, an accurate initial estimate of the wave number is [30]:

$$(k_m)_{init} = \frac{1}{d}\frac{\alpha + \beta^2 \operatorname{sech}^2 \beta}{\tanh \beta + \beta \operatorname{sech}^2 \beta} \qquad \text{with:} \begin{cases} \beta = \alpha\sqrt{\coth \alpha} \\ \alpha = \dfrac{\omega_{\mathrm{R},m}^2 d}{g} \end{cases} \tag{3.5}$$

In Eq. 3.3, the phase angles ϕ_m are uniformly distributed between 0 and 2π. The amplitudes a_m follow from the Rayleigh distributed amplitude variances, where the expected value is obtained from the wave spectrum:

$$E(\tfrac{1}{2}a_m^2) = S(f_{\mathrm{R},m})\Delta f_{\mathrm{R}} \tag{3.6}$$

The spectral density $S(f_{\mathrm{R},m})$ and frequency bin widths $\Delta f_{\mathrm{R},m}$, are usually provided in the relative frame of reference, and are in Hz rather than radians per second here for convenience. This is done since the definition of the wave spectra in Chapter 2 is in Hz, which can be interpreted more intuitively than the angular frequency. The conversion is straightforward, since $\Delta f_{\mathrm{R},m} = \Delta\omega_{\mathrm{R},m}/(2\pi)$.

The 1st-order velocity potential that corresponds to the surface elevation given in Eq. 3.3 reads:

$$\Phi^{(1)}(z,t) = -\sum_{m=1}^{N} b_m \frac{\cosh k_m(z+d)}{\cosh k_m d}\sin(\omega_{\mathrm{R},m}t - k_m x - \phi_m) \tag{3.7}$$

where

$$b_m = \frac{a_m g}{\omega_{\mathrm{R},m}} \tag{3.8}$$

This velocity potential differs from the textbook example in Eq. 2.30. The argument of the sine of Eq. 2.30 has been multiplied by -1, and since $sin(x) = -sin(-x)$, this results in the velocity potential as displayed in Eq. 3.7. The reason for this manipulation is to make the reformulation required for the use in a Inverse Fast Fourier Transform, which is treated in Section 3.3.2, more transparent. Expressions for the 1st-order wave particle kinematics are obtained by deriving the velocity potential:

$$u^{(1)}(z,t) = \frac{\partial\Phi^{(1)}}{\partial x} = \sum_{m=1}^{N} b_m \frac{\cosh k_m(z+d)}{\cosh k_m d} k_m \cos(\omega_{\mathrm{A},m}t - k_m x - \phi_m) \tag{3.9}$$

$$\dot{u}^{(1)}(z,t) = \frac{\partial u^{(1)}}{\partial t} = -\sum_{m=1}^{N} b_m \frac{\cosh k_m(z+d)}{\cosh k_m d} k_m \omega_{\mathrm{R},m}\sin(\omega_{\mathrm{A},m}t - k_m x - \phi_m) \tag{3.10}$$

Note that formally, when deriving Eq. 3.9, the apparent frequency should be present in the amplitude of the acceleration terms (Eq. 3.10). However, since it is assumed that all expressions for the kinematics are to be calculated in the relative frame of reference, the apparent frequency only enters the arguments of the trigonometric functions afterwards.

Second-order perturbation expressions

The sum- and difference components of the 2nd-order perturbation to the surface elevation are given by:

$$\eta^{(2)}(t) = \sum_{m=1}^{N}\sum_{n=1}^{N}\left[a_m a_n\left\{B^-_{mn}\cos(\psi_{\mathrm{A},m}-\psi_{\mathrm{A},n})+B^+_{mn}\cos(\psi_{\mathrm{A},m}+\psi_{\mathrm{A},n})\right\}\right] \tag{3.11}$$

where $\eta^{(2)} = \eta^{(2-)} + \eta^{(2+)}$ and $\psi_{\mathrm{A},m}$ and $\psi_{\mathrm{A},n}$ are short notations of the same cosine argument as in Eq. 3.3:

$$\psi_{\mathrm{A},m} = \omega_{\mathrm{A},m}t - k_m x - \phi_m \tag{3.12}$$

The variables B^-_{mn} and B^+_{mn}, being transfer functions for the 2nd-order amplitude, depend on the wave properties traveling with the current in the relative frame of reference, and are expressed as follows:

$$B^-_{mn} = \frac{1}{4}\left[\frac{D^-_{mn} - (k_m k_n + R_m R_n)}{\sqrt{R_m R_n}} + (R_m + R_n)\right] \tag{3.13}$$

$$B^+_{mn} = \frac{1}{4}\left[\frac{D^+_{mn} - (k_m k_n - R_m R_n)}{\sqrt{R_m R_n}} + (R_m + R_n)\right] \tag{3.14}$$

where

$$\begin{aligned} D^-_{mn} = & \frac{\left(\sqrt{R_m} - \sqrt{R_n}\right)\ \left\{\sqrt{R_n}(k_m^2 - R_m^2) - \sqrt{R_m}(k_n^2 - R_n^2)\right\}}{\left(\sqrt{R_m} - \sqrt{R_n}\right)^2 - k^-_{mn}\tanh k^-_{mn}d} \\ & + 2\frac{\left(\sqrt{R_m} - \sqrt{R_n}\right)^2 (k_m k_n + R_m R_n)}{\left(\sqrt{R_m} - \sqrt{R_n}\right)^2 - k^-_{mn}\tanh k^-_{mn}d} \end{aligned} \tag{3.15}$$

$$\begin{aligned} D^+_{mn} = & \frac{\left(\sqrt{R_m} + \sqrt{R_n}\right)\ \left\{\sqrt{R_n}(k_m^2 - R_m^2) + \sqrt{R_m}(k_n^2 - R_n^2)\right\}}{\left(\sqrt{R_m} + \sqrt{R_n}\right)^2 - k^+_{mn}\tanh k^+_{mn}d} \\ & + 2\frac{\left(\sqrt{R_m} + \sqrt{R_n}\right)^2 (k_m k_n - R_m R_n)}{\left(\sqrt{R_m} + \sqrt{R_n}\right)^2 - k^+_{mn}\tanh k^+_{mn}d} \end{aligned} \tag{3.16}$$

The variables R_m, R_n, and the difference- and sum wave numbers k^-_{mn}, k^+_{mn} are given by:

$$R_m = \frac{\omega^2_{\mathrm{R},m}}{g} \tag{3.17}$$

$$k^-_{mn} = |k_m - k_n| \tag{3.18}$$

$$k^+_{mn} = k_m + k_n \tag{3.19}$$

The 2nd-order difference- and sum velocity potentials that correspond to the surface elevation perturbations read:

$$\Phi^{(2)}(z,t) = -\frac{1}{4}\sum_{m=1}^{N}\sum_{n=1}^{N}\left[b_m b_n \frac{\cosh k_{mn}^{\pm}(z+d)}{\cosh k_{mn}^{\pm} d}\frac{D_{mn}^{\pm}}{(\omega_{\mathrm{R},m} \pm \omega_{\mathrm{R},n})}\sin(\psi_{\mathrm{R},m} \pm \psi_{\mathrm{R},n})\right] \tag{3.20}$$

From the 2nd-order velocity potentials, the expressions for the difference- and sum kinematics can be derived:

$$u^{(2)}(z,t) = \frac{\partial \Phi^{(2)}}{\partial x} = \sum_{m=1}^{N}\sum_{n=1}^{N} Z_{mn}^{\pm}\cos(\psi_{\mathrm{A},m} \pm \psi_{\mathrm{A},n}) \tag{3.21}$$

$$\dot{u}^{(2)}(z,t) = \frac{\partial u^{(2)}}{\partial t} = -\sum_{m=1}^{N}\sum_{n=1}^{N} Z_{mn}^{\pm}(\omega_{\mathrm{R},m} \pm \omega_{\mathrm{R},n})\sin(\psi_{\mathrm{A},m} \pm \psi_{\mathrm{A},n}) \tag{3.22}$$

where the amplitude terms have been gathered in the variable $Z_{mn}^{\pm}$:

$$Z_{mn}^{\pm} = \frac{1}{4} b_m b_n \frac{\cosh k_{mn}^{\pm}(z+d)}{\cosh k_{mn}^{\pm}}\frac{D_{mn}^{\pm}}{(\omega_{\mathrm{R},m} \pm \omega_{\mathrm{R},n})} k_{mn}^{\pm} \tag{3.23}$$

3.3.2 The Inverse Fast Fourier Transform (IFFT)

The linear and second-order nonlinear irregular wave models in Section 3.3.1 are formulated in the time-domain. As a large number of waves is to be superimposed, especially the double-summations in the second-order model will be time consuming. To avoid the numerical inefficiency of performing summations in the time-domain, a better approach is to carry out the calculations in the frequency-domain and subsequently use the *Inverse Fast Fourier Transform* (IFFT) to realize a time series. The IFFT is an efficient digital implementation of the Fourier Transform, which is a technique to convert a signal in the time-domain to a spectrum in the frequency-domain, and vice versa. This relation is shown in Figure 3.4.

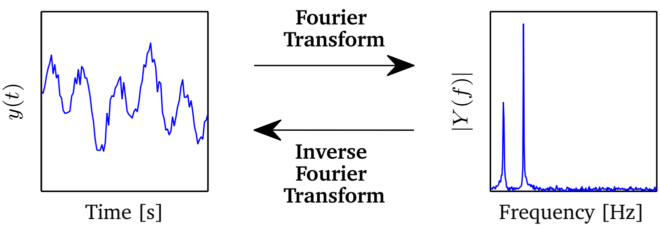

Figure 3.4: An illustration showing the conversion from a time series of a signal to a spectrum in the frequency-domain, and vice versa, using the Fourier Transform.

To show how the IFFT can be used, we consider the 1st-order surface elevation (Eq. 3.3). In a digital time-domain realization with a duration T, the continuous time t has to be discretized by creating a time vector $t_p = p\Delta t$, where $p = 1, 2, \ldots, N$ and the time step $\Delta t = T/N$. Similarly, an angular frequency vector can be defined such that $\omega_m = m\Delta\omega$, with $m = 1, 2, \ldots, N$. The discrete representation of the surface elevation then reads:

$$\eta^{(1)}(t_p) = \sum_{m=1}^{N} a_m \cos(\omega_{\mathrm{A},m} t_p - \phi_m) \tag{3.24}$$

Using Euler's complex exponential function, $\exp(i\phi) = \cos(\phi) + i\sin(\phi)$, Eq. 3.24 can be rewritten to:

$$\eta^{(1)}(t_p) = \Re\left\{\sum_{m=1}^{N} a_m \exp(-i\phi_m)\exp\left(i(m\Delta\omega_{\mathrm{A}})(p\Delta t)\right)\right\} \tag{3.25}$$

It can be shown [74] that the product of the terms $\Delta\omega_{\mathrm{A}}$ and Δt in the second exponential is equal to $\Delta\omega_{\mathrm{A}}\Delta t = 2\pi/N$, such that:

$$\eta^{(1)}(t_p) = \Re\left\{\sum_{m=1}^{N} X_\eta^{(1)}(\omega_{\mathrm{R},m})\exp\left(i\frac{2\pi m}{N}p\right)\right\} \tag{3.26}$$

Here we have gathered the amplitude and the first exponential in Eq 3.25 in a Fourier coefficient for the 1st-order surface elevation, $X_\eta^{(1)}$:

$$X_\eta^{(1)}(\omega_{\mathrm{R},m}) = a_m \exp(-i\phi_m) \tag{3.27}$$

The summation in 3.26 can be recognized as the inverse of the *Discrete Fourier Transform* (DFT) of $X_\eta^{(1)}$. This transform can be efficiently calculated using the IFFT algorithm [75], which has been widely established in many fields of science. Hence, the 1st-order surface elevation can be rewritten as:

$$\eta^{(1)}(t_p) = \Re\left\{\mathrm{IFFT}\left[X_\eta^{(1)}(\omega_{\mathrm{R},m})\right]\right\} \tag{3.28}$$

As shown in Eq. 3.26, the IFFT algorithm requires a frequency vector which is discretized in a number of equally sized bins with a width of $\Delta\omega$. In case the waves travel on a steady current, a Doppler shift needs to be taken into account, which will cause problems with the implementation of the IFFT. In Section 3.3.3, the nature of this problem will be addressed and a workaround is presented.

Cut-off frequency and aliasing

When the FFT is used to convert a discrete time series back to a spectrum in the frequency-domain, the frequency range of the output spectrum should be chosen carefully to avoid high frequency *aliases* of the original wave in the signal. This can be illustrated by the example in Figure 3.5. The original 1 Hz wave, sampled at time intervals of $1/6$ s will hence result in additional spectral peaks at 5 Hz and its higher frequency aliases.

To avoid this aliasing effect, a cut-off frequency should be used above which no frequencies will be taken into account. According to the Nyquist sampling theorem, this cut-off or Nyquist frequency is defined as $f_N = \frac{1}{2\Delta t}$. Conversely, when simulating waves the cut-off frequency of the wave spectrum should be chosen in accordance with the time step that shall be used. In case the 2$^{\mathrm{nd}}$-order interactions are taken into account in the simulation, one needs to realize that the sum-interactions will double the highest frequency that is present in the wave record realization, which implies that the time step may need to be reduced accordingly.

An everyday example of the aliasing effect can be observed on television. Rotating objects, such as spoked wheels on a wagon, can be perceived to rotate in the opposite direction due to the refresh rate of the television.

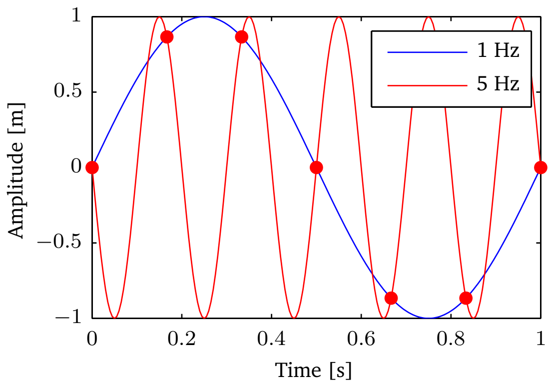

Figure 3.5: Illustration of the aliasing effect. If a 1 Hz wave is sampled at intervals of $1/6$ s, an FFT to the frequency-domain can also fit its 5 Hz *alias* to the sampling points.

3.3.3 Using the IFFT with a Doppler shift due to a current

For waves traveling on an arbitrary steady current U_C, the apparent frequencies as experienced by the monopile are related to the relative frequencies in the moving frame of reference and the Doppler shift ω_{D}, according to:

$$\omega_{\mathrm{A}} = \omega_{\mathrm{R}} + \omega_{\mathrm{D}} \ , \qquad \text{with: } \omega_{\mathrm{D}} = k\widetilde{U}_C \tag{3.29}$$

where $\widetilde{U}_C$ is the weighted mean current, given by:

$$\widetilde{U}_C = \frac{2k_m}{\sinh k_m d} \int_{-d}^{0} U_C(z) \cosh 2k_m(z+d) \ \mathrm{d}z \tag{3.30}$$

It can already be observed from Eq. 3.29 and 3.30 that the Doppler shift is a function of the wave number k_m and hence of the relative wave frequency. The relation between relative and apparent frequency is illustrated in Figure 3.6, in which three cases are distinguished for different current magnitudes. The relative frequencies are evenly distributed and range from 0 to 1 Hz and the water depth is 20 m. For cases (a), (b) and (c) the current magnitudes are $U_C = 0.15, -0.10$ and -0.20 m/s, respectively.

In the first case, the current is positive and hence in the wave propagation direction. The example shows that the Doppler shift ω_D mainly affects the higher frequencies. In cases (b) and (c) the current is negative and thus opposes the waves, where in (b) the current is relatively weak and in (c) relatively strong. An interesting observation is that if the opposing current is strong enough, the apparent frequency ω_A becomes double-valued, which means that two different relative frequencies can lead to the same apparent frequency.

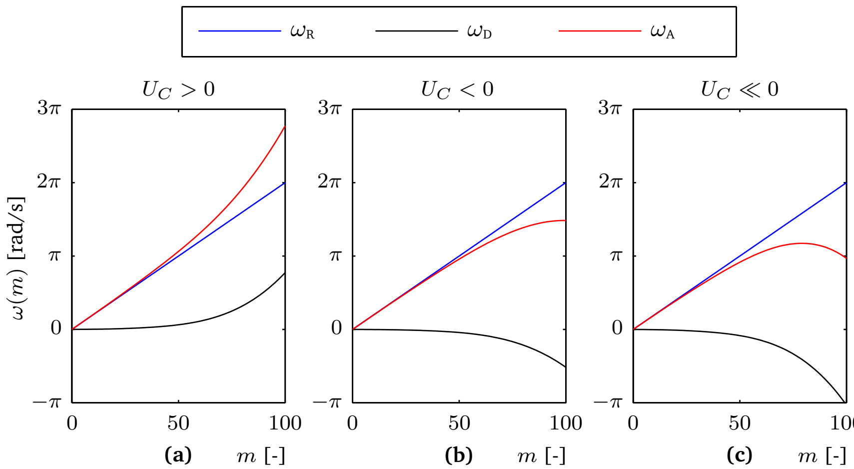

Figure 3.6: The Doppler shift ω_D due to three different current magnitudes U_C, calculated from the relative frequency $\omega_\mathrm{R} = m\Delta\omega_\mathrm{R}$ with $m = 1, 2, \ldots, 100$ and $\Delta\omega_\mathrm{R} = 2\pi/100$ rad/s. The apparent frequency $\omega_\mathrm{A} = \omega_\mathrm{R} + \omega_\mathrm{D}$ is not linearly related to m and therefore unsuited for a discrete IFFT. It can be observed that for strong opposing currents, $U_C \ll 0$, the apparent frequency becomes double-valued.

As shown in Section 3.3.2, the use of the efficient IFFT to realize a wave record requires a discrete frequency space which is evenly spaced. If the Doppler shift due to a current was to be ignored, one could directly discretize the relative frequencies and use the IFFT algorithm. However, modeling the incoming waves using their apparent frequency as experienced by the support structure is more realistic and is therefore prefered. This does complicate the implementation in the frequency-domain approach, since in this case it is required that the apparent frequencies have equally wide bins, rather than the relative frequencies. In

Figure 3.7, it is shown that a suitable apparent frequency discretization can not be achieved if the relative frequencies are evenly spaced.

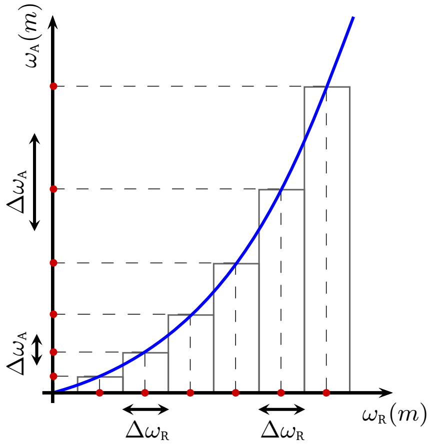

Figure 3.7: An illustration of the discretization of the relative frequencies $\omega_R = m\Delta\omega_R$. The relative frequency bins have a constant width of $\Delta\omega_R$, while the width of the apparent frequency bins $\Delta\omega_A$ depends on the index m. To use a discrete IFFT, evenly spaced apparent frequencies are required instead.

To overcome this inconvenience, first an apparent frequency space should be created such that $\omega_A = m\Delta\omega_A$. The corresponding relative frequencies can then be calculated using the following approximate Doppler shifted dispersion relation [52]:

$$\left(\omega_A - k\widetilde{U}_C\right)^2 = gk\tanh kd \tag{3.31}$$

Equation 3.31 can be solved for k numerically using for example Newton's algorithm. The apparent frequency range should be well chosen, such that the full wave spectrum in the relative frame of reference is present in the wave record realization, up to the predefined cut-off frequency. Furthermore, double-valued apparent frequencies should be dealt with, if these occur. Therefore, one should first Doppler-shift the desired relative frequency range to identify the maximum apparent frequency and a potential range of double-valued frequencies. In Figure 3.8, the same current magnitudes as in Figure 3.6 are used, but now the apparent frequencies are evenly spaced.

The problem of having double-valued apparent frequencies can be overcome by splitting the respective range in two parts, as is shown in Figure 3.8c. A proper choice for the initial estimate of k drives the solver of Eq. 3.31 to either of the solutions. A safe initial value of k to find a solution for the increasing part of the apparent frequency range is a small number, for example 1e-5. For the second solution, the wave number corresponding to the cut-off frequency could be used as an estimate.

As can be observed in Figure 3.8, the apparent frequency vector is now a linear function of m, and is therefore suited for the IFFT. The wave amplitudes of each apparent frequency component can be found from the spectral density and bin width of the corresponding relative frequency. The relative frequency bin widths $\Delta\omega_{\mathrm{R}}$ are now frequency dependent.

It must be remarked that especially if the apparent frequency is not monotonic, such as in Figure 3.8c, the relative frequencies are thin spread near the apparent frequency maximum. This is undesirable, because the wave description around this frequency will be less detailed. Fortunately, if double-valued apparent frequencies occur, this will mostly affect only the highest frequencies, which contain little energy. Nevertheless, it is recommended to use a denser frequency discretization in this case in order to ensure that a sufficient level of detail is present near the maximum apparent frequency.

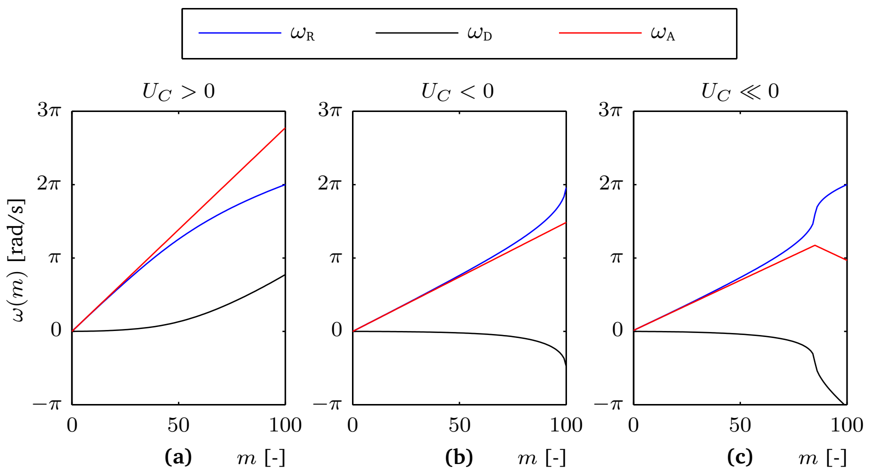

Figure 3.8: For the same scenarios as in Fig. 3.6, an approach in which the apparent frequency ω_{A} is a linear function of m and therefore suited for a discrete IFFT. The required relative frequencies ω_{R}, are calculated using the Doppler shifted dispersion relation, Eq. 3.31. The double-valued apparent frequencies for $U_C \ll 0$ are dealt with by splitting the apparent frequency domain in two parts.

3.3.4 Fourier coefficients

In order to be able to use the efficient IFFT, the kinematic models first needs to be reformulated in the frequency-domain rather than the time-domain. In this section the Fourier coefficients for both the first- and second order wave models are provided.

First-order wave model coefficients

Using the definition of the IFFT as described in Section 3.3.2, the Fourier coefficient of the 1st-order surface elevation $X^{(1)}_{\eta,m}(\omega_{\mathrm{R},m})$ is repeated for completeness:

$$X^{(1)}_{\eta,m} = a_m \exp(-i\phi_m) \tag{3.32}$$

For the sake of clarity $X^{(1)}_{\eta,m}(\omega_m)$ is simply written as $X^{(1)}_{\eta,m}$. In a similar way, the 1st-order horizontal velocity $u^{(1)}$ and acceleration $\dot{u}^{(1)}$ can be calculated using an IFFT:

$$u^{(1)}(z,t_p) = \Re\left\{\mathrm{IFFT}\left[X^{(1)}_{u,m}\right]\right\} \tag{3.33}$$

$$\dot{u}^{(1)}(z,t_p) = \Im\left\{\mathrm{IFFT}\left[X^{(1)}_{\dot{u},m}\right]\right\} \tag{3.34}$$

The corresponding Fourier coefficients read:

$$X^{(1)}_{u,m} = \frac{gk_m}{\omega_{\mathrm{R},m}}\frac{\cosh k_m(z+d)}{\cosh k_m d}X^{(1)}_{\eta,m} \tag{3.35}$$

$$X^{(1)}_{\dot{u},m} = -\omega_{\mathrm{R},m}X^{(1)}_{u,m} \tag{3.36}$$

Second-order wave model coefficients

The 2nd-order surface elevation components $\eta^{(2)}$, as defined by Eq. 3.11, can be discretized and rewritten to:

$$\eta^{(2)}(t_p) = \Re\left\{\sum_{m=1}^{N}\sum_{n=1}^{N} X^{(2)}_{\eta,mn}\exp\left(i\frac{2\pi(m\pm n)}{N}p\right)\right\} \tag{3.37}$$

Here, $n = 1,2,\ldots,N$ and the difference- and sum Fourier coefficients are given by:

$$X^{(2)}_{\eta,mn} = a_m a_n B^{\pm}_{mn}\exp(-i(\phi_m \pm \phi_n)) \tag{3.38}$$

To reduce the amount of computations, according to Agarwal [74] the double summation in Eq. 3.37 can be reformulated to a single summation with a replacement Fourier coefficients $Y^{(2)}_{\eta,j}$, such that:

$$\eta^{(2)}(t_q) = \Re\left\{\sum_{j=1}^{M} Y^{(2)}_{\eta,j}\exp\left(i\frac{2\pi j}{M}q\right)\right\} \tag{3.39}$$

which is in the correct format to calculate the 2nd-order surface elevation with an IFFT:

$$\eta^{(2)}(t_q) = \Re\left\{\mathrm{IFFT}\left[Y^{(2)}_{\eta,j}\right]\right\} \tag{3.40}$$

To make sure that the highest sum-frequencies will be represented, the number of samples has been doubled to $M = 2N$, and the index vector p has been replaced by $q = 1, 2, \ldots, M$. Accordingly, the time vector is now defined as $t_q = q\Delta t$.

The single summation Fourier coefficients $Y^{(2)}_{\eta,j}$ are obtained by collecting the original Fourier coefficients $X^{(2)}_{\eta,mn}$ for every possible combination of index pairs of m and n, for each value of j. For example, the index pairs that contribute to the sum interactions of $j = 4$, are $(m, n) = (1, 3), (3, 1)$ and $(2, 2)$. Similarly, also for the difference indices multiple combinations are possible. Since the IDFT formulation of the 2nd-order surface (Eq. 3.39) requires positive values of j, we define $j = |m - n|$. For the surface elevation, this is completely valid and no further manipulation is required, since $\cos(x) = \cos(-x)$. This means that for example the double-summation coefficients $X^{(2)}_{\eta,mn}$ with $(m, n) = (1, 2)$ and $(2, 1)$, both contribute to its single-summation counterpart $Y^{(2-)}_{\eta,j}$ with $j = 1$. Summarizing, the single-summation Fourier coefficients for the 2nd-order surface elevation can be collected as follows:

$$Y^{(2+)}_{\eta,j} = \begin{cases} 0 & j < 2, \\ \underbrace{\sum\sum}_{m+n=j} X^{(2+)}_{\eta,mn} & 2 \leq j \leq M. \end{cases} \tag{3.41}$$

$$Y^{(2-)}_{\eta,j} = \begin{cases} \underbrace{\sum\sum}_{|m-n|=j} X^{(2-)}_{\eta,mn} & 1 \leq j \leq (N-1), \\ 0 & j > (N-1). \end{cases} \tag{3.42}$$

The expressions for the 2nd-order kinematics, given in Eqs. (3.21) and (3.22), can be discretized to:

$$u^{(2)}(z, t_p) = \Re\left\{\sum_{m=1}^{N}\sum_{n=1}^{N} X^{(2)}_{u,mn} \exp\left(i\frac{2\pi(m \pm n)}{N}p\right)\right\} \tag{3.43}$$

$$\dot{u}^{(2)}(z, t_p) = \Im\left\{\sum_{m=1}^{N}\sum_{n=1}^{N} X^{(2)}_{\dot{u},mn} \exp\left(i\frac{2\pi(m \pm n)}{N}p\right)\right\} \tag{3.44}$$

with the double-summation Fourier coefficients

$$X^{(2)}_{u,mn} = Z^{\pm}_{mn} \exp\big(-i(\phi_m \pm \phi_n)\,\mathrm{sgn}(m \pm n)\big) \tag{3.45}$$

$$X^{(2)}_{\dot{u},mn} = -(\omega_{\mathrm{R},m} \pm \omega_{\mathrm{R},n}) X^{(2)}_{u,mn} \tag{3.46}$$

In Eq. 3.45, $\mathrm{sgn}(x)$ is the signum function, which is an odd function such that:

$$\mathrm{sgn}(x) = \begin{cases} -1 & \text{if } x < 0, \\ 0 & \text{if } x = 0, \\ 1 & \text{if } x > 0. \end{cases} \tag{3.47}$$

Using the procedure as described above for the 2$^{\text{nd}}$-order surface elevation, the expressions for the kinematics can be rewritten to a single-summation format. The velocities and acceleration perturbations can then be calculated by calculating the IFFT of the corresponding single-summation Fourier coefficients $Y_{u,j}^{(2)}$ and $Y_{\dot{u},j}^{(2)}$.

$$u^{(2)}(z, t_p) = \Re\left\{\mathrm{IFFT}\left[Y_{u,j}^{(2)}\right]\right\} \tag{3.48}$$

$$\dot{u}^{(2)}(z, t_p) = \Im\left\{\mathrm{IFFT}\left[Y_{\dot{u},j}^{(2)}\right]\right\} \tag{3.49}$$

The Fourier coefficients for the kinematics can be collected in a similar fashion as was shown above for the surface elevation.

As addressed in Section 3.3.3, the Doppler shift due to a current is frequency dependent, or in other words, the relative frequencies are not linearly related to index m. Therefore, strictly spoken, the apparent frequency of sum-interaction pair $\omega_{\mathrm{R},m} + \omega_{\mathrm{R},n}$ is not equal to the discretized apparent frequency $\omega_{\mathrm{A},j=(m+n)}$. However, one should bear in mind that the 2$^{\text{nd}}$-order perturbation works as a correction to the 1$^{\text{st}}$-order wave, and as such it has to travel *locked* to the 1$^{\text{st}}$-order waves in order to keep the correct phase during the entire simulation. Therefore it is justified to use the apparent frequencies as discretized by $\omega_{\mathrm{A}} = j\Delta\omega_{\mathrm{A}}$ in the arguments of the 2$^{\text{nd}}$-order expressions presented in this section.

The procedure to gather sum- and difference contributions with an equal frequency into single-summation Fourier coefficients, as described above, does however have a complication when a Doppler shift is to be accounted for. This can be explained by investigating the formulation of the 2$^{\text{nd}}$-order surface surface elevation, Eq. 3.11. Although the frequencies of the perturbations are linearly spaced for the IFFT, the *amplitudes* on the other hand are a function of the relative frequencies and hence are not exactly linearly related to the integer frequency indices m and n. Without a current causing a Doppler shift, the amplitudes are a linear function of the frequency indices, and therefore the collection of equal frequencies described above is fully exact.

In case this method is used with a Doppler shift, the amplitudes may not be collected into the single-summation Fourier coefficients correctly, which means that the proposed method is physically incorrect. It is expected however, that in many cases either the Doppler shift or 2$^{\text{nd}}$-order effects are relatively weak, and therefore the error is likely to be small. To test this hypothesis, in Chapter 4 the Doppler shifted frequency-domain approach proposed in this section will therefore be compared with the time-domain results, which are assumed to be exact.

3.3.5 MacCamy-Fuchs correction for diffraction

In Section 2.3.3, the MacCamy-Fuchs correction was introduced to account for linear diffraction effects in the Morison equation. As was shown in the flowchart for the wave kinematics module (Figure 3.2), the MacCamy-Fuchs diffraction correction is applied to the acceleration Fourier coefficients in the frequency-domain. The phase lag correction ϕ_{MCF} (Eq. 2.73) can easily be applied to the acceleration terms, but the modified inertia coefficient $\hat{C}_m$ requires some rewriting in order to be accounted for in the wave kinematics. To show how this is done, we first inspect the inertia force f_I in the Morison equation, $f_{Morison} = f_I + f_D$, in its form without structural motion:

$$f_I = \rho \frac{\pi D^2}{4} \hat{C}_m \dot{u} \tag{3.50}$$

where $\hat{C}_m$ is given by Eq 3.51 as

$$\hat{C}_m = \frac{4}{\pi (kD/2)^2 \sqrt{\left[J_1'(kD/2)\right]^2 + \left[Y_1'(kD/2)\right]^2}} \tag{3.51}$$

Since this corrected inertia coefficient has been derived for a cylinder in irrotational flow, the theoretical value of $C_M = 2$ [13]. Eq. 3.51 can therefore be reformulated as

$$\hat{C}_m = K_{\text{MCF}} C_M \tag{3.52}$$

where an inertia coefficient gain K_{MCF} has been defined such that:

$$K_{\text{MCF}} = \frac{2}{\pi (kD/2)^2 \sqrt{\left[J_1'(kD/2)\right]^2 + \left[Y_1'(kD/2)\right]^2}} \tag{3.53}$$

The inertia force component (Eq. 3.50) can therefore be rewritten to:

$$f_I = \rho \frac{\pi D^2}{4} K_{\text{MCF}} C_M \dot{u} \tag{3.54}$$

Since the gain K_{MCF} is a linear operator in the inertia force term, it can be applied to the acceleration amplitudes in an early stage. For example, we consider the Fourier coefficient for the 1st-order acceleration, Eq. 3.36. This coefficient can be worked out to:

$$X^{(1)}_{\dot{u},m} = -g k_m \frac{\cosh k_m (z+d)}{\cosh k_m d} \left[a_m \exp(-i\phi_m) \right] \tag{3.55}$$

Defining the MacCamy-Fuchs modified amplitudes and phase shifts, $\hat{a}_m$ and $\hat{\phi}_m$ respectively, as follows:

$$\hat{a}_m = a_m K_{\text{MCF},m} \tag{3.56}$$

$$\hat{\phi}_m = \phi_m + \phi_{\text{MCF},m} \tag{3.57}$$

the diffraction corrected 1st-order acceleration Fourier coefficients $\hat{X}^{(1)}_{\dot{u},m}$ are:

$$\hat{X}^{(1)}_{\dot{u},m} = -gk_m \frac{\cosh k_m(z+d)}{\cosh k_m d} \left[\hat{a}_m \exp(-i\hat{\phi}_m)\right] \tag{3.58}$$

This expression for the modified Fourier coefficients can be simplified to:

$$\hat{X}^{(1)}_{\dot{u},m} = X_{\text{MCF},m} X^{(1)}_{\dot{u},m} \tag{3.59}$$

Here, a convenient Fourier coefficient for the MacCamy-Fuchs correction has been introduced, which can be defined as:

$$X_{\text{MCF},m} = K_{\text{MCF},m} \exp(-i\phi_{\text{MCF},m}) \tag{3.60}$$

This is convenient, since the correction has now been completely applied in the kinematics module of the wave load model. For reasonably small changes in the structural diameter D, the difference in effect on the acceleration is negligible, and the kinematics can therefore be assumed independent of the monopile dimensions during structural optimization. Another advantage of the formulation used above, is that the inertia coefficient C_M is still present in the diffraction corrected Morison equation, since

$$\hat{f}_I = \rho \frac{\pi D^2}{4} C_M \hat{\dot{u}} \tag{3.61}$$

The effect of changes in the design value of C_M due to for example a different monopile surface roughness, can therefore be evaluated quickly with the Morison equation, without the need to recalculate the wave kinematics. Since the MacCamy-Fuchs correction is valid for linear diffraction effects only, the modification is only applied to accelerations of the 1st-order wave model. A follow-up research on the implementation of a similar correction for diffraction in 2nd-order waves is recommended.

4 Verification

4.1 Introduction

In the previous chapter, an overview was presented of the setup of the hydrodynamic load calculation program, the mathematical formulations of the irregular wave models used and the most important details about the implementation of these models. In this chapter, the results of the 1st-order reference wave model and the 2nd-order nonlinear model are analyzed to confirm that the program behaves as expected. In Section 4.2, several cases are studied to assess the simulation results of the sea surface elevation and hydrodynamic loads, both qualitatively and quantitatively. In order to make the comparisons as transparent as possible, the monopile is assumed clean with a constant diameter of $D = 6$ m and force coefficients $C_M = 2$ and $C_D = 1$. Extra attention is paid to the performance of the frequency-domain method in combination with a Doppler shift. This method has been devised in Chapter 3, but since some remarks were made on the accuracy due to the assumptions, comparisons with time-domain results are required to investigate whether the error is acceptable.

In Section 4.3, the verification of the wave models with wave load data of a wind farm in the German Bight is discussed. For this project, certified hydrodynamic loads were provided by a third party foundation contractor. Since the input parameters of both the wave model and the support structure geometry are well documented, a full set of wave load files could be reproduced to be checked against the results from the foundation contractor. The modeled structure represents a realistic monopile, which features secondary steel, marine growth and force coefficients that depend on both the vertical coordinate and the incoming wave direction. It must be emphasized that the primary goal of this verification is to confirm the correct implementation of the 1st-order reference wave model. A validation of the 2nd-order wave model results with measurement data from a full-scale offshore monopile foundation was anticipated, but has been cancelled eventually. The reason for not using these measurements was the lack of correlation between sea surface elevation measurements and strain data, which is caused by the large distance between the wave measurement buoy and the monopile.

To analyze results as a function of the frequency, a spectral representation of data is frequently used in this chapter. For the surface elevation, the wave energy or variance-density spectrum is convenient, since the wave spectrum is also an input parameter of the wave models. In order to compare hydrodynamic loads, the overturning bending moment M_y of the support structure at seabed level is considered, since this is proportional to the normal stress due to bending in the structure. In this case, the Power Spectral Density (PSD) and spectral power of the bending moment are used as a measure of energy per frequency bin and total energy that is transferred to the support structure, respectively [76].

Besides a verification of the wave loads themselves, the bending moments from dynamic response simulations in BHawC are compared to verify that the output is comparable. This is done by inspecting the equivalent fatigue loads. An equivalent fatigue load is not a primary design parameter, but it provides a simplified indication of the fatigue damage accumulated during the lifetime of a structure. This representation of fatigue damage in a single parameter allows a straightforward and quantifiable comparison of the dynamic response loads due to different wave load input. In this comparison, the equivalent fatigue loads due to bending moments in the tower and monopile are considered. Although in design different Wöhler slopes are used for each wind turbine component, a constant Wöhler slope of $m = 5$ was assumed for both the tower and monopile, such that a direct comparison of the entire supporting structure is possible.

4.2 Analysis of wave simulation results

In this section, the realized wave models are tested for various cases to investigate whether the output is sound. First, the variance-density spectra of both the 1$^{\text{st}}$- and 2$^{\text{nd}}$-order wave model sea surfaces are compared with a theoretical JONSWAP wave spectrum, and the influence of the wave model on the bending moment PSD is shown. Besides that, also the time-series of the 2$^{\text{nd}}$-order wave model is inspected for a regular and an irregular wave, to analyze the behavior of the 2$^{\text{nd}}$-order corrections in a qualitative way.

Second, the frequency-domain approach in which the Doppler shift is accounted for, as devised in Chapter 3, is compared to the time-domain results. Two possible sources of error have been identified in using this approach. In strong opposing currents, the relative frequencies locally suffer from a course discretization. The effect is investigated with the 1$^{\text{st}}$-order wave model. Furthermore, a Doppler shift may cause the amplitudes of the 2$^{\text{nd}}$-order wave model perturbations to be incorrectly collected in the single-summation Fourier coefficients. To assess whether this error limits the usability of the Doppler-shifted frequency-domain approach for 2$^{\text{nd}}$-order wave modeling, different sea states are tested to quantify the error.

4.2.1 Qualitative analysis of wave model output

The variance-density spectrum of the 1$^{\text{st}}$-order sea surface elevation should result in the same spectrum as the input spectrum that was used to obtain the wave amplitudes. As the amplitude variance is Rayleigh distributed, a large number of simulations is required to assure that the simulation is random enough and that average spectral density is smooth. Therefore, 500 simulations of 600 seconds have been performed, of which the average spectral density for each frequency is compared to the corresponding theoretical JONSWAP spectrum in Figure 4.1(a). The spectrum represents a sea state with a significant wave height of 8.1 m and a peak period of 13.1 s, where the JONSWAP peak-enhancement factor γ has a common value of 3.3. Besides that, the PSD of the bending moment at seabed level is shown in Figure 4.1(b), for a monopile with constant diameter of $D = 6$ m and force coefficients $C_M = 2$ and $C_D = 1$. Note that this bending moment PSD only represents the action of the Morison force on the monopile, and not the bending moment due to dynamic response loads.

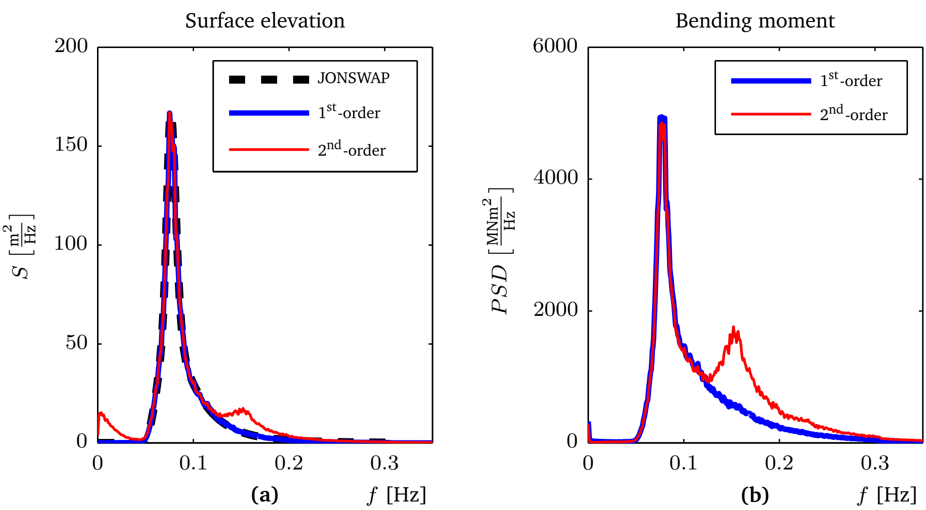

Figure 4.1: Comparison between the average spectral density of 500 sea surface simulations and a theoretical JONSWAP wave spectrum (a) with $\gamma = 3.3$, representing a sea state of $H_S = 8.1$ m and $T_P = 13.1$ s with a water depth of $d = 20$ m. Figure (b) shows the PSD of the bending moment at seabed level.

It can be observed from Figure 4.1 that the average of the 1$^{\text{st}}$-order simulations has almost converged to the JONSWAP spectrum, apart from some small ripples near the peak. From the spectral density of the 2nd-order surface elevation we can conclude that the spectral power of that model is higher than the theoretical and 1st-order model. The low frequency energy is added by the difference-interactions, while a second addition near 0.15 Hz follows from the sum-interactions, which as expected peaks at approximately twice the peak frequency. Although the 2nd-order model results in a higher spectral power than the theoretical JONSWAP shape, for this research it is assumed that the effect on the significant wave height is negligible. In the bending moment PSD, the influence of the sum-frequencies is clearly seen, as the spectral density due to the 2nd-order wave model is significantly higher around 0.15 Hz. The difference frequencies on the other hand hardly influence the bending moment PSD.

The wave spectrum shown in Figure 4.1 confirms that the 1st-order surface elevation is simulated as expected, and also the 2nd-order model appears to produce valid results, based on the spectra. In order to further assess whether the 2nd-order model performs as expected on a qualitative basis, the time series of the surface elevation are inspected. In Figure 4.2 two snapshots of a surface elevation time series are shown, the top figure (a) representing a regular wave and the bottom figure (b) an irregular wave. To illustrate the how the difference- and sum terms contribute to the 2nd-order wave, these are shown separately.

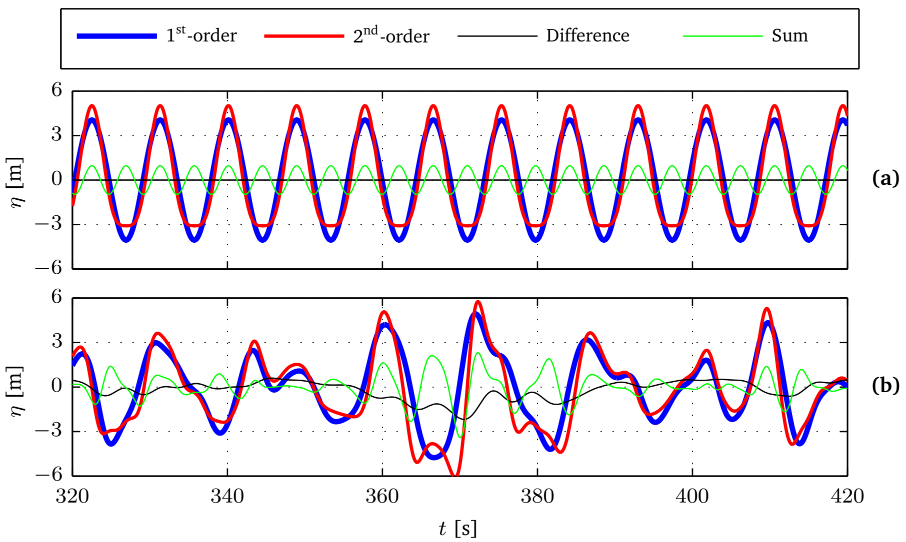

Figure 4.2: The 1st- and 2nd-order surface elevation for a regular (a) and an irregular wave (b). In the regular wave, only the sum interactions contribute to the 2nd-order wave perturbation, while in the irregular wave the difference interactions also play a role. Sea state: $H_S = 8.1$ m, $T_P = 13.1$ s, $\gamma = 3.3$ with $d = 20$ m.

The regular wave, which is obtained by using a Delta spectrum with one frequency as input, shows that the 2nd-order wave features the sharpened crests and flattened troughs that are typical for nonlinear regular waves. Since only one frequency is present, the difference terms do not contribute to the nonlinear wave and the sum interactions have exactly twice the frequency of the 1st-order wave. Hence in this case, the 2nd-order wave model works in the same way as the 2nd-order Stokes method for regular waves (Section 2.2.5).

Contrary to the regular wave, the difference terms do contribute to the 2nd-order wave in the irregular sea surface. It can be observed that as predicted, the difference interactions produce a long wave that causes a setdown of the water level below high wave groups and a slight water level rise in the calmer parts of the sea surface. The sum interactions are again responsible for sharper crests and flattened troughs, which results in steeper waves that are common in relatively shallow water.

4.2.2 Doppler-shifted frequency-domain method accuracy

In Section 3.3.3, a method is devised to allow the use of an IFFT in combination with a current, which causes a Doppler-shifted apparent frequency. Two sources of error were identified. First, for strong opposing currents, the relative frequency discretization will be coarse around the point at which the apparent frequency decreases with the wave number (see Figure 3.8c). This may lead to a local loss of accuracy. Second, it was concluded in Section 3.3.4 that the perturbation correction amplitudes of the 2nd-order wave model may be erroneous, since these may be related to incorrect relative frequencies. Below these two problems are addressed and the errors quantified.

Influence of coarse frequency discretization in strong opposing currents

To quantify the impact of the locally poor relative frequency density, the Doppler-shifted frequency-domain approach from Section 3.3.3 is compared with its time-domain equivalent for the 1st-order wave model. The time-domain approach serves as a benchmark, since in that case the relative frequencies are equally spaced.

Since the Doppler shift is most prevalent in high frequency wave components, a calm sea state is required to make sure that the maximum apparent frequency is in the part of the wave spectrum that contains significant wave energy. Therefore, this case study is performed on a low wind speed scenario from the verification project, where a strong current with a 50-year return period is applied in a direction opposing the wave propagation. In Figure 4.3, the averaged wave energy spectra and bending moment PSDs of 500 simulations in the frequency- and time-domain are shown. Besides that, the averaged results of 500 simulations without a Doppler shift are displayed, to show the impact of ignoring the Doppler shift in a calm sea.

It is observed that when taking the Doppler shift into account, the surface elevation spectrum is Doppler-shifted as well, which results in a lower apparent

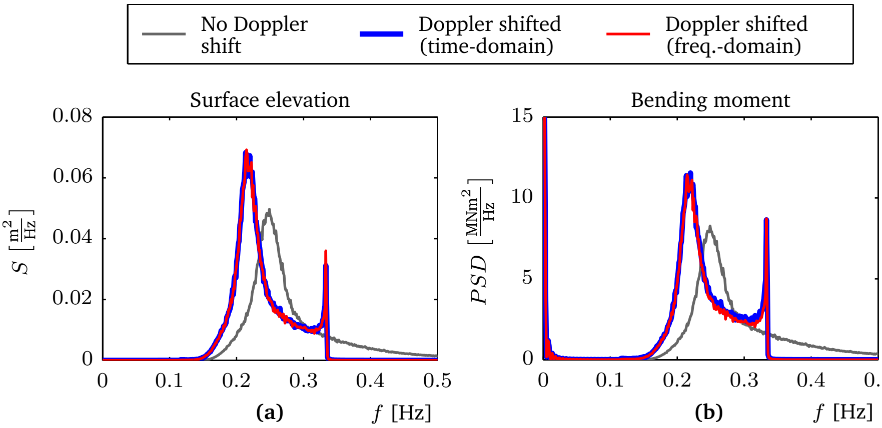

Figure 4.3: Comparison of different calculation approaches of the 1st-order wave model with a 0.69 m/s strong opposing current. Shown are the average wave energy spectrum (a) and bending moment PSD (b) of 500 simulations. Sea state: $H_S = 0.25$ m, $T_P = 4.05$ s and $\gamma = 3.3$.

peak frequency. Furthermore, it can be seen that at the maximum apparent frequency, which is approximately 0.33 Hz, a second peak is present. This can be explained from the fact that a wide range of relative frequencies is close to the maximum apparent frequency (see Figure 3.6c). The peak in the bending moment PSD near $f = 0$ Hz can be explained by considering that the steady current velocity causes a constant drag force on the monopile, which results in an offset of the average bending moment.

From both the surface elevation spectrum and the bending moment PSD, it appears that the frequency-domain approach delivers results that are close to the time-domain. This conclusion is further confirmed when the average spectral power of the bending moment is compared. In Table 4.1 the bending moment spectral powers have been normalized with the Doppler-shifted time-domain result. Compared to the time-domain results the frequency domain approach shows a slightly lower spectral power, with a difference of 2.3% . It must be noted here that for this case study, the MacCamy-Fuchs correction was switched off to emphasize the wave action by higher frequencies. When this diffraction correction is used in the simulations, the difference between both approaches will be lower due to the attenuation of high frequency inertia forces.

Finally, an interesting observation is that in a calm sea state with a relatively strong current, the Doppler shift has a significant influence on the frequency at which the support structure is excited. Neglecting the Doppler shift of hydrodynamic loads, which has been done by the foundation contractor of the verification project, may thus have an impact on the dynamic response and hence on fatigue life of the support structure.

Table 4.1: Normalized bending moment spectral power of the different modeling approaches of the 1st-order wave model, as shown in Figure 4.3. The Doppler-shifted time-domain result is set to 100 %.

Modeling approach	Bending moment Spectral power [%]
No Doppler shift	97.12
Time-domain + Doppler	100
Freq.-domain + Doppler	97.70

Error in 2nd-order wave model perturbation amplitudes

The second possible source of error is due to incorrect amplitudes in the 2nd-order wave model when the Doppler-shifted frequency-domain approach is used (see Section 3.3.4). Below, the method is tested against results from time-domain simulations. Since the latter method is rather computationally expensive, the number of frequencies has been lowered to 200 and the number of simulations in the time-domain is reduced to 75.

The first sea state represents a case in which 2nd-order interactions are presumed to be significant. Therefore, a rough sea state of the verification project, with a significant wave height of $H_S = 8.5$ m and a peak period of $T_P = 12.87$ s is selected. Acurrent of 0.69 m/s is assumed to be co-flowing with the waves. In Figure 4.4 the resulting wave energy spectrum and bending moment PSD are shown of both the 1st-order wave model and the 2nd-order model in time- and Doppler-shifted frequency domain. It appears that in this case the spectra of Doppler-shifted frequency-domain approach do not deviate much from the time-domain results. This is confirmed by the total bending moment spectral power shown in Table 4.2, since the difference between both approaches is smaller than 1%.

The second sea state that is investigated, is a case in which both the Doppler shift and 2nd-order interactions are significant. To achieve this, the sea state and water depth are changed to $H_S = 2.25$ m, $T_P = 6.0$ s and $d = 6$ m, while the same current as in the previous example is maintained. This yields the results shown in Figure 4.5. It is observed that although the sea surface elevation obtained with the Doppler-shifted frequency-domain approach shows a good match with the time-domain results, the bending moment PSD in general is considerably lower. The normalized bending moment spectral power, shown in Table 4.2, only confirms this observation.

It is obvious that in this case, the 2nd-order results from the Doppler-shifted frequency-domain method proposed in Section 3.3.3 fails to accurately repro-

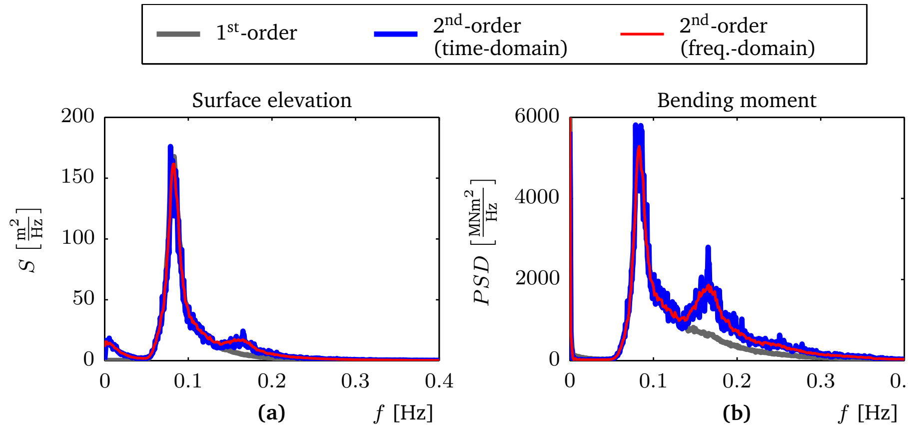

Figure 4.4: Comparison between 2nd-order modeling approaches in moderately deep water with a 0.69 m/s strong co-flowing current (Sea state 1). Shown are the average wave energy spectrum (a) and bending moment PSD (b). Sea state: $H_S = 8.5$ m, $T_P = 12.87$ s, $\gamma = 3.3$, with $d = 20$ m.

duce the 2nd-order time-domain results. However, it should be mentioned that although the results from this approach are less accurate, still the spectral power is higher than what would be achieved with a 1st-order simulation. Nevertheless, in cases in which both the Doppler shift and 2nd-order effects are significant, the time-domain approach is preferred. Since the time-domain approach is significantly slower, an assessment of the difference between the two approaches for a full load case simulation is strongly advised.

4.3 Verification with an existing project

The final objective of this thesis is to establish the influence of nonlinear irregular wave modeling on dynamic response, using the results of a full simulation where all the design load cases (DLC) required by IEC Standards [71] are included. A summary of the DLCs that are defined by a unique sea environment is provided in Appendix C. These DLCs form the basis of the wave load files that are created, which in turn are used as input for the BHawC dynamic response simulations. In this section, the results from simulations with input generated by the developed wave models are compared with previously obtained simulation results for an existing wind farm. These simulations were run with certified wave loads from a third-party foundation contractor.

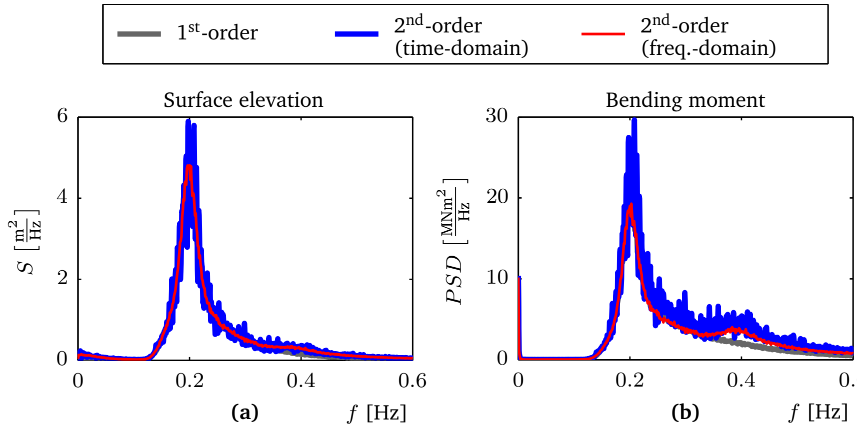

Figure 4.5: Comparison between 2nd-order modeling approaches in very shallow water with a 0.69 m/s strong co-flowing current (Sea state 2). Shown are the average wave energy spectrum (a) and bending moment PSD (b). Sea state: $H_S = 2.25$ m, $T_P = 6.0$ s, $\gamma = 3.3$, with $d = 6$ m.

4.3.1 Description of the verification project

The wind farm chosen for the verification is situated in the German Bight in the North Sea, where the water depth is approximately 25 m. For this project, full documentation of the input parameters was available, which allowed a complete reconstruction of the sea environment and structural geometry. This comprises the significant wave heights, peak periods, currents, water levels and deterministic wave characteristics used in every DLC, further specified in Appendix C. The monopile is defined by a discretization of the structural diameter and force coefficients in the axial direction, in all of which marine growth and appurtenances are accounted for. Furthermore, the equivalent drag coefficient (see Section 2.5.4 is calculated for 12 wave direction sectors, since the orientation of appurtenances with respect to the incoming flow influences the drag coefficient. Due to the confidential nature of these data, the input parameters used in the hydrodynamic load model are not provided in this report.

4.3.2 Comparison of Normal Sea State wave loads

To assure that the wave characteristics and hydrodynamic loads of the stochastic time series are correct, the output of the developed wave models is compared to the information extracted from the certified wave load files by the foundation designer. The comparisons here are made for DLC 1.2, which is used for fatigue analysis and comprises 108 wave load files per wind speed. In Figure 4.6, the significant wave height and significant wave period T_S, obtained from the sea surface signals, are compared. The significant wave period is used here for a

Table 4.2: Comparison of the normalized bending moment spectral powers of the Doppler-shifted 2nd-order wave model using different modeling approaches, corresponding to the sea states shown in Figures 4.4 and 4.5. The 1st-order time-domain solution is set to 100 %.

Modeling Approach	**Bending moment spectral power [%]**	
	Sea state 1	Sea state 2
1st-order (time-domain)	100	100
2nd-order (time-domain)	128.72	139.03
2nd-order (freq.-domain)	127.89	109.47

better period comparison of the energy-containing waves. It is observed that the results show a good match with the certified sea surface elevation parameters.

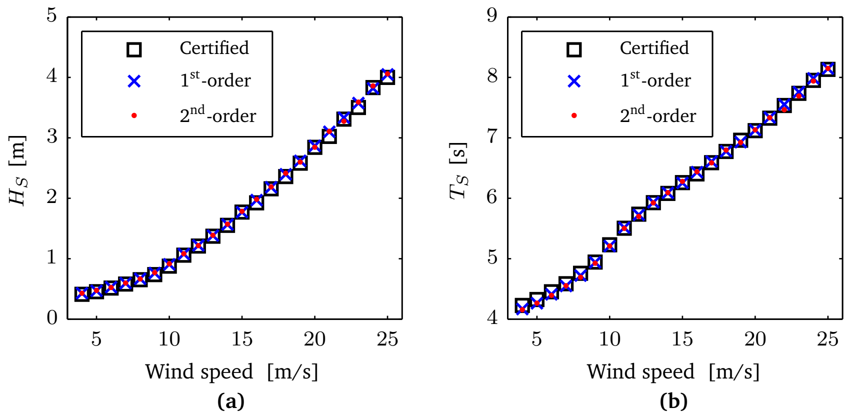

Figure 4.6: Verification of the significant wave height H_S (a) and period T_S (b) with results from certified simulations. Shown are the averages of 108 NSS simulations per wind speed (DLC 1.2).

Prior to performing the dynamic response simulations, the overturning bending moment and the corresponding equivalent fatigue load can be compared, based purely on the wave load input. These results are shown in Figure 4.7. The overturning bending moment, which provides an indirect check of the calculated wave kinematics, reveil that especially in the high wind scenarios the bending moment is structurally lower than for the certified case. This is suspicious since the surface elevation did show a good match. A close inspection of the certified wave loads reveiled that in those files no correlation between surface elevation

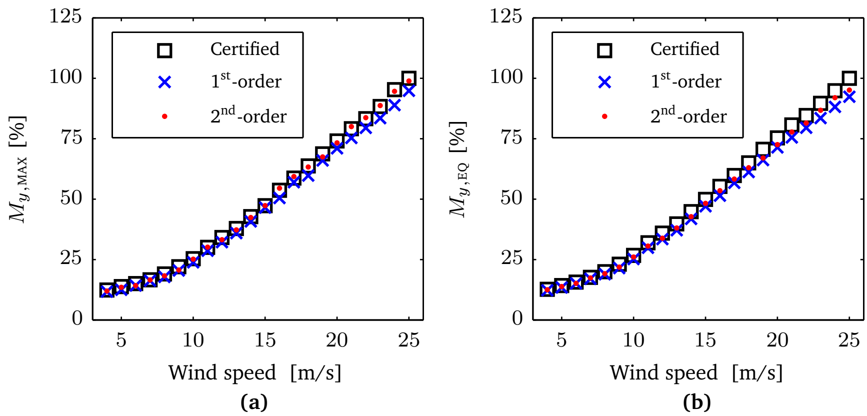

Figure 4.7: Verification of the overturning bending moment at seabed level: Maximum values $M_{y,\text{MAX}}$ (a) and equivalent fatigue loads $M_{y,\text{EQ}}$ (b). Bending moments are obtained from wave load input only, and are normalized by the average certified value for a 25 m/s wind speed. Shown are the averages of 108 NSS simulations per wind speed (DLC 1.2).

and bending moment exists, which is peculiar at least. One explanation for this difference could be a phase shift between the surface elevation and wave kinematics. If that is the case, the Wheeler stretching technique may be redistributing the velocity and acceleration profiles to a set of vertical coordinates belonging to an incorrect surface elevation. Since no details about the implementation techniques applied by the foundation designer are available, no conclusive evidence exists to prove this statement. Besides this, it is observed that the 2$^{\text{nd}}$-order wave model yields slightly higher bending moments, as expected.

4.3.3 Comparison of Severe Sea State wave loads

Similarly as for the Normal Sea State, the implementation of the deterministic waves is verified. This is done using the Severe Sea State (SSS) design load case, DLC 1.6. In this load case for ultimate strength analysis, 6 SSS simulations are performed per wind speed, since only one wave sector (worst) is used. In Figure 4.8, the maximum wave height H_{MAX} and the maximum overturning bending moment $M_{y,\text{MAX}}$ are shown.

It is observed that the maximum wave height matches well with the certified waves. Only in some wind speed cases, the maximum wave height was found to be slightly higher than the deterministic wave height. An inspection of the wave elevation time records reveiled that for some wave seeds, the wave height in a group of high irregular waves was actually higher than the deterministic regular wave that was inserted. Although this did not lead to a higher wave load, since the highest loads were still caused by the deterministic wave, more realistic

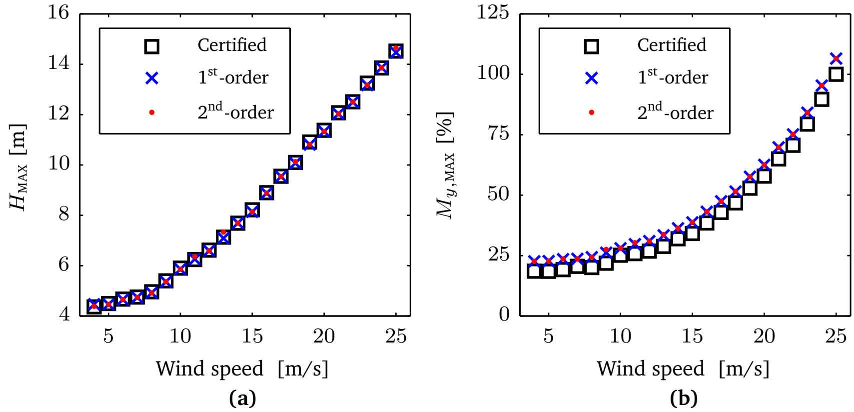

Figure 4.8: Verification of the deterministic wave simulations: Maximum wave height H_{MAX} (a) and normalized maximum overturning moment $M_{y,\text{MAX}}$ (b). Shown are the averages of 6 SSS simulations per wind speed (DLC 1.6).

results may be achieved when the deterministic wave is inserted at the exact spot of the highest wave in the stochastic record.

The bending moments of the SSS wave records show a difference which increases slightly with the height of the deterministic waves. A number of reasons for this difference can be identified, both due to presumed mistakes in the certified deterministic waves and due to uncertainties in the implementation of the deterministic wave model used in the developed model. These possible mistakes and uncertainties are further addressed in Section B.2 in Appendix B.

4.3.4 Comparison of dynamic response loads

Up to this point, the verification against certified simulations was performed purely on the simulated wave loads that serve as input for the BHawC simulations. This section therefore discusses the results of the dynamic response simulations, which comprises a full set of design load cases. Due to the focus of this thesis on irregular wave modeling, and the uncertainty about the correctness of the deterministic wave modeling observed above, the comparison is limited to the analysis of equivalent fatigue loads due to bending moments.

In the previous comparisons the overturning bending moment was considered to quantify the resultant hydrodynamic load. This overturning moment was taken about the axis parallel to the wave crests. In the dynamic response simulations performed by BHawC, a different coordinate system is used, as displayed in Figure 4.9. This coordinate system is defined with respect to the wind direction, rather than wave propagation direction. The bending moments of interest from the BHawC simulations are M_x and M_y, which represent the moments about the axes perpendicular and parallel to the wind direction, respectively. These bend-

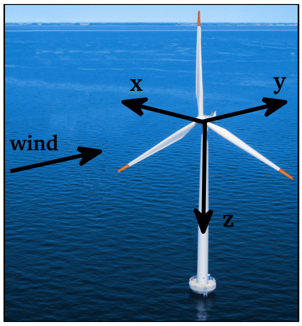

Figure 4.9: The coordinate system used in BHawC.

ing motions are also referred to as fore-aft and side-side bending, respectively.

For the verification of wave input by an analysis of dynamic response loads, the BHawC simulations with 1st-order waves are compared with existing results from simulations with the certified wave loads. In this comparison, the equivalent fatigue loads of the bending moments M_x and M_y in both the tower and the monopile are considered. To give an impression of the variation with height, the

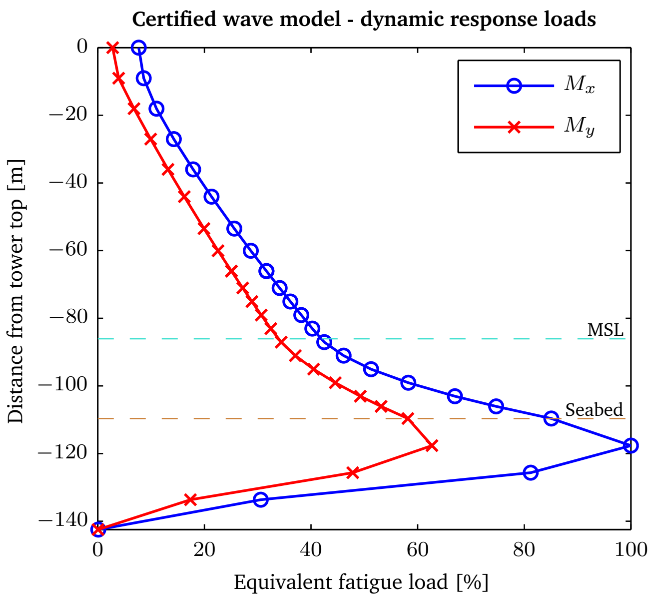

Figure 4.10: Impression of the equivalent fatigue load distribution throughout the supporting structure, from response simulations with certified wave loads. Normalized by the maximum value.

equivalent fatigue loads from the certified simulations are depicted as a function of the distance from the tower top in Figure 4.10. On each of these nodal locations, the equivalent fatigue load is normalized by the maximum value, which occurs in M_x at the node below the sea bed.

It can be observed from Figure 4.10 that the highest fatigue damage is caused by the fore-aft bending moment, M_x. In both M_x and M_y, the node below the seabed is the most sensitive to fatigue accumulation. Furthermore, it is observed that the monopile, which roughly comprises the bottom section of the supporting structure below MSL, is affected more by fatigue than the tower.

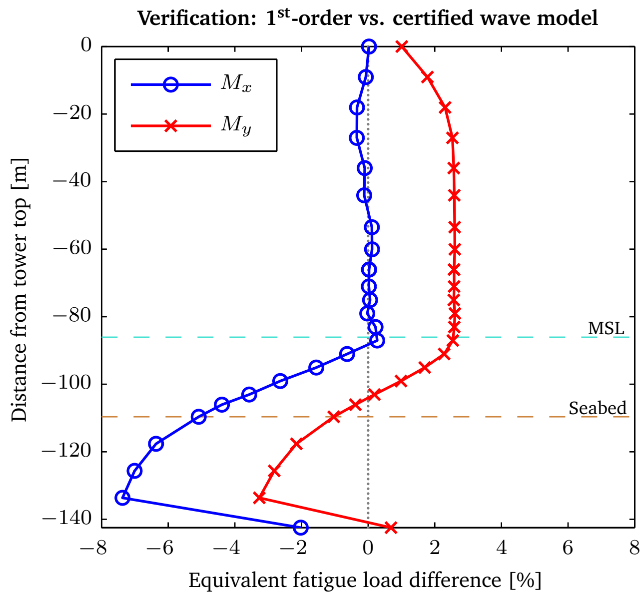

Figure 4.11: Verification of the equivalent fatigue loads from response simulations with 1$^{\text{st}}$-order wave model loads. The graph shows the relative difference with respect to the certified simulations on each node (Figure 4.10).

The comparison between simulations with 1$^{\text{st}}$-order and certified wave loads is shown in Figure 4.11. In this figure, the difference between the equivalent fatigue loads of both response simulations is shown as a percentage of the absolute values of the certified simulation, shown in Figure 4.10. It can be observed that the fore-aft bending moment leads to significantly lower equivalent fatigue loads in the submerged section, especially below the seabed. This is expected, since in the previous section it appeared that the equivalent fatigue loads at seabed level, purely based on wave action, was slightly lower for the 1$^{\text{st}}$-order model wave loads than for the certified loads (see Figure 4.7b). The side-side equivalent fatigue loads show the same pattern as the fore-aft loads, though with a slight offset to a positive difference.

In general, the 1st-order wave model developed for this project shows results that are relatively comparable to the certified wave model. The differences noticed in the equivalent fatigue loads of the bending moments, both purely due to wave action and due to the dynamic response, may be explained by the lack of correlation between surface elevation and wave loading in the certified wave load calculations. This has probably led to the application of Wheeler stretching of velocity and acceleration profiles to an incorrect surface elevation, which results in slightly different wave loads.

5 Results and Analysis

5.1 Introduction

In the previous chapters, the linear and nonlinear wave models were presented and a verification was performed. Since the wind farm that was used for verification is situated in shallow water, where nonlinear wave effects are expected to be significant, this project is suitable to form the basis for the main comparison between the wave model simulations and some additional case studies. Also the fact that the input settings that are used for this project represent a realistic support structure, including appurtenances and marine growth, supports the choice to use this wind farm.

This chapter first gives an overview of the simulation cases that were devised to carry out the comparison, a sensitivity study and two case studies on deterministic waves. These simulation cases are then discussed and analyzed in detail in the sections following the overview.

5.2 Overview of simulation cases

For this thesis project, several simulation cases were devised, which are summarized in Table 5.1. The verification and comparison simulations use the default input of the wind farm in question, specified in the third-party documentation of the wave load calculations. The simulation with the certified wave loads, which was used for the verification, is included in the simulation table for completeness with identifier A0. Except for the case studies on deterministic waves, a full set of design load cases (DLC) is simulated in BHawC for every scenario.

Besides the comparison between linear and nonlinear waves, which are named A1 and A2 respectively, a second category of simulation cases has been devised.

Table 5.1: An overview of the simulation cases, which are performed on the wind farm also used for verification.

Case study	Sim. ID	Wave Kinematics	Details
Verification & Comparison	A0	Certified	
	A1	1^{st}-order	Default input
	A2	2^{nd}-order	
Influence of wave spectrum shape	B1	1^{st}-order	$\gamma = 1$ (PM spectrum)
	B2	2^{nd}-order	
	B3	1^{st}-order	$\gamma = 7$
	B4	2^{nd}-order	
Influence of Doppler shift	C1	1^{st}-order	With Doppler shift
	C2	2^{nd}-order	
Discontinuity determ. wave	D1	-	Original (D1) vs. modified (D2)[1]
	D2		
Negative accel. determ. wave	E1	$\dot{u} = -\dot{u}$	DLC 6.1 (ESS), one modified seed

[1] Limited to two wave load files from a third-party (D1). In the modified files (D2), the discontinuity in wave force at the insertion point is smoothed.

This category comprises a set of scenarios for a sensitivity study on the impact of changes in the input parameters and the modeling approach. For simulations B1 to B4, the shape of the JONSWAP spectrum is changed, by modifying the peakedness-parameter from the default value of $\gamma = 3.3$ to either $\gamma = 1$ or $\gamma = 7$. For $\gamma = 1$, the shape effectively becomes a PM-spectrum, which embodies a fully developed sea state. The high value of γ is considered to be the upper limit of this parameter, which basically represents a very young sea state. The input spectrum is expected to have some influence of the degree of nonlinearity of the waves [77], which motivates a detailed investigation. An illustration of the resulting spectral shapes is given in Figure 5.1.

In simulations C1 and C2, the impact of a different approach to model the current is investigated. In the default case, the current is assumed to always act in the direction of the waves, and the Doppler shift is ignored. Especially the former assumption is conservative, since at many sites currents reverse every half-period of tidal motion. In this case study, the current direction is therefore alternated between co-flowing and opposing for each wave seed. Contrary to the default setup, also the Doppler shift is accounted for. This is done using the Doppler-shifted frequency-domain method described in Chapter 3.

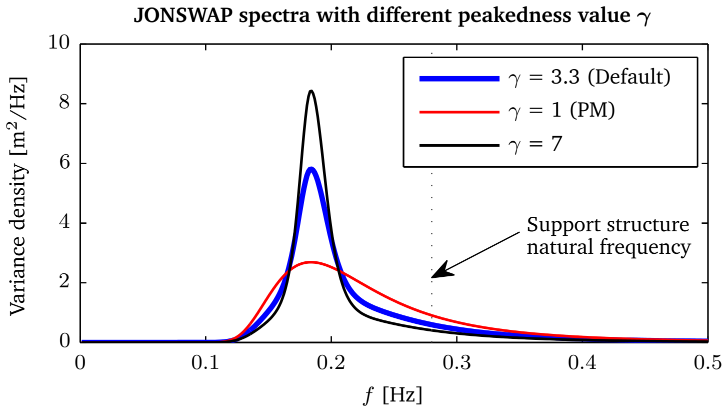

Figure 5.1: The JONSWAP wave spectra that are used in the sensitivity study. Examples are shown for a sea state with $H_S = 2.35$ m and $T_P = 5.44$ s.

The third group of simulations consists of two case studies on deterministic waves. As described in more detail in Appendix B, it was found that the foundation designer responsible for the certified wave loads used in the verification took the acceleration terms with a negative sign. The negative acceleration may not influence the magnitude of the maximum hydrodynamic load compared to a correctly modeled wave, but the different phasing might have an influence on the dynamic response behavior and loads. This is investigated for one wave seed of DLC 6.1, by a comparison between BHawC results from two wave load files. These wave load files are created from the same stochastic wave record, with the only difference that below the inserted deterministic wave the sign of the acceleration terms is exactly opposed. This way, it is possible to purely isolate the difference in response due to a different sign in the fluid acceleration.

Furthermore, discontinuities in the distributed wave load were observed frequently at the insertion points of the deterministic waves, as shown in Appendix B. Two wave load files with a significant discontinuity were therefore chosen, and modified such that the distributed load is smooth in time around the insertion point. The aim of the comparison is then to establish whether the discontinuity leads to transients in the response that may increase the maximum load in any component of the wind turbine.

5.3 Results of dynamic response simulations

This section presents the results of the dynamic response simulations with the hydrodynamic loads due to 1st-order linear and 2nd-order nonlinear waves as input, respectively. For the comparison, the equivalent fatigue loads due to the fore-aft and side-side bending moment, M_x and M_y respectively, are considered over the entire length of the support structure. To simplify the comparison of foundation and tower fatigue, a constant Wöhler slope of $m = 5$ is assumed. Also the sensitivity study is discussed.

5.3.1 Comparison of linear and nonlinear waves

The comparison of the dynamic response simulation results from cases A1 and A2, due to linear and nonlinear waves respectively, is shown in Figure 5.2. In this figure, the difference in equivalent fatigue load is shown, where the difference is normalized by the 1st-order simulation result at each structural node. It can be observed that the 2nd-order waves result in higher fatigue damage across the entire length of the support structure. The equivalent fatigue load increases most near MSL, and it can be seen that the damage increase due to side-side bending is significantly higher than due to fore-aft motion.

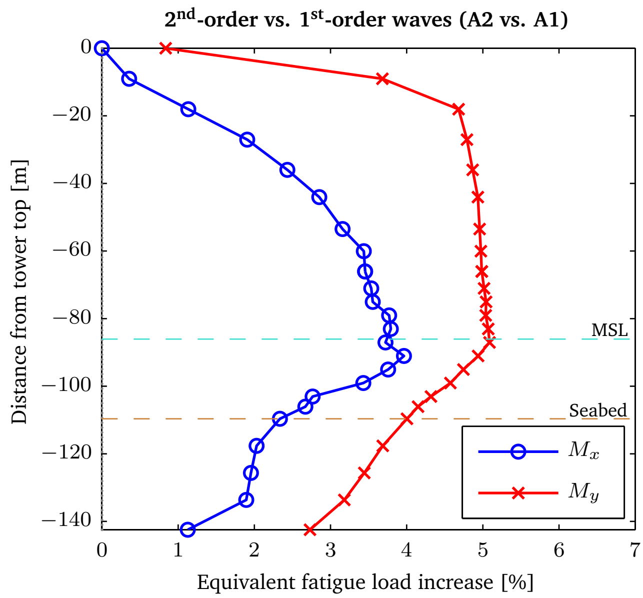

Figure 5.2: Influence of 2nd-order waves on equivalent fatigue loads. Difference is normalized by the values due to 1st-order waves on each structural node.

Since multiple load cases are simulated, the accumulation of fatigue damage can be further specified for each operation mode of the wind turbine. In Figure 5.3, a comparison of the fatigue accumulation by 1st- and 2nd-order waves is shown for both M_x and M_y at two vertical coordinates. The pie charts shown in this figure, represent the relative fatigue damage contribution of various operation modes of the wind turbine.

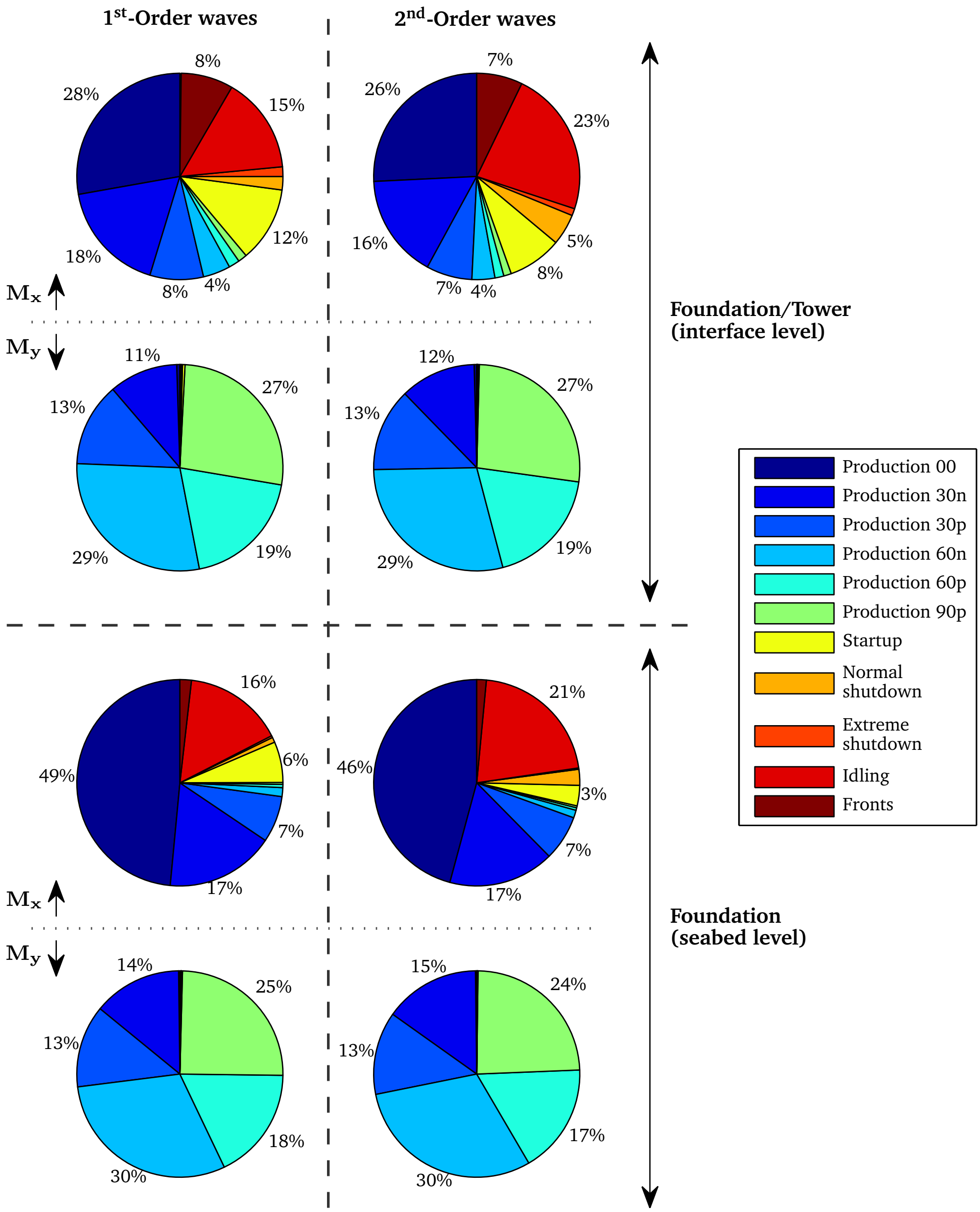

Figure 5.3: Relative contribution of several operation modes of the wind turbine on the fatigue damage caused by fore-aft (M_x) and side-side (M_y) bending. Results are shown for both wave models, at two positions in the support structure.

For the production, a number is shown to indicate the misalignment angle between the wind and wave propagation direction. The affixes (p) and (n) indicate whether the misalignment is positive or negative. The idling mode represents all load cases in which the turbine is not producing electricity. The fronts contribution is due to an additional load case, that is included by Siemens to account for weather fronts.

It can be observed that both at seabed and foundation/tower interface level, using 2nd-order waves yields a higher relative contribution of the idling mode to the fatigue damage accumulated due to fore-aft bending. For side-side bending, hardly any difference can be observed. Furthermore, it can be concluded at seabed level fatigue damage is dominated by the power production mode, while at the interface turbine startup and shutdown have a more pronounced role.

5.3.2 Sensitivity study

The primary purpose of the sensitivity study is to identify the effect of changing assumptions in the wave simulation input on the influence of 2nd-order wave modeling. Since the 2nd-order wave simulations are compared with 1st-order results using the same input assumptions, an additional comparison between several 1st-order simulations is possible. Therefore, in both study cases, the 1st-order results will also be compared to the reference simulations with the 1st-order waves from A1.

Peakedness of the JONSWAP wave spectrum

First, the simulations with 1st-order waves using different values for the JONSWAP peakedness parameters, B1 and B3, will be compared to the reference simulations, A1. In Figure 5.4, the difference in equivalent fatigue loads are shown for a value of $\gamma = 1$ (a) and $\gamma = 7$ (b). Again, the difference is normalized by the 1st-order simulation result from A1 at each structural node.

It is illustrated by this comparison that the shape of the input wave spectrum has a tremendous impact on the fatigue damage that is accumulated. Figure 5.4(a) shows that when the peakedness parameter is chosen such that the shape of the Pierson-Moskowitz spectrum is obtained ($\gamma = 1$), over the entire length of the support structure the equivalent fatigue load increases. A young sea state on the other hand results in lower fatigue damage, as can be seen in Figure 5.4(b). Similar to the comparison between 1st- and 2nd-order waves in Section 5.3.1, the side-side bending moment gives rise to the *highest relative change* in equivalent fatigue load in both cases. When the absolute values of equivalent fatigue loads due to M_x and M_y are inspected, it appears that still the fore-aft bending moment yields the *highest amount* of damage. The latter is consistent with the observations made earlier in Figure 4.10 in Chapter 4.

The impact of the wave spectrum on the additional fatigue damage caused by using 2nd-order waves (B2 and B4) instead of 1st-order waves (B1 and B3) is much smaller, as is shown in Figure 5.5. An interesting observation is that in

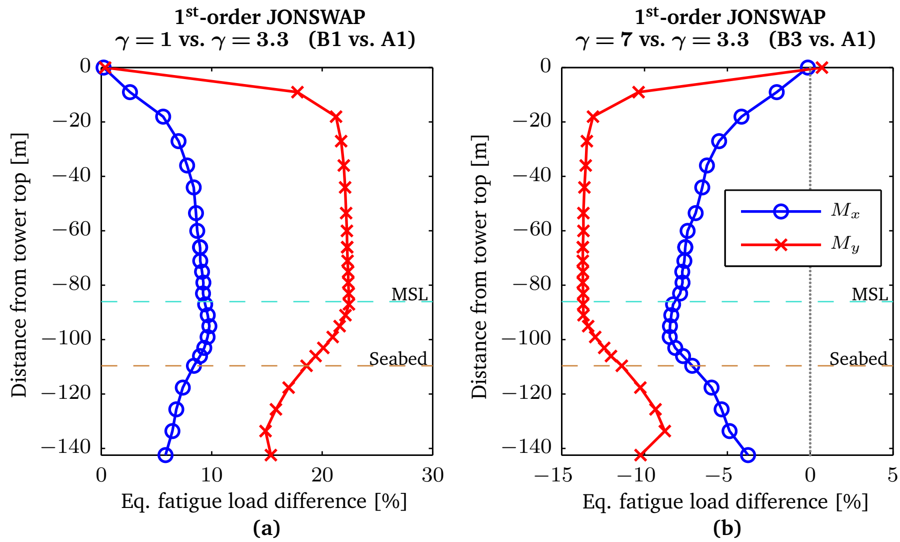

Figure 5.4: Comparison of equivalent fatigue loads due to 1st-order waves from a different input spectrum shape, with the default 1st-order waves where $\gamma = 3.3$ (A1). Difference is normalized by the values due to these reference 1st-order waves on each structural node.

both cases the fatigue damage due to fore-aft motion is affected the most by the nonlinearity of the waves. This contradicts the results from the standard spectrum discussed in Section 5.3.1, where the side-side moment caused the largest increase in equivalent fatigue loads. Both figures do show that the dependency of the equivalent fatigue due to M_x and M_y on the distance from tower top is similar to what is observed in the comparison with the default wave spectrum (Figure 5.2).

Modified current direction and Doppler shift

When the current direction is alternated rather than always co-flowing and a Doppler shift is applied, the effect on equivalent fatigue loads due to 1st-order waves is minimal, as is shown in Figure 5.6(a). The largest relative change in fatigue damage is found below the water level and is most pronounced in side-side bending.

In Figure 5.6(b), the comparison between 1st- and 2nd-order waves is shown for the simulations with the modified current and Doppler shift. It is observed that the increase in equivalent fatigue loads shows very similar values and variation with height as the previously discussed cases. Again, as was also seen in the sensitivity study on the change in wave spectrum shape, the fore-aft bending moment leads to the highest relative increase in fatigue damage.

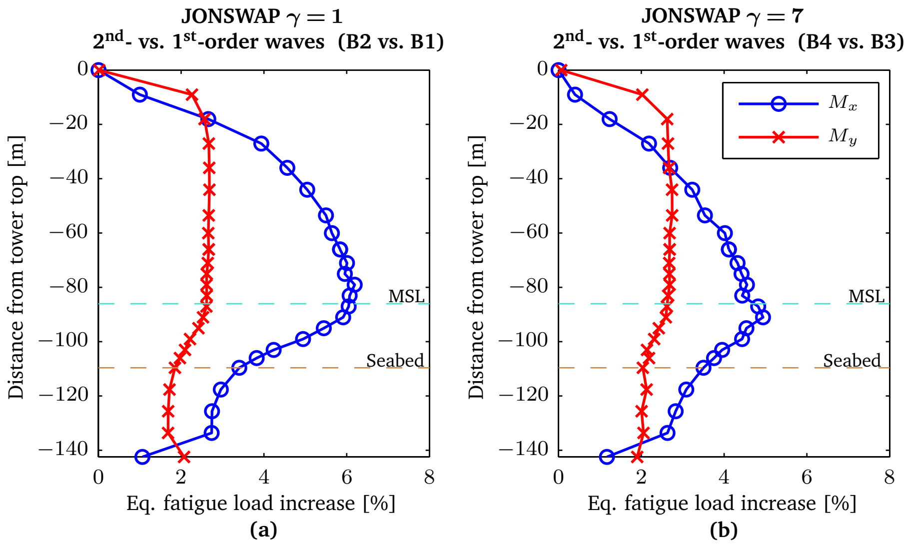

Figure 5.5: Influence of a different input spectrum on the increase of fatigue damage due to 2^{nd}-order waves (B2 and B4). Difference is normalized by the values due to 1^{st}-order waves from the same spectrum (B1 and B3).

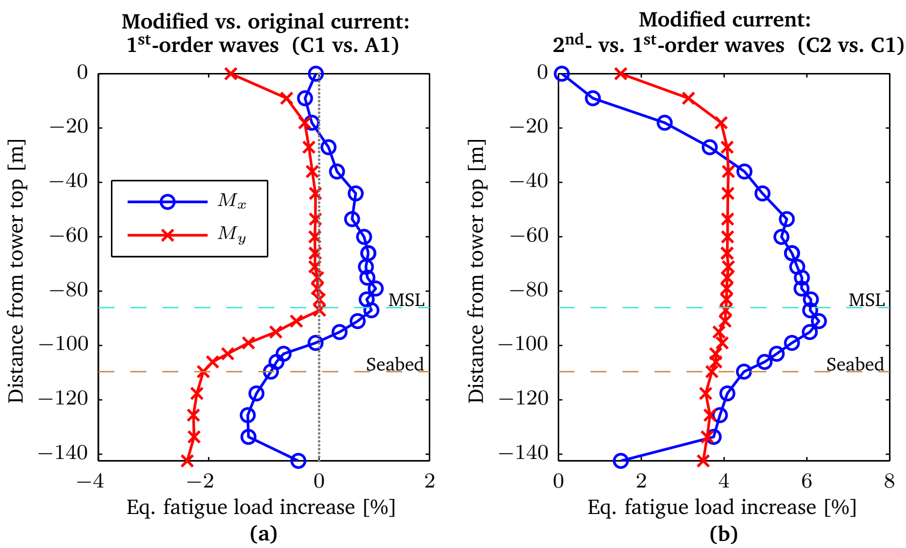

Figure 5.6: Influence of different assumptions in the current modeling, shown for 1^{st}-order waves (a) and 2^{nd}-order waves (b). Normalized by the values from 1^{st}-order simulations A1 and C1, respectively.

5.3.3 Case studies on deterministic waves

In this section, the case studies that were performed to investigate the impact of the quality of deterministic wave modeling on the dynamic response are discussed. The influence of discontinuities at the insertion point and of acceleration terms with a different sign is shown by both time- and frequency-domain graphs of bending moments in the support structure and the blades.

Discontinuity at insertion point

To investigate the influence of a wave load discontinuity at the insertion point of a deterministic wave, two wave seeds from the third-party foundation designer are taken. The first wave seed is taken from DLC 16, since this particular seed contains the relatively largest jump in the hydrodynamic force. Since this wave seed is in a power production load case, a second wave seed was selected from DLC 6.1, to observe the effect on an idling turbine. The modified wave load files have been smoothed, such that the distributed force is continuous in time. Both the original and modified wave load files are then used as input for the BHawC simulations.

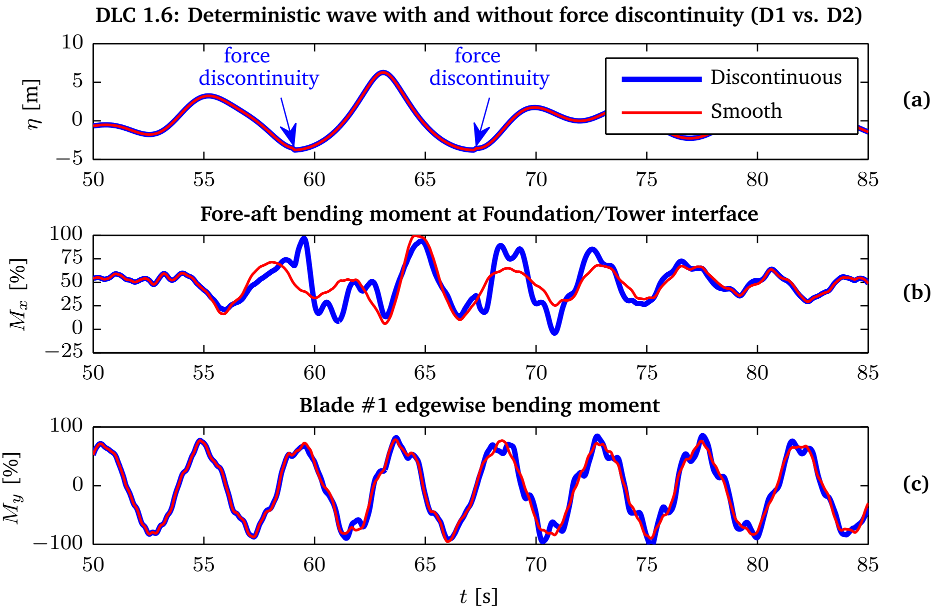

Figure 5.7: Effect of a discontinuity in the hydrodynamic force at the deterministic wave insertion point on the dynamic response. Bending moments are normalized by the absolute value of the maximum moment.

In Figure 5.7, the surface elevation (a) and fore-aft bending moment at foundation/tower interface level (b) are shown for the DLC 1.6 wave seed. Also the

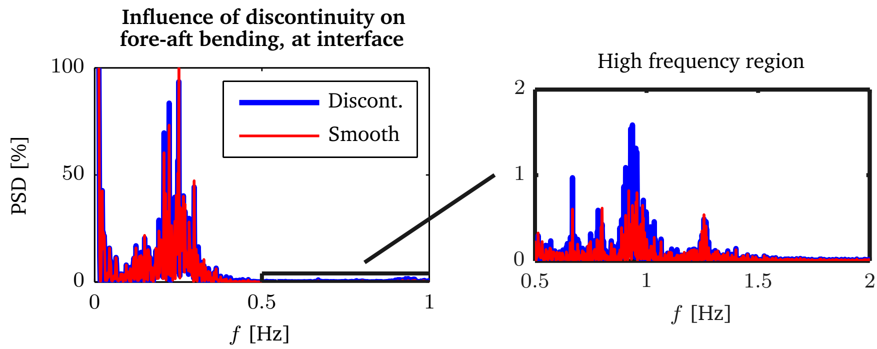

Figure 5.8: PSD of the fore-aft bending moment shown in Figure 5.7(b). Normalized by the value at the peak near 0.3 Hz.

edgewise bending moment of the first rotor blade is shown in Figure 5.7(c). It is observed that the jump, which occurs at the insertion points in the deterministic wave troughs, introduces a quite severe high frequency transient in the fore-aft bending moment. This high frequency oscillation in the response is also detected in the PSD of this bending moment, shown in Figure 5.8.

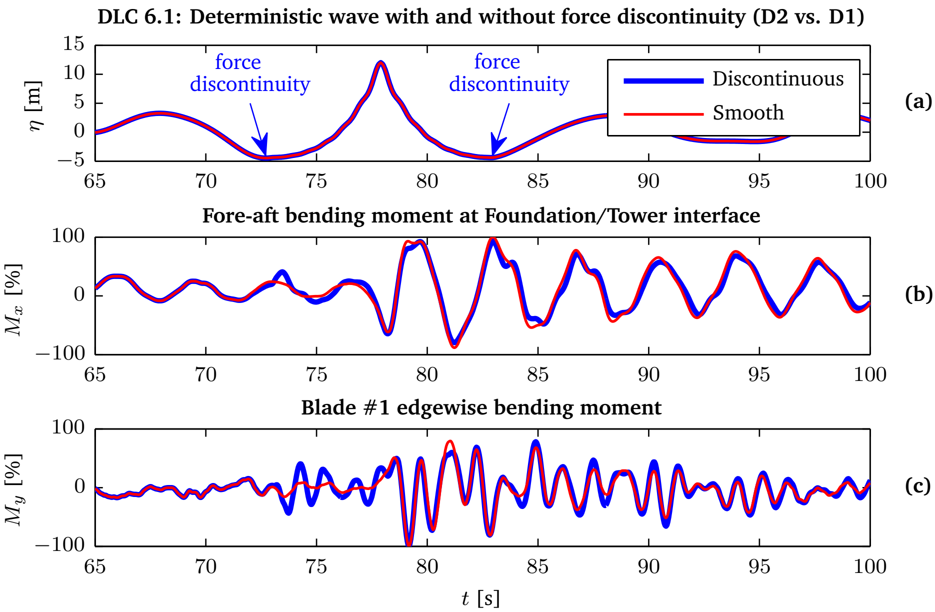

Figure 5.9: Effect of a discontinuity in the hydrodynamic force at the deterministic wave insertion point on the dynamic response. Bending moments are normalized by the absolute value of the maximum moment.

Although the maximum fore-aft bending moment due to the original wave only differs a few percent from the smoothed wave, it is disturbing that the maximum is achieved just after the insertion point, rather than during the passage of the wave crest. In the blade edgewise bending moment, the high-frequency oscillation is observed as well, albeit in smaller magnitude.

The second wave seed from DLC 6.1 contains a much smaller discontinuity. Hence, the effect on the fore-aft bending moment is significantly less severe, as can be observed from Figure 5.9. The influence on the edgewise bending moment of the first blade however, is much more pronounced. Since the magnitude of the bending moment in the blade in DLC 6.1 is comparable to the values that occur in power production, the additional oscillations that are excited by the jump are significant.

Negative acceleration below deterministic waves

The influence of using a deterministic wave with an incorrect fluid acceleration sign is illustrated with a wave seed from DLC 6.1. Two wave load files are used in the comparison, where the differentiation is made in the sign of the acceleration terms below the deterministic wave. In order to have identical dynamic response characteristics upon the arrival of the determinstic wave, the stochastic wave record was simulated with the correct sign.

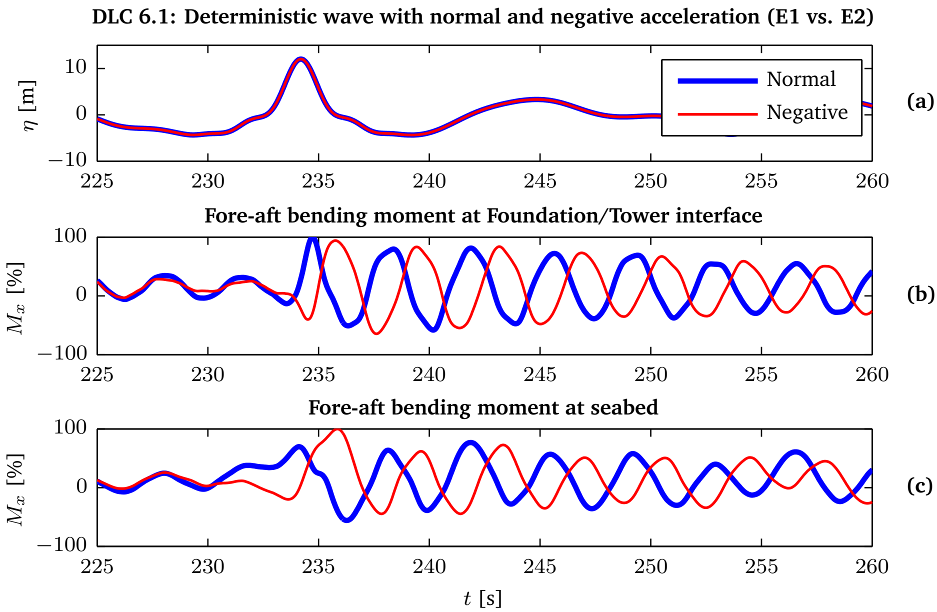

Figure 5.10: Effect of negative fluid acceleration below a deterministic wave on the dynamic response. Bending moments are normalized by the maximum moment.

In Figure 5.10, the surface elevation (a) and the fore-aft bending moment at two levels (b,c) are shown. Clearly, the phase shift due to the changed sign of the acceleration can be observed. Although the maximum fore-aft bending moment purely due to wave loading is equal for both wave load files, the maximum response load shows a striking difference of 23% at seabed level. Another interesting observation can be made in a frequency-domain representation, of the fore-aft bending moment at interface level, depicted in Figure 5.11. A zoom-in on the natural frequency of the support structure reveils that the two wave simulations result in a slightly different peak frequency of the power spectrum.

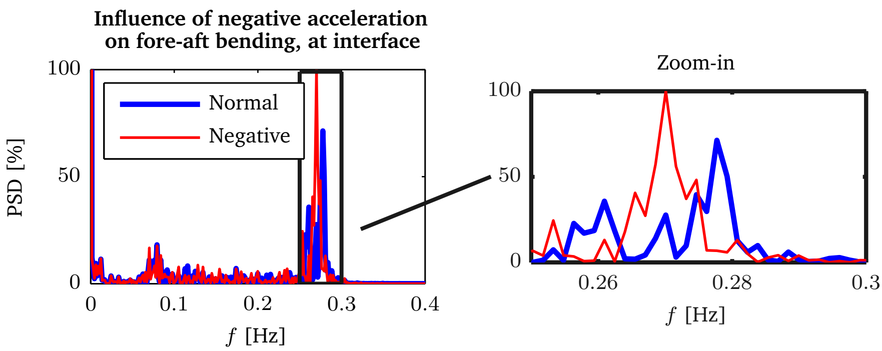

Figure 5.11: PSD of the fore-aft bending moment at interface level shown in Figure 5.10(b). Normalized by the value at the peak near 0.3 Hz.

5.4 Analysis of simulation results

In the previous section, the results of the various simulation cases listed in Table 5.1 were discussed. Based on the observations that were made, an analysis of the results is presented in this section.

5.4.1 Influence of nonlinear irregular waves on fatigue

It was shown in the comparisons between the results due to linear and nonlinear waves that the 2^{nd}-order wave model results in higher equivalent fatigue loads. Side-side bending was found to cause a higher relative increase in fatigue damage than fore-aft bending. A possible explanation for this observation is the reduced effectivity of aerodynamic damping of the rotor when wave propagation is misaligned with the wind direction. This reduction of response attenuation results in a larger amount of load cycles of a higher magnitude, which in turn causes a higher fatigue damage. Hence, an increase in wave loading has a more direct effect on the equivalent fatigue load if aerodynamic damping is small.

From the relative contribution from each operation mode, in the fore-aft bending direction the most notable observation was that significantly more fatigue damage was accumulated during the idling of the turbine. This can be explained by two considerations. First, when the turbine is in idling mode, aerodynamic damping from the rotor is absent. Second, since in some cases the reason of the idling is the occurrence of strong winds above the cut-out wind speed, the significant wave height is high. In a high sea, the water depth is relatively small, which causes nonlinear effects to be more pronounced. Hence, the combination of relatively strong nonlinear effects and the absence of aerodynamic damping is likely to cause a significant increase in fatigue damage.

5.4.2 Sensitivity to wave modeling assumptions

The sensitivity study on the peakedness of the JONSWAP spectrum showed that a fully developed sea state (PM spectrum) yields to more than 20 % increase in fatigue loads. This can be explained by distribution of wave energy over the frequencies. Whereas the JONSWAP spectrum has a very defined peak frequency, in the PM spectrum the wave energy is more spread out over the rest of the frequencies. As can be observed in Figure 5.1, this results in a higher amount of energy near the natural frequency of the support structure. It was demonstrated in Chapter 2 that this can lead to a poorly damped response, which leads to an increase in fatigue damage, as is observed in the simulation results. On the contrary, a high peakedness results in lower fatigue damage due to the reduced amount of energy near the natural frequency.

The predicted effect of the spectrum on the influence of nonlinearity was not observed, since the comparisons between 1^{st}- and 2^{nd}-order waves did not differ significantly in magnitude from the comparison with the standard spectrum. A remarkable observation however, was that instead of the side-side bending moment, the fore-aft bending appeared to result in the highest relative increase in equivalent fatigue loads. This was also observed in the linear versus nonlinear waves comparison with the different assumptions for the current. An explanation for this observation was not found.

Assuming an alternating current direction and a Doppler shift did not result in significantly different results, neither between 1^{st}-order waves or on the influence of 2^{nd}-order waves. Since two assumptions were changed for this case study, it is not possible to isolate the influence of either the Doppler shift or alternating the direction of the current. Therefore, it may as well be the case that the effect of one assumption compensates the influence of the other.

Besides this, it can be deduced from the results that despite the introduced modeling errors in the Doppler-shifted frequency domain method with 2^{nd}-order waves (see Section 4.2.2), reliable results are obtained. Thus, for the given sea environment, the modeling errors appear to be of an acceptable level.

5.4.3 Impact of low-quality deterministic wave modeling

It was shown that a discontinuity at the insertion point of a deterministic wave has a severe effect on the fore-aft bending moment in the support structure. In the most severe case, the maximum fore-aft bending moment was achieved just after the discontinuity, rather than after the passage of the wave crest. Since the bending moment due to the stochastic wave record was already high when the jump in hydrodynamic load occurred, the transient response due to the jump was severe enough that a maximum was achieved.

Besides that, the edgewise bending moment of the blades appeared to be influenced significantly by the discontinuity. In power production (DLC 1.6), the effect is noticeable but limited, since the aerodynamic forces on the blade are able to suppress the response quite effectively. In idling (DLC 6.1) however, the blade excitations due to the jump are more severe due to the absence of aerodynamic damping.

From the simulations with a negative acceleration below deterministic waves, a significant difference was found between the maximum fore-aft bending moments at seabed level. On the interface level, this difference however appeared to be far less pronounced. The reason for this remarkable observation was not found.

Furthermore, a difference in the peak frequency of the fore-aft bending moment PSD was found. As can be observed in the time series of the bending moment, the transients caused by the deterministic wave take considerable time to damp out. Since the stochastic record is simulated with the correct accelerations, the phase shift introduced by the deterministic wave is eventually corrected again, as wave action of the stochastic record takes over the dominant response. This explains the difference in spectral power peak frequency.

6 Conclusion and Recommendations

6.1 Introduction

The primary goal of this thesis is to quantify the influence of using a nonlinear irregular wave model on the predicted fatigue damage of an offshore wind turbine. The prediction of how much fatigue damage is accumulated, is done by a large amount of dynamic response simulations of an entire set of design load cases, which should represent the entire lifetime of the wind turbine. The simulations are carried out in the time-domain using the aero-servo-elastic wind turbine code BHawC.

In order to carry out a comparison with the traditional linear wave model with Wheeler stretching, both the linear 1^{st}-order and a 2^{nd}-order nonlinear irregular wave model were implemented. These provide the wave kinematics, after which the Morison equation is used to calculate the hydrodynamic load on the support structure. The resulting output from this hydrodynamic load calculation program is then used as input for the dynamic response simulations in BHawC. In the previous chapters, the theory behind the wave models and the details of the implementation were given. The output of the hydrodynamic load program was verified using an existing wind farm project in the German Bight, of which the input parameters were fully documented.

In Chapter 5, the comparison between simulation results due to linear and nonlinear waves was described and analyzed. Additionally, a sensitivity study was performed. This comprises a number of full sets of simulations, where the input settings for the wave simulations were changed. Subject to investigation were the effect of changes in the shape of the JONSWAP wave spectrum and the assumptions used to model the current. Besides that, two additional case studies were performed on the quality of deterministic wave modeling. This was done to investigate the impact of modeling errors, which were observed in third-party wave simulations, on the dynamic response.

In this chapter, the final conclusions are drawn based on the observations and analyses that were made in the previous chapters. Additionally, recommendations for future work are given. Finally, the work is reflected upon in a section that contains the lessons learned during this project.

6.2 Conclusion

This section presents the conclusions from the analysis of the linear versus nonlinear waves comparison, sensitivity study and case study performed in Chapter 5. Also, the Doppler-shifted frequency-domain method that was devised to be able to account for a Doppler shift due to a steady current is reflected upon. Finally, the impact of using nonlinear irregular waves on fatigue design is assessed.

6.2.1 Influence of nonlinear irregular waves on fatigue damage

The comparison between the dynamic response simulations run with linear and 2nd-order irregular waves reveiled that, as expected, the nonlinear waves yield higher equivalent fatigue loads. The increased hydrodynamic load due to the nonlinearity of the waves has the largest impact on the support structure, near the mean sea level. It was found that the effect on other components than the tower and foundation, for example the blades and nacelle, is insignificant.

Regardless of which wave model is used to prepare the hydrodynamic loads, the dynamic response loads due to fore-aft bending of the support structure are responsible for the largest portion of the fatigue damage accumulation. The highest equivalent fatigue load is achieved just below the seabed, and decreases gradually towards the tower top. Using the 2nd-order wave model than traditional linear wave theory, the response loads due to side-side bending result in the largest *relative* increase in equivalent fatigue loads. The highest increase was found to be 5% from the original load due to linear waves. In fore-aft bending direction, the maximum relative increase was found to be slightly lower with 4%. The higher increase in fatigue damage in the side-side bending was contributed to the absence of aerodynamic damping of response motion by the rotor, when wave action is misaligned with the wind direction. Due to this smaller response damping, a higher wave load thus has a more pronounced impact on side-side than on fore-aft bending.

The contribution of several turbine operation modes to the accumulation of fatigue damage was also investigated. The most significant difference between linear and nonlinear waves was found in the relative amount of fatigue damage due to fore-aft bending when the turbine is idling. Measured at the foundation/tower-interface, 23% of the fatigue damage due to fore-aft bending was accumulated during idling using nonlinear waves, whereas with linear waves this proved to be only 15%. Again, since the rotor is inactive in the idling mode, the lack of aerodynamic damping was brought up as one of the reasons for this significant increase. Besides that, in some of the scenarios when the turbine is idling, wind speeds are high and hence the sea is in an agitated state. This means that the wave height is large with respect to the water depth, which results in a high degree of nonlinearity. Both factors explain the increase of fatigue damage in the idling mode. Contrary to the fore-aft bending, no significant difference between wave models was found in the contribution of operation modes to side-side fatigue damage accumulation.

6.2.2 Sensitivity to wave modeling assumptions

A sensitivity study was carried out to test the sensitivity of fatigue damage estimation to the assumptions used for the wave model. First, the wave spectrum used to obtain the amplitude of each frequency component in the wave record was changed. Since a JONSWAP spectrum was used with a value of the peakedness-parameter of $\gamma = 3.3$, this value was changed to $\gamma = 1$ and $\gamma = 7$ to investigate the effect on both dynamic response simulations with linear and 2$^{\mathrm{nd}}$-order waves. The assumed values represent a fully developed and very young sea state, respectively.

It was shown that the input spectrum has a very significant influence on the equivalent fatigue loads. Using linear waves in the dynamic response simulation, the fully developed sea state assumption led to approximately 10% higher equivalent fatigue loads due to fore-aft bending. The fatigue damage due to side-side bending increased up to 22%, but since the absolute values of the equivalent loads in this direction is lower, this is considered less important. The increase in fatigue damage was explained by the higher amount of energy in the tail of the wave spectrum, in which the natural frequency of the support structure is situated. The young sea state with $\gamma = 7$ on the other hand, led to a equivalent fatigue load reduction of up to 8% in fore-aft bending. In side-side bending, this reduction amounts to up to 13%.

For the two different spectra, the influence of 2$^{\mathrm{nd}}$-order waves with respect to linear waves remained of comparable magnitude as observed in the comparison with the default spectrum. It was found however, that the relative increase in fore-aft bending fatigue damage is slightly higher than with the default spectrum. Also, the side-side fatigue damage was limited to an increase of approximately 2% in both cases, whereas this was 5% in the default scenario. An explanation for these observations was not found.

Besides the spectrum, the influence of changing the assumptions with respect to a steady current was investigated. Rather than assuming that the current is co-flowing with the waves, the direction was alternated to simulate a tide. Furthermore, the Doppler shift was taken into account rather than ignored. Both assumptions only led to a small change ($< 2\%$) in the fatigue damage with the traditional linear wave theory. It was concluded that by changing two assumptions at the same time, the effect of the individual settings is hard to isolate.

The 2^{nd}-order Doppler shifted waves showed a very similar equivalent fatigue load increase as the study cases with the different wave spectra. This suggests that the 2^{nd}-order wave model with the Doppler-shifted frequency-domain approach, devised in Chapter 3, yields very acceptable results given the sea and current environment of the test farm.

6.2.3 Impact of poor deterministic wave modeling

Two case studies were conducted to investigate the effect of modeling inaccuracies on the dynamic response loads. First, discontinuities at the insertion point of a deterministic wave were inspected. When a deterministic wave is glued into a stochastic record, the distributed hydrodynamic load should be continuous at the insertion point to avoid undesired response behavior. With two third-party examples containing a jump, by a comparison with a smoothed insertion it was shown that a jump in the wave load can lead to severe transients in the dynamic response of the offshore wind turbine. These transients caused significant differences in the bending moments in the support structure and rotor blades.

The worst case, which occurred in a power production load case (DLC 1.6), showed that the maximum fore-aft bending moment was achieved after the discontinuity rather than after the wave crest. In an idling case with an extreme sea state, also the blades were excited quite severely, leading to significant edgewise bending moments just after the discontinuity. Even though the discontinuity was by far not as severe as the worst case, the effect was very visible in the blade response loads. This confirms that the insertion of a deterministic wave requires careful attention.

A second case study was performed with a negative acceleration below the deterministic wave. This was done to show that this unphysical implementation of acceleration terms, which was done by a third-party foundation designer, has a noticeable impact on dynamic response behavior. An idling case with an extreme sea state (DLC 6.1) showed a completely different behavior of the fore-aft bending moment at seabed level, compared to the smooth version of the same wave record. This resulted in a 23% lower maximum fore-aft bending moment at seabed level when the fluid acceleration is physically correct rather than negative. On the foundation/tower-interface this difference was smaller with 6%. This case study shows that this incorrect way of modeling has a severe impact on the dynamic response loads.

For the wind farm used for simulations in this thesis, the load case investigated in the above case appeared to be design driving. Considering the fact that this wind farm was designed using wave loads with a negative acceleration and with discontinuities at the insertion point, it is very likely that significant errors have been made in the design.

6.2.4 Effect of nonlinear irregular waves on design

As mentioned above, ultimate loads in extreme wave conditions turned out to be design driving for the support structure of the wind farm used in this research. Hence, the increase in fatigue damage due to using nonlinear irregular waves instead of linear waves would not change the dimensions of the support structure in this case. This may be different in another environment, where the support structure design is fatigue driven rather than ultimate load driven.

For the given water depth of 25 m. and the given sea environment and support structure, it may be concluded that the maximum equivalent fatigue damage due to fore-aft bending increases between 4 and 6%. This maximum increase is found near the mean sea level. It has to be emphasized that this figure depends on the degree of nonlinearity of the waves, which in turn is related to the relative water depth compared to the wave height. This, of course, is very site specific.

The calculation time of a single wave record of 10 minutes with 500 wave frequencies and a vertical coordinate on every meter, turned out to be approximately 5 seconds on an ordinary laptop. Using the frequency-domain approach described in this report, the argument that the required calculations would be too demanding, is no longer valid. Therefore, if this method is implemented carefully, it is a good candidate to replace the traditional linear wave model in the industry standard.

6.3 Recommendations for future work

Based on the conclusions and the experience that was gained by developing and testing the hydrodynamic load model, recommendations for future work can be given. These recommendations concern both work on the developed tool and possible follow-up research projects. Five recommendations are listed below.

- **Reconsideration of safety factor on fatigue loads**
  As described in the conclusion, nonlinear irregular waves results in a roughly 5% higher fatigue damage. In the current standard of modeling wave kinematics, using linear wave theory with Wheeler stretching, this difference is accounted for with a safety factor on the dynamic response loads. Since employing a more accurate model should always be preferred above using an empirical safety factor, the value of the latter is subject to discussion to avoid overdimensioning of the support structure. Hence, if one intends to use the 2$^{\text{nd}}$-order irregular wave model described in this thesis, the safety factor on loads should be reconsidered carefully. It should be mentioned that since the nonlinearity of the waves strongly depends on the relative water depth, each site has its unique wave characteristics and therefore requires specific consideration.

- **Correcting the added power by downscaling the input wave spectrum**
  As mentioned in Chapter 4, by using the 2$^{\text{nd}}$-order wave model power is

added to the wave energy spectrum. This results in a slight increase of the significant wave height of the output wave record. For this research this increase was assumed to be small enough to be ignored. A more realistic approach would be to correct the input wave spectrum for the added power due to the 2nd-order contributions. However, since downscaling the input spectrum in turn affects the magnitude of the 2nd-order components, an iterative procedure may be required.

- **Using more site-specific wave spectra and directional irregular waves**
  The sensitivity study that was performed, showed that the choice of which wave spectrum is used has a significant impact on the fatigue damage that is accumulated in the dynamic response simulations. Since wave conditions are very site specific, the common assumption to just use a JONSWAP spectrum with a peakedness-parameter of $\gamma = 3.3$ almost seems ill-considered. Especially if a swell, which is less dependent of the local wind conditions, occurs frequently, the JONSWAP spectrum might be inappropriate. Therefore, a double-peaked Torsethaugen spectrum should perhaps be considered instead. Given the impact of the chosen wave spectrum on the modeled fatigue damage, the spectrum should thus be chosen with care. Furthermore, evidence exists that including directional spreading in wave modeling results in a significant fatigue damage reduction [78]. Therefore, investigating the influence of using directional waves on fatigue damage would be a logical next step in irregular wave modeling for offshore wind turbines.

- **Assessment of sensitivity on assumptions in modeling currents**
  A sensitivity study was performed on the impact of using different assumptions in the modeling of a steady current. Due to a shortage of time, this case study was limited to one change of parameters, which did not result in a useful conclusion. Therefore, a sensitivity study is suggested to isolate the effect of using a Doppler shift, and the influence of the assumed current direction. If the Doppler shift does have a significant impact, the devised Doppler-shifted frequency-domain approach may need to be improved when used with 2nd-order waves, or if possible a different approach should be considered. A research on a case in which both the current and nonlinear effects are strong would be useful to test the accuracy of the devised method.

- **Verification of the Fourier method implemented for deterministic waves**
  In Appendix B, the implementation of the Fourier approximation model for nonlinear regular waves is discussed. This method, which is used to model deterministic extreme waves, was found to be quite sensitive to the assumptions that were made with respect to the current. Within the time available for this project, it was not possible to verify whether the assumptions that have been used are fully correct. Therefore, additional work is required to

make sure the Fourier approximation model yields physically sound results.

- **Feasibility of more advanced modeling of near-breaking extreme waves** Besides the implementation issues, some of the extreme waves that needed to be modeled are on the verge or even beyond the theoretical breaking limit. In those cases, it was hard to find a combination of input settings that resulted in a converging solution. This definitely illustrates the limitation of the perturbation approach that is used in the Fourier method and similar models, which is and has been the standard for many years. In order to be able to model extreme waves close to the breaking limit properly, for example a full-potential flow method could be an option. Hence, the feasibility of implementing such a model of higher fidelity for engineering purposes should be investigated.

6.4 Lessons learned during this project

Besides the conclusions that are drawn and the recommendations that are given for future research, finalizing the project has given insight in the lessons that were learned. The three most important are listed below.

- **Implementation challenges should not be solved at all cost** In Chapter 3, a method was devised to be able to account for a Doppler shift due to a current in the frequency domain. This proved to be challenging, due to which a considerable amount of time was spent to analyze and solve the problem at hand. In retrospect, it would have been wiser to first analyze the impact of changing the assumptions in current modeling on the fatigue damage, using the straight-forward time-domain formulation of linear wave theory. This way, the conclusion may have been drawn that the time spent overcoming the challenge of implementing the Doppler shift in the frequency domain would not justify the gain in modeling accuracy.

- **Define the framework of the simulations as early as possible** Quite some time passed in this project before the simulation project was defined. Together with the requirement by Siemens to deliver a complete hydrodynamic load simulation toolbox, this led to a pursuit of flexibility in realizing the wave load calculation program. Had the simulation project been chosen earlier, the more defined scenario would have lowered the amount of options that the program should be able to handle. Besides that this results in less implementation work, the challenge mentioned in the previous point could have been avoided. On the contrary, the requirement of realizing a versatile model has resulted in a more structured approach to build the program.

- **Certification of hydrodynamic loads does not guarantee quality** As was discovered during the verification of the developed wave models against the results from a third-party foundation designer, the fact that the wave loads had been certified did not prevent errors in the results. Hence, certification is not sanctifying and wave loads that are provided by third-parties should always be inspected carefully on their physical correctness.

A
Linear wave theory derivations

In Chapter 2, the gouverning equations and boundary conditions of a free surface gravity wave were briefly stated. In this appendix, the derivation of those equations from the full Navier-Stokes equations, and the linearization of the non-linear surface boundary conditions will be shown in detail. Good understanding of these equations and the limitations imposed on its applicability by the assumptions made during the linearizations, are of fundamental importance.

A.1 Equations of motion

We will start with the basic equations of motion, assuming that the fluid is incompressible, such that the density is constant in time and space. These are the Navier-Stokes equations, which in Chapter 2 were stated in vector form (Eqs. 2.18 and 2.19), here they are written out in each direction.

continuity:

$$\frac{\partial u}{\partial x} + \frac{\partial v}{\partial y} + \frac{\partial w}{\partial z} = 0 \tag{A.1}$$

momentum:

$$\text{x-dir} \rightarrow \quad \frac{\partial u}{\partial t} + \frac{\partial (uu)}{\partial x} + \frac{\partial (uv)}{\partial y} + \frac{\partial (uw)}{\partial z} = -\frac{1}{\rho}\frac{\partial p}{\partial x} + \nu\left(\frac{\partial^2 u}{\partial x^2} + \frac{\partial^2 u}{\partial y^2} + \frac{\partial^2 u}{\partial z^2}\right) \tag{A.2}$$

$$\text{y-dir} \rightarrow \quad \frac{\partial v}{\partial t} + \frac{\partial (uv)}{\partial x} + \frac{\partial (vv)}{\partial y} + \frac{\partial (vw)}{\partial z} = -\frac{1}{\rho}\frac{\partial p}{\partial y} + \nu\left(\frac{\partial^2 v}{\partial x^2} + \frac{\partial^2 v}{\partial y^2} + \frac{\partial^2 v}{\partial z^2}\right) \tag{A.3}$$

$$\text{z-dir} \rightarrow \quad \frac{\partial w}{\partial t} + \frac{\partial (uw)}{\partial x} + \frac{\partial (vw)}{\partial y} + \frac{\partial (ww)}{\partial z} = -\frac{1}{\rho}\frac{\partial p}{\partial z} + \nu\left(\frac{\partial^2 w}{\partial x^2} + \frac{\partial^2 w}{\partial y^2} + \frac{\partial^2 w}{\partial z^2}\right) \tag{A.4}$$

Considering only the momentum equation in the x-direction, the chain rule can be applied on the terms on the left hand side (LHS) and neglecting the viscous terms on the right hand side (RHS) the Euler equation in x-direction is obtained:

$$\frac{\partial u}{\partial t} + u\left(\frac{\partial u}{\partial x} + \frac{\partial v}{\partial y} + \frac{\partial w}{\partial z}\right) + u\frac{\partial u}{\partial x} + v\frac{\partial u}{\partial y} + w\frac{\partial u}{\partial z} = -\frac{1}{\rho}\frac{\partial p}{\partial x} \tag{A.5}$$

$$\frac{\partial u}{\partial t} + u\frac{\partial u}{\partial x} + v\frac{\partial u}{\partial y} + w\frac{\partial u}{\partial z} = -\frac{1}{\rho}\frac{\partial p}{\partial x} \tag{A.6}$$

In Eq. A.5 the term in brackets can be omitted, as follows from the continuity equation, Eq. A.1. Assuming irrotational flow, the continuity equation can be expressed in terms of the velocity potential $\boldsymbol{u} = \nabla\Phi$:

$$\frac{\partial^2 \Phi}{\partial x^2} + \frac{\partial^2 \Phi}{\partial y^2} + \frac{\partial^2 \Phi}{\partial z^2} = 0 \tag{A.7}$$

Irrotational flow requires the curl of the flow to be zero, or: $\Omega = \nabla \times \boldsymbol{u} = 0$. This gives:

$$\Omega_x = \frac{\partial w}{\partial y} - \frac{\partial v}{\partial z} = 0 \quad \rightarrow \quad \frac{\partial v}{\partial z} = \frac{\partial w}{\partial y} \tag{A.8}$$

$$\Omega_y = \frac{\partial u}{\partial z} - \frac{\partial w}{\partial x} = 0 \quad \rightarrow \quad \frac{\partial u}{\partial z} = \frac{\partial w}{\partial x} \tag{A.9}$$

$$\Omega_z = \frac{\partial v}{\partial x} - \frac{\partial u}{\partial y} = 0 \quad \rightarrow \quad \frac{\partial u}{\partial y} = \frac{\partial v}{\partial x} \tag{A.10}$$

Substitution in the x-momentum equation, Eq. A.6 gives:

$$\frac{\partial u}{\partial t} + u\frac{\partial u}{\partial x} + v\frac{\partial v}{\partial x} + w\frac{\partial w}{\partial x} = -\frac{1}{\rho}\frac{\partial p}{\partial x} \tag{A.11}$$

The spatial derivatives on the LHS can be gathered in one term, and subsequently the velocity potential can be substituted:

$$\frac{\partial u}{\partial t} + \frac{\partial}{\partial x}\left(\frac{1}{2}u^2 + \frac{1}{2}v^2 + \frac{1}{2}w^2\right) = -\frac{1}{\rho}\frac{\partial p}{\partial x} \tag{A.12}$$

$$\frac{\partial}{\partial t}\left(\frac{\partial \Phi}{\partial x}\right) + \frac{\partial}{\partial x}\left\{\frac{1}{2}\left[\left(\frac{\partial \Phi}{\partial x}\right)^2 + \left(\frac{\partial \Phi}{\partial y}\right)^2 + \left(\frac{\partial \Phi}{\partial z}\right)^2\right]\right\} = -\frac{1}{\rho}\frac{\partial p}{\partial x} \tag{A.13}$$

Regrouping the spatial derivatives again:

$$\frac{\partial}{\partial x}\left\{\frac{\partial \Phi}{\partial t} + \frac{1}{2}\left[\left(\frac{\partial \Phi}{\partial x}\right)^2 + \left(\frac{\partial \Phi}{\partial y}\right)^2 + \left(\frac{\partial \Phi}{\partial z}\right)^2\right] + \frac{p}{\rho}\right\} + gz = 0 \tag{A.14}$$

where the gravity term gz has been added for completeness. As this term is not a function of x, the equation can be set equal to a function that depends solely on time. In its simplest form this function is zero, $f(t) = 0$, so we can put the equation in a more general vector form:

$$\frac{\partial \Phi}{\partial t} + \frac{1}{2}\left|\nabla \Phi\right|^2 + \frac{p}{\rho} + gz = 0 \tag{A.15}$$

This is the nonlinear Bernoulli equation for unsteady motion, derived with the assumption of irrotational, inviscid (potential) flow.

A.2 Boundary conditions

For an ocean wave, three boundary conditions need to be taken into account: the kinematic boundary conditions at the bottom and the free surface and a dynamic boundary condition at the surface.

- **Kinematic boundary condition at the sea bed**
  This boundary condition simply requires that the bottom is impermeable. To achieve this, the velocity component normal to the sea bed should be zero, which in case of a flat bottom is:

$$\boxed{w = \frac{\partial \Phi}{\partial z} = 0} \qquad \text{at } z = -d \tag{A.16}$$

- **Kinematic Free Surface Boundary Condition (KFSBC)**
  On the surface, fluid particles are assumed not to be able to leave the surface, so velocity components normal to the surface should be zero. In Figure A.1, this is illustrated with the displacement of a fluid particle riding the surface on the left and the evolution of the surface on the right. This yields the following kinematic relation for the 2D case shown in the illustration:

$$w\cos\alpha - u\sin\alpha = \frac{\partial \eta}{\partial t}\cos\alpha \qquad \text{at } z = \eta \tag{A.17}$$

Rewriting Eq. A.17 gives:

$$w = \frac{\partial \eta}{\partial t} + u \tan \alpha = \frac{\partial \eta}{\partial t} + u \frac{\partial \eta}{\partial x} \qquad \text{at } z = \eta \tag{A.18}$$

After substitution of the velocity potential the KFSBC reads:

$$\frac{\partial \Phi}{\partial z} = \frac{\partial \eta}{\partial t} + \frac{\partial \Phi}{\partial x}\frac{\partial \eta}{\partial x} \qquad \text{at } z = \eta \tag{A.19}$$

The last term in this expression contains a nonlinear term, as the velocity potential appears both on the LHS and the RHS. Assuming a small perturbation and wave steepness, such that $\alpha \to 0$, this nonlinear term can be neglected and the relation becomes linear:

$$\boxed{\frac{\partial \Phi}{\partial z} = \frac{\partial \eta}{\partial t}} \qquad \text{at } \mathbf{z} = \mathbf{0} \tag{A.20}$$

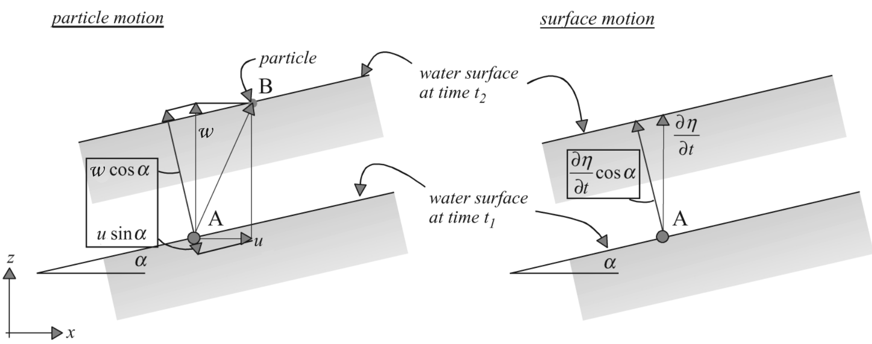

Figure A.1: Visualization of the KFSBC, with particle displacement on the left and surface displacement on the right [7].

- **Dynamic Free Surface Boundary Condition (DFSBC)**
  The DFSBC requires that the pressure at the surface is equal to the ambient pressure of the air on top of the wave. Taking the Bernoulli equation, Eq. A.15 and setting $p = 0$ at $z = \eta$ gives an expression for the DFSBC:

$$\frac{\partial \Phi}{\partial t} + \frac{1}{2}\left|\nabla \Phi\right|^2 + g\eta = 0 \qquad \text{at } z = \eta \tag{A.21}$$

As the quadratic term is nonlinear, removing the term will linearize the DFSBC, assuming again a small perturbation and small wave steepness. The DFSBC then reads:

$$\boxed{\frac{\partial \Phi}{\partial t} + g\eta = 0} \qquad \text{at } \mathbf{z} = \mathbf{0} \tag{A.22}$$

B

Deterministic extreme waves

In Section 2.2.5, several wave models were presented for regular waves. Although these models are not within the scope of this thesis project about nonlinear irregular waves, its insertion and use in stochastic records are discussed in this appendix nonetheless. The reason is that for a full load case simulation, deterministic waves shall be included. Besides that, during this research it was found that in practice the insertion of deterministic extreme waves is often of poor quality and sometimes the physical correctness of the wave itself is doubtful. This appendix therefore presents some observations on an example wave from a third party, delivered to Siemens to use as input in dynamic response simulations. Furthermore, an insertion method is proposed, which provides a robust way to smoothly glue a deterministic wave into a stochastic record.

B.1 Analysis of a low quality deterministic wave

To illustrate the problems that were observed in deterministic waves, an example of a deterministic wave inserted in a stochastic wave record is shown in Figure B.1. This example wave record has been supplied to Siemens by a third party foundation designer, as an input wave load file for the same project that was used for verification (Chapter 4). The figure shows two graphs; the surface elevation and the resultant shear force at seabed level acting in the propagation direction of the waves. The specific example shown here is a nonlinear regular wave of height $H = 16.4$ m and wave period $T = 9.8$ s, with a water depth below mean sea level of $d = 26.8$ m.

From Figure B.1 several observations can be made. First, a jump in the shear force can be seen on the transition points from stochastic to regular wave and vice versa, which take place at approximately 92.5 and 103 seconds respectively. Although the surface elevation is completely smooth, the force time series is not,

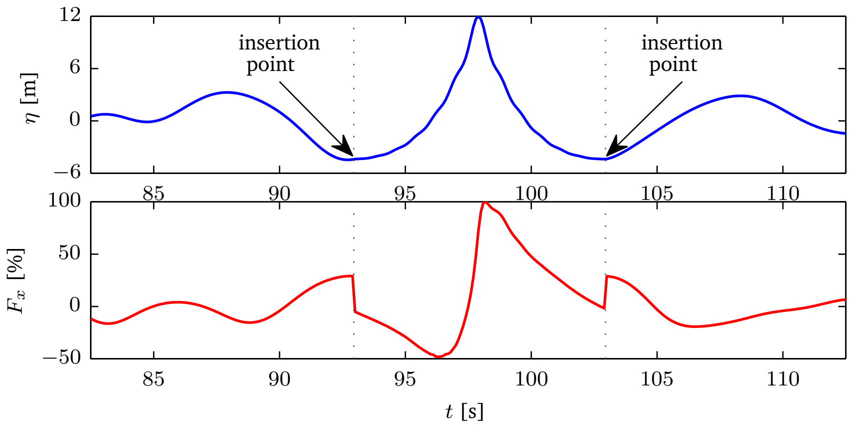

Figure B.1: An everyday example of a poorly inserted deterministic wave. While the surface elevation η (top) is smooth, the shear force at seabed level F_x (bottom, normalized by maximum) contains a significant jump.

which indicates that the kinematics have not been smoothed properly after insertion of the regular wave. Such a discontinuity in wave loading is very undesirable, since it may lead to an unphysical extreme response of one or more of the wind turbine components.

Second, it can be observed that small oscillations are present in the sea surface elevation of the regular wave. This is likely to be caused by a high amplitude of one of the perturbation frequencies in the nonlinear wave model, which is typical when the breaking limits are approached or exceeded. This assessment proves to be true when the breaking limits of a wave are investigated more closely. Theoretically, the highest wave with nondimensional height H_{MAX}/d, according to Fenton's approximation [22] to research performed by Williams [79], is:

$$\frac{H_{\text{MAX}}}{d} = \frac{0.0077829\left(\frac{L}{d}\right)^3 + 0.0095721\left(\frac{L}{d}\right)^2 + 0.141063\left(\frac{L}{d}\right)}{0.0093407\left(\frac{L}{d}\right)^3 + 0.0317567\left(\frac{L}{d}\right)^2 + 0.078834\left(\frac{L}{d}\right) + 1} \tag{B.1}$$

Besides this theoretical breaking limit, which depends on the wave length to water depth ratio L/d, experiments by Nelson [80] have shown that waves in practice break already at $H_{\text{MAX}}/d = 0.55$. This lower practical breaking limit is supported by other research [81] as well. When the breaking limits of Fenton/Wilson and Nelson are plotted together with the wave height of the example wave shown above, one can only conclude from the resulting figure (B.2) that waves of this height is very likely to break. Hence, waves in this region actually require a higher fidelity wave model in which breaking of the sea surface can be tracked.

A final observation on the regular wave in Figure B.1 reveals that the shear force peaks slightly later than the surface elevation. This is unexpected, since the

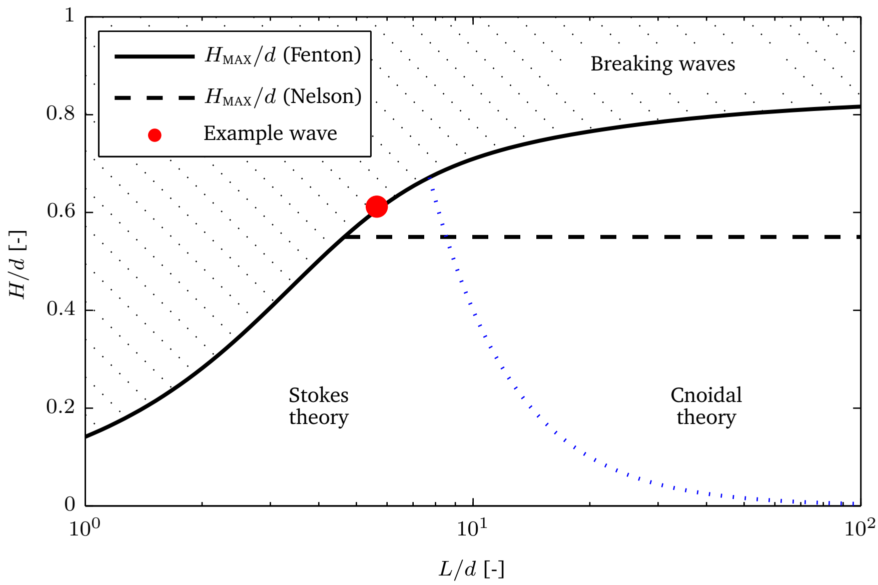

Figure B.2: Diagram showing the breaking limits of regular waves, according to the theoretical approximation by Fenton and experiments by Nelson. The regular deterministic wave from Figure B.1 just exceeds the breaking limit. The blue dotted line indicates the demarcation line between the traditional cnoidal and Stokes theory (see Chapter 2).

acceleration terms in the Morison equation have a 90 degrees phase lead over the velocity terms. When the wave approaches, the horizontal velocities increase until they achieve their maximum at the wave crest, hence the acceleration is positive. The peak of the shear force is therefore expected slightly before the wave crest. This leads to the conclusion that in this wave the acceleration terms have the wrong sign.

B.1.1 Influence of the MacCamy-Fuchs diffraction correction

Although the wrong phase of the acceleration does not significantly influence the magnitude of the maximum bending moment, it does influence the dynamic response of the offshore wind turbine, as shown in Chapter 5. Besides the observations made here, it was shown in Chapter 4 that the wave loads due to the third party waves differ significantly from the loads calculated with the methods used for this thesis. Considering the 180°phase shift in the acceleration terms, an incorrect implementation of the phase lag due to the MacCamy-Fuchs correction for diffraction (Section 2.3.3) may be plausible.

For the monopile geometry and deterministic waves used for this project, the diffraction parameter $(kD/2)$ varies between 0.1 and 0.4, approximately. This

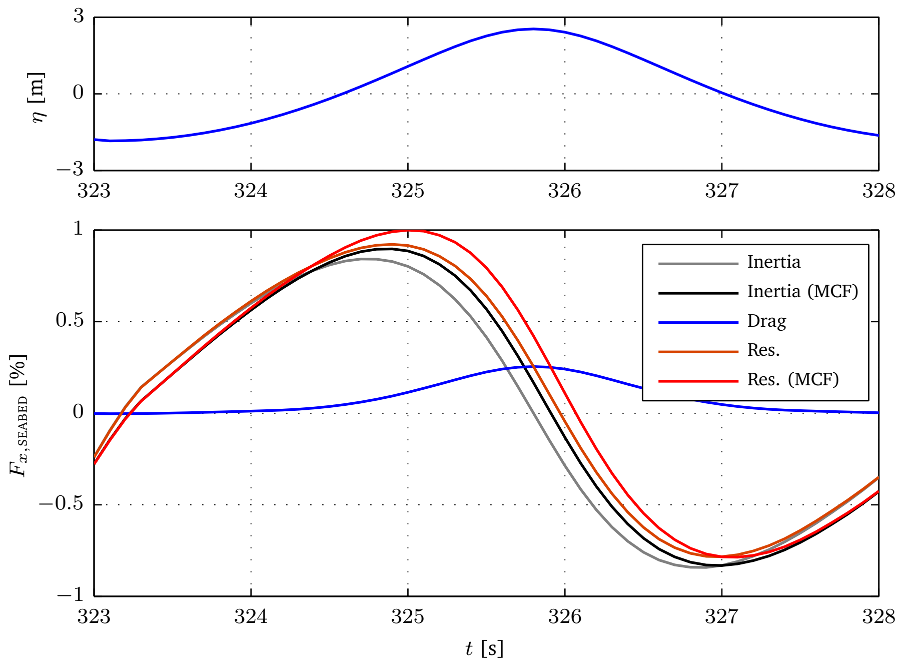

Figure B.3: Influence of MacCamy-Fuchs correction on wave loads due to a deterministic wave. Shown are the inertia and drag contributions to the resultant hydrodynamic force at seabed level, with and without MacCamy-Fuchs correction. Diffraction parameter $(kD/2) \approx 0.4$.

results in a maximum phase lag of the inertia term in the Morison equation of about 7°, which is shown in Figure B.3 for $(k/D) \approx 0.4$. It can be observed that the phase shift of the inertia term has a small influence on the magnitude and the time stamp of the maximum resultant force. Even when the phase lag has been implemented incorrectly by the foundation designer, this does not fully explain the large difference observed in Chapter 4.

A final note has to be made on the MacCamy-Fuchs correction. Since the higher-order corrections are bound waves that are phase-locked on to the primary regular wave, the phase lag that is applied with the MacCamy-Fuchs correction should be based on the primary wave and should be the same for all higher-order Fourier components.

B.2 Nonlinear wave model: Fourier approximation

The wave model that is used to calculate deterministic wave properties is the Fourier approximation method by Fenton [6], which is a nonlinear model for regular waves. As was discussed in Section 2.2.5, the principle behind this method is to add higher-order perturbations to a linear harmonic wave, where the amplitude coefficients of the perturbations are solved numerically. This model is available as an open-source program developed in C++ by Fenton, and therefore only requires a small amount of work to implement. An instruction manual is provided, which aids in setting up the input files and extracting the relevant variables from the output. The formulations of the expressions for the surface elevation and kinematics can be found in the instruction manual [31].

It was observed that the results of the wave loads due to nonlinear regular waves are quite sensitive to the choices made with respect to modeling a steady current. The Fourier method is able to anticipate the Doppler shift due to a steady depth-averaged current. This is convenient when one wants to reproduce a wave of which the wave period was measured in the stationary frame of reference. The Fourier method then corrects the wave length and wave celerity such that in the relative frame of reference, moving with the wave, the kinematics are modeled correctly. The requirement, however, is that the specified wave period represents the apparent period as measured from a stationary position.

For this project, deterministic wave periods are obtained from Metocean data, and this requirement may not be satisfied due to the ambiguity of what wave period is actually specified in the Metocean data. Since the wave length is modified when a current is specified upfront, a wave with a different steepness and hence different kinematics is created than what one would expect based on the properties from Metocean data. Therefore, in this thesis it is assumed that the Metocean data represents the wave properties in the relative frame of reference. As such, the Fourier program will calculate a wave independent of the current, which can be added later vectorially. The Doppler shift can simply be accounted for by modifying the frequency of the wave.

Since specifying a current in the input of the Fourier program has a quite significant influence on the wave steepness and kinematics, this may be an explanation for the large difference with the verified wave loads due to deterministic waves found in Chapter 4. Whether this difference is due to mistakes by the foundation designer, or due to an incorrect implementation of the Fourier program in the developed hydrodynamic load model, is unclear. A more detailed check of the correctness of the implementation and the chosen approach to deal with currents in the Fourier program is therefore recommended.

B.3 Insertion method

As discussed above, the empirical insertion of a deterministic wave into a stochastic wave record needs to be performed carefully to avoid discontinuities in the distributed wave load in time. Therefore, an algorithm was devised to find the best insertion point in a wave record, and to smoothen the transition between stochastic and deterministic wave kinematics. The algorithm consists of three steps:

1. Find best insertion point
2. Create replacement surface elevation
3. Create replacement wave kinematics

In order to create a smooth transition, first a regular cosine wave with phase $-2\pi \leq \phi \leq 2\pi$ is created with the Fourier model, hereafter referred to as the Fourier wave. The phase range between the troughs, from $-\pi$ to π, represents the passage of the deterministic wave, while the half-periods prior to and after the Fourier wave troughs are used for smoothing. Below, the individual steps are described in more detail. It must be mentioned that the method devised here is not based on any physical theory, but provides a more robust way to apply the engineering method of glueing a deterministic wave in a stochastic wave record without user intervention.

B.3.1 Identification of the optimal insertion point

To find the best point in a stochastic wave record to insert the Fourier wave, an objective function is created. A minimization will then return the optimal insertion point. This objective function $f_{insertion}$ comprises two criteria that can be considered as penalty functions, which are evaluated for each local pair of adjacent troughs in the original wave record. This gives:

$$f_{insertion} = f_{\Delta elev} + f_{\Delta period} \tag{B.2}$$

The function $f_{\Delta elev}$ represents the normalized difference between the elevations of the local trough pairs and the Fourier wave. With the trough elevation from MSL defined as $h = -z_{trough}$, the function is defined as:

$$f_{\Delta elev} = \frac{1}{2}\left(\frac{|h_1 + h_2 - 2h_F|}{h_F}\right) K_1 \tag{B.3}$$

where h_1 and h_2 are the elevations of the local pairs of first and second trough, and h_F is the elevation of the Fourier wave trough. The gain K_1 was set to 1. The penalty function for the nondimensional period difference is given as:

$$f_{\Delta period} = \frac{(t_2 - t_1) - T_F}{T_F} K_2 \tag{B.4}$$

where t_1 and t_2 are the time stamps of the local trough pairs and T_F is the Fourier wave period. For the gain K_2, the value of $K_2 = 2$ was found appropriate to yield a good balance between both contributions in the objective function, Eq. B.2.

B.3.2 Replacement surface elevation

With the insertion point determined, a surface elevation can be created that replaces the original surface elevation between -2π and 2π. Since the period between the local trough pair hardly ever is exactly the same as the Fourier wave period, the original surface elevations in the transition ranges $-2\pi \leq \phi \leq -\pi$ and $\pi \leq \phi \leq 2\pi$ are *stretched* in time. This way, the troughs in the stochastic record have the same time stamp as the Fourier wave troughs.

Next, a linear scaling is applied to the stochastic surface elevation η_S, such that it smoothly adapts to the Fourier wave elevation η_F. The replacement surface elevation η_R, including the insertion of the Fourier wave, is given by:

$$\eta_R = \eta_S K_S + \eta_F K_F \tag{B.5}$$

where the gains K_S and K_F are defined as:

$$K_S = \begin{cases} 1 - \frac{1}{\pi}(\phi + \pi) \cdot \frac{h_F}{h_1} & -2\pi \leq \phi < -\pi \\ 0 & -\pi \leq \phi \leq \pi \\ 1 + \frac{1}{\pi}(\phi - \pi) \cdot \frac{h_F}{h_2} & \pi < \phi \leq 2\pi \end{cases} \tag{B.6}$$

$$K_F = \begin{cases} 1 & -\pi \leq \phi \leq \pi \\ 0 & \text{otherwise} \end{cases} \tag{B.7}$$

Here, the ratios h_F/h_1 and h_F/h_2 take care of the appropriate scaling of the original trough elevation to the Fourier wave trough. An example of a deterministic wave inserted in a stochastic record using this method is shown for the surface elevation in Figure B.4.

B.3.3 Replacement wave kinematics

Less straightforward than the replacement of the surface elevation is a smooth transition of the wave kinematics. In the Fourier wave troughs, the velocity profile is maximally negative and the acceleration is zero. To adapt the velocity profile below the replacement surface in the transition regions $-2\pi \leq \phi < -\pi$ and $\pi < \phi \leq 2\pi$ to the velocity profile below the Fourier trough, the following modification is applied to the Fourier wave velocity distribution:

$$u_F(z, \phi) = \begin{cases} u_F(z_c, -\pi) \cdot \frac{-\eta_R(\phi)}{h_F} & -2\pi \leq \phi < -\pi \\ u_F(z, \phi) & -\pi \leq \phi \leq \pi \\ u_F(z_c, \pi) \cdot \frac{-\eta_R(\phi)}{h_F} & \pi < \phi \leq 2\pi \end{cases} \tag{B.8}$$

This means that in the transition region, the same velocity profile as below the Fourier trough is used, of which the magnitude is scaled with the local surface

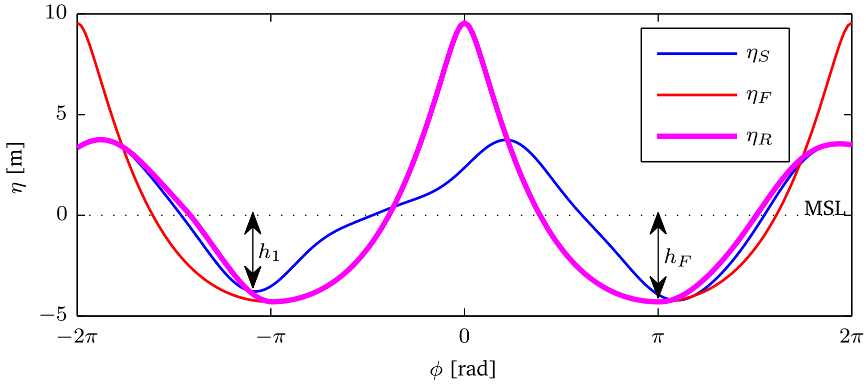

Figure B.4: Insertion of a deterministic wave in a stochastic record. Shown are the surface elevation of the stochastic record η_S, the deterministic Fourier wave η_F and the resulting replacement wave η_R.

elevation of the replacement wave record. The same principle as applied in Wheeler's stretching technique is used to redistribute the velocities on coordinates z_c across the local vertical coordinates z, up to the actual surface. A similar procedure can be applied to the acceleration profile, using the ratio of the gradients of the replacement and Fourier surface elevations instead to account for the $90°$ phase lead of the acceleration term. If the MacCamy-Fuchs correction is used, this should also be taken into account in the phase.

Next, the modified Fourier kinematics can be blended with the original stochastic wave kinematics, using the following linear crossfade relation for the resultant velocity:

$$u_R = u_S K_S + u_F K_F \tag{B.9}$$

where the gains K_S and K_F are defined as:

$$K_S = \begin{cases} -\frac{1}{\pi}(\phi + \pi) & -2\pi \leq \phi < -\pi \\ 0 & -\pi \leq \phi \leq \pi \\ \frac{1}{\pi}(\phi - \pi) & \pi < \phi \leq 2\pi \end{cases} \tag{B.10}$$

$$K_F = 1 - K_S \tag{B.11}$$

Since at certain points in time the elevation difference between stochastic and Fourier wave can be significant, the velocity profiles may need to be extended to the local maximum of both surface elevations. This way, a reduced replacement magnitude near the surface coordinates due to a different amount of submerged z-coordinates, is avoided. The crossfade procedure described here for the velocities, is used for the acceleration terms in the same fashion.

C
Design Load Cases for Response Simulations

In Chapter 4 and 5, the full dynamic response simulation of an offshore wind turbine is discussed. This appendix provides additional detail on the Design Load Cases (DLC) that are used to define (amonst others) the sea environment. These DLCs are described in full detail in the IEC-61400-3 Design Standards [71]. Since a complete overview of all DLCs is far outside the scope of this thesis, only the DLCs that are relevant with respect to the sea enviroment are treated here. As far as the assumptions for determining parameters and models are concerned, the IEC Standards leave some room for judgement by the foundation designer. Since the simulations in this thesis are performed on the wind farm that was used for verification of the reference wave model, the same assumptions and DLC definitions that the foundation designer for this project has used are employed.

C.1 Definition of the Design Load Cases

The response loads that are simulated for each DLC are either analyzed with ultimate or fatigue strength criteria. Each DLC uses a distinct combination of a predefined design situation, wind condition and sea environment. The wave load calculations that are used as input in the BHawC simulations are either uniquely generated for that DLC, or the wave loads of another DLC are used instead. The different DLCs and the corresponding sea environments are tabulated in Table C.1.

C.1.1 Number of wave load files per DLC

In Table C.1, seven distinct DLCs are defined. The design situation describes the operational condition of the wind turbine of each DLC, with the identifier of the DLC specified in the second column. Within a DLC, the number of wind speeds, wave directions and *seeds* define the number of unique wave load files that is to be created for the DLC. If more than one wind speed is simulated, the range of wind speeds is discretized with steps of 1 or 2 m/s. For DLCs 1.x and 2.1, the wind speed is stepped through the wind speed range in which the wind turbine is allowed to produce power. In the parked load cases 6.x, either an extreme or a stepped range of high wind speeds is used.

Due to the secondary steel that is added to the monopile (boat landings, ladders), the support structure is not axisymmetric. This results in a dependency of the Morison force coefficients on wave direction, and hence on the calculated equivalent force coefficients (see Section 2.5.4). In the simulations carried out for this research, the wave directions have been discretized with a 30°stepping, which results in 12 wave sectors. The worst wave direction then refers to the wave sector with the highest force coefficients, which will result in the highest hydrodynamic loads. Out of conservatism, this worst wave sector is usually taken in ultimate load analysis.

To ensure a certain amount of randomness in the simulations, several wave load files called seeds are created for each unique combination of wind speeds and wave directions. In every seed, the significant wave height and peak period are varied within the range of the expected values for the sea state that is applied. With the number of wind speeds, wave directions and seeds given in Table C, in total 2988 wave load files have to be created for a full dynamic response simulation.

C.1.2 Definition of the sea environment

With respect to the sea state, the significant wave height and peak period are related to the wind speed. In the Normal Sea State (NSS), the sea state is based on the long term joint probability distribution of these three parameters, which is usually obtained from site-specific metocean data. The Severe Sea State (SSS) is an extrapolation of the metocean data, such that every combination of significant wave heights and wind speeds has a recurrence period of 50 years. The Extreme Sea State (ESS) is defined by the significant wave height with a recurrence period of 1 year (DLC 6.3) and 50 years (DLC 6.1), where an appropriate peak period is determined accordingly.

The current models that are applied in the simulations are differentiated by their magnitude. The normal current is based on a depth-averaged velocity with a recurrence period of 1 year, while the extreme current has a recurrence period of 50 years. Both models use the same assumptions; the velocity profile is described by a power-law (see Section 2.2.7), the current is in the same direction as the wave propagation and the Doppler shift is ignored. Below deterministic waves, a uniform velocity profile is assumed. Furthermore, DLC 6.4 is simulated without a current.

The water levels that are applied follow the definitions of Section 2.5.3. The properties of the deterministic wave that is inserted, depends on the load case. In DLC 1.6, the severe wave height H_{SWH} is chosen such that the combination of deterministic wave height and mean wind speed has a recurrence period of 50 years. For the deterministic waves in the ESS load cases, the extreme wave height H_{EWH} is used. In DLC 6.1 this means using the wave height with a recurrence period of 50 years, H_{50}, whereas in DLC 6.3 the wave height with a 1 year return period, H_1, shall be inserted.

Table C.1: Definition of the Design Load Cases with a unique sea state.

Design Situation	DLC	Wind Speed [m/s]	Wave Dir.	No. of Seeds	Sea State	Current Model	Water Level	Determ. Wave	Type of Analysis
Power Production (1)	1.2	4 - 25 (Step=1)	All	9	NSS	Normal	MSL	-	Fatigue
	1.3		Worst	6	NSS	Normal	MSL	-	Ultimate
	1.6		Worst	6	SSS	Extreme	HAT	H_{SWH}	Ultimate
Power Production + Fault Occurence (2)	2.1	4 - 25 (Step=1)	Worst	12	NSS	Normal	MSL	-	Ultimate
Parked (6) (standing still / idling)	6.1	44	Worst	6	ESS	Extreme	HSWL	H_{50}	Ultimate
	6.3	31	Worst	6	ESS	Extreme	HSWL	H_1	Ultimate
	6.4	26 - 36 (Step=2)	Worst	6	NSS	-	HAT	-	Fatigue

Bibliography

[1] B. Erdogan, Y. Mehmet, and S. Abdulkadir, "Offshore wind power development in Europe and its comparison with onshore counterpart," *Renewable and Sustainable Energy Reviews*, vol. 15, no. 2, pp. 905–915, 2011.

[2] S. P. Breton and G. Moe, "Status, plans and technologies for offshore wind turbines in Europe and North America," *Renewable Energy*, vol. 34, no. 3, pp. 646–654, 2009.

[3] J. R. Morison, M. P. O'Brien, J. W. Johnson, S. A. Schaaf, *et al.*, "The force exerted by surface waves on piles," *Journal of Petroleum Technology*, vol. 2, no. 5, pp. 149–154, 1950.

[4] G. B. Airy, "Tides and waves," *Encyclopaedia Metropolitana*, 1845.

[5] J. D. Wheeler, "Methods for calculating forces produced on piles in irregular waves," *Journal of Petroleum Technology*, vol. 1, pp. 1–2, 1970.

[6] J. D. Fenton, "Numerical methods for nonlinear waves," *Advances in coastal and ocean engineering*, vol. 5, pp. 241–324, 1999.

[7] L. H. Holthuijsen, *Waves in oceanic and coastal waters*. Cambridge University Press, 2007.

[8] J. H. Vugts, "The offshore wave and current environment and hydrodynamic loading," tech. rep., Delft University of Technology, 2002.

[9] J. M. J. Journee and W. W. Massie, "Offshore hydromechanics," tech. rep., Delft University of Technology, 2001.

[10] K. Torsethaugen, "Model for a doubly peaked wave spectrum," *SINTEF report STF22 A*, vol. 96204, 1996.

[11] Det Norske Veritas (DNV), "Recommended practice - DNV-RP-C205 – Environmental conditions and environmental loads," *Høvik, Norway*, 2007.

[12] S. Gran, *A course in ocean engineering*. Elsevier, 1992.

[13] T. Sarpkaya, *Wave forces on offshore structures*. Cambridge University Press, 2010.

[14] O. T. Gudmestad, "Measured and predicted deep water wave kinematics in regular and irregular seas," *Marine Structures*, vol. 6, no. 1, pp. 1–73, 1993.

[15] O. T. Gudmestad and S. T. Haver, "Uncertainties in prediction of wave kinematics in irregular waves," *Wave Kinematics and Environmental Forces*, 1993.

[16] G. Rodenbusch and G. Forristall, "An empirical model for random directional wave kinematics near the free surface," in *Offshore Technology Conference*, 1986.

[17] S. K. Chakrabarti, "Discussion of dynamics of single point mooring in deep water," *Journal of the Waterways, Harbors and Coastal Engineering Division*, vol. 97, no. 3, pp. 588–590, 1971.

[18] O. T. Gudmestad and J. J. Connor, "Engineering approximations to nonlinear deepwater waves," *Applied ocean research*, vol. 8, no. 2, pp. 76–88, 1986.

[19] O. T. Gudmestad, "A new approach for estimating irregular deep water wave kinematics," *Applied Ocean Research*, vol. 12, no. 1, pp. 19–24, 1990.

[20] G. Z. Forristall, "Irregular wave kinematics from a kinematic boundary condition fit (kbcf)," *Applied ocean research*, vol. 7, no. 4, pp. 202–212, 1985.

[21] S. H. Gjøsund, "A lagrangian model for irregular waves and wave kinematics," *Journal of Offshore Mechanics and Arctic Engineering*, vol. 125, p. 94, 2003.

[22] J. D. Fenton, "Nonlinear wave theories," *The Sea*, vol. 9, no. 1, pp. 3–25, 1990.

[23] P. Goodwin, R. J. Thieke, R. J. Westberg Jr, *et al.*, "Application of stokes, cnoidal, and Fourier wave theories," *Journal of Waterway, Port, Coastal and Ocean Engineering*, vol. 113, p. 565, 1987.

[24] J. Fenton, "A fifth-order stokes theory for steady waves," *Journal of Waterway, Port, Coastal and Ocean Engineering*, vol. 111, no. 2, pp. 216–234, 1985.

[25] J. D. Fenton, "A high-order cnoidal wave theory," *J. Fluid Mech*, vol. 94, no. part 1, pp. 129–161, 1979.

[26] R. Mirshak, "An overview of jacobian elliptical functions,"

[27] J. E. Chappelear, "Direct numerical calculation of wave properties," *Journal of Geophysical Research*, vol. 66, no. 2, pp. 501–508, 1961.

[28] R. G. Dean, "Stream function representation of nonlinear ocean waves," *Journal of Geophysical Research*, vol. 70, no. 18, pp. 4561–4572, 1965.

[29] M. M. Rienecker and J. D. Fenton, "Fourier approximation method for steady water waves," *Journal of Fluid Mechanics*, vol. 104, pp. 119–37, 1981.

[30] J. D. Fenton, "The numerical solution of steady water wave problems," *Computers & Geosciences*, vol. 14, no. 3, pp. 357–368, 1988.

[31] J. D. Fenton, "Use of the program fourier for steady waves," 2010.

[32] J. N. Sharma and R. G. Dean, "Second-order directional seas and associated wave forces," *Old SPE Journal*, vol. 21, no. 1, pp. 129–140, 1981.

[33] G. Z. Forristall, "Wave crest distributions: Observations and second-order theory," *Journal of Physical Oceanography*, vol. 30, no. 8, pp. 1931–1943, 2000.

[34] K. Trulsen, O. T. Gudmestad, and M. G. Velarde, "The nonlinear Schrödinger method for water wave kinematics on finite depth," *Wave motion*, vol. 33, no. 4, pp. 379–395, 2001.

[35] J. Zhang, J. Yang, J. Wen, I. Prislin, and K. Hong, "Deterministic wave model for short-crested ocean waves: Part I. Theory and numerical scheme," *applied ocean Research*, vol. 21, no. 4, pp. 167–188, 1999.

[36] J. Zhang and W. K. Melville, "Evolution of weakly nonlinear short waves riding on long gravity waves," *Journal of Fluid Mechanics*, vol. 214, no. 1, pp. 321–346, 1990.

[37] J. Zhang, L. Chen, M. Ye, and R. E. Randall, "Hybrid wave model for unidirectional irregular waves: Part I. Theory and numerical scheme," *Applied Ocean Research*, vol. 18, no. 2, pp. 77–92, 1996.

[38] A. T. Couch and J. P. Conte, "Field verification of linear and nonlinear hybrid wave models for offshore tower response prediction," *Transactions of the ASME. Journal of Offshore Mechanics and Arctic*, vol. 119, no. 3, pp. 158–165, 1997.

[39] I. Prislin, J. Zhang, and R. J. Seymour, "Deterministic decomposition of deep water short-crested irregular gravity waves," *Journal of geophysical research*, vol. 102, no. C6, pp. 12677–12, 1997.

[40] P. Agarwal and L. Manuel, "Incorporating irregular nonlinear waves in coupled simulation and reliability studies of offshore wind turbines," *Applied Ocean Research*, 2011.

[41] G. Z. Forristall, "Nonlinear wave calculations for engineering applications," *Journal of Offshore Mechanics and Arctic Engineering*, vol. 124, p. 28, 2002.

[42] T. B. Johannessen, "Calculations of kinematics underneath measured time histories of steep water waves," *Applied Ocean Research*, vol. 32, no. 4, pp. 391–403, 2010.

[43] J. K. Longridge, R. E. Randall, and J. Zhang, "Comparison of experimental irregular water wave elevation and kinematic data with new hybrid wave model predictions," *Ocean engineering*, vol. 23, no. 4, pp. 277–307, 1996.

[44] N. J. Tarp-Johansen, K. Agyriadis, H. Carstens, J. v. d. Tempel, T. Camp, P. W. Cheng, and P. Passon, "Review of modelling approaches for irregular, non-linear wave loading on offshore wind turbines and their relevance for future designs,"

[45] P. A. Madsen, H. B. Bingham, and H. Liu, "A new Boussinesq method for fully nonlinear waves from shallow to deep water," *Journal of Fluid Mechanics*, vol. 462, no. 1, pp. 1–30, 2002.

[46] V. R. Gopala and B. G. M. van Wachem, "Volume of fluid methods for immiscible-fluid and free-surface flows," *Chemical Engineering Journal*, vol. 141, no. 1, pp. 204–221, 2008.

[47] S. B. Pope, *Turbulent flows*. Cambridge Univ Pr, 2000.

[48] M. I. Gerritsma, "Computational fluid dynamics - incompressible flows," tech. rep., Delft University of Technology, 2002.

[49] A. P. Engsig-Karup, H. B. Bingham, and O. Lindberg, "An efficient flexible-order model for 3D nonlinear water waves," *Journal of Computational Physics*, vol. 228, no. 6, pp. 2100–2118, 2009.

[50] A. P. Engsig-Karup, M. G. Madsen, and S. L. Glimberg, "On a fast GPU-accelerated massively parallel method for fully nonlinear water wave computations," 2011.

[51] J. T. Kirby and T. M. Chen, "Surface waves on vertically sheared flows: approximate dispersion relations," *Journal of Geophysical Research*, vol. 94, no. C1, pp. 1013–1027, 1989.

[52] O. T. Gudmestad and D. T. Karunakaran, "Wave current interaction," in *Environmental Forces on Offshore Structures and Their Predictions: Proceedings of an international conference*, 1990.

[53] J. F. Wilson, B. J. Muga, and L. C. Reese, *Dynamics of offshore structures*. Wiley, 2003.

[54] A. R. Henderson, M. B. Zaaijer, and T. R. Camp, "Hydrodynamic loading on offshore wind turbines," in *Offshore Wind Energy in the Mediterranean and Other European Seas Conference [OWEMES]*, 2003.

[55] L. L. M. Veldhuis, "Aircraft aerodynamics primer," tech. rep., Delft University of Technology, 2010.

[56] H. Schlichting, K. Gersten, and K. Gersten, *Boundary-layer theory*. Springer Verlag, 2000.

[57] T. Sarpkaya, "Vortex shedding and resistance in harmonic flow about smooth and rough circular cylinders at high Reynolds numbers," tech. rep., DTIC Document, 1976.

[58] S. K. Chakrabarti, *Handbook of offshore engineering*, vol. 1. Elsevier, 2005.

[59] S. K. Chakrabarti, *The theory and practice of hydrodynamics and vibration*, vol. 20. World Scientific Pub Co Inc, 2002.

[60] N. Heaf, "The effect of marine growth on the performance of fixed offshore platforms in the North Sea," in *Offshore Technology Conference*, 1979.

[61] W. Shi, H. C. Park, C. W. Chung, and Y. C. Kim, "Marine growth effect on the vibration characteristics of offshore wind turbine with jacket foundation," *Applied Mechanics and Materials*, vol. 84, pp. 691–696, 2011.

[62] T. Sarpkaya, "In-line and transverse forces on smooth and sand-roughened cylinders in oscillatory flow at high Reynolds numbers," tech. rep., DTIC Document, 1976.

[63] I. Jusoh and J. Wolfram, "Effects of marine growth and hydrodynamic loading on offshore structures," *Jurnal Mekanikal*, vol. 1, no. 1, pp. 77–96, 1996.

[64] R. C. MacCamy, "Wave forces on piles: A diffraction theory.," tech. rep., DTIC Document, 1954.

[65] N. D. P. Barltrop, A. J. Adams, and M. G. Hallam, *Dynamics of fixed marine structures*, vol. 8. Butterworth-Heinemann Oxford, 1991.

[66] J. van der Tempel and D. P. Molenaar, "Wind turbine structural dynamics – a review of the principles for modern power generation, onshore and offshore," *Wind Engineering*, vol. 26, no. 4, pp. 211–222, 2002.

[67] J. Van Der Tempel, "Design of support structures for offshore wind turbines," 2006.

[68] R. P. L. Nijssen, M. B. Zaaijer, W. Bierbooms, G. A. M. Van Kuik, D. R. V. Van Delft, and T. van Holten, "The application of scaling rules in up-scaling and marinisation of a wind turbine," in *Offshore Wind Energy Special Topic Conference, Brussels, Belgium*, 2001.

[69] T. Fischer, W. Vries, P. Rainey, B. Schmidt, K. Argyriadis, and M. Kühn, "Offshore support structure optimization by means of integrated design and controls," *Wind Energy*, 2011.

[70] W. Versteijlen, A. Metrikine, J. Hoving, E. Smidt, and W. De Vries, "Estimation of the vibration decrement of an offshore wind turbine support structure caused by its interaction with soil," *Master's thesis. Technical University of Delft*, 2011.

[71] International Electrotechnical Commission *et al.*, "IEC 61400-3," *Wind Turbines – Part 3: Design Requirements for Offshore Wind Turbines*, 2009.

[72] Det Norske Veritas (DNV), "Offshore Standard - DNV-OS-J101 – Design of offshore wind turbine structures," *Høvik, Norway*, 2004.

[73] T. J. Ypma, "Historical development of the Newton-Raphson method," *SIAM review*, pp. 531–551, 1995.

[74] P. Agarwal, *Structural reliability of offshore wind turbines*. ProQuest, 2008.

[75] J. W. Cooley and J. W. Tukey, "An algorithm for the machine calculation of complex Fourier series," *Math. Comput*, vol. 19, no. 90, pp. 297–301, 1965.

[76] R. G. Lyons, *Understanding digital signal processing*. Prentice Hall PTR, 2004.

[77] H. Veldkamp and J. Van Der Tempel, "Influence of wave modelling on the prediction of fatigue for offshore wind turbines," *Wind Energy*, vol. 8, no. 1, pp. 49–65, 2005.

[78] K. Mittendorf, M. Kohlmeier, A. Habbar, and W. Zielke, "Influence of irregular wave kinematics description on fatigue load analysis of offshore wind energy structures," in *Proceedings of DEWEK*, pp. 22–23, 2006.

[79] J. M. Williams, "Limiting gravity waves in water of finite depth," *Philosophical Transactions of the Royal Society of London. Series A, Mathematical and Physical Sciences*, vol. 302, no. 1466, pp. 139–188, 1981.

[80] R. C. Nelson, "Design wave heights on very mild slopes: an experimental study," *Transactions of the Institution of Engineers, Australia. Civil engineering*, vol. 29, no. 3, pp. 157–161, 1987.

[81] B. Le Mehaute, D. Divoky, and A. Lin, "Shallow water waves: a comparison of theories and experiments," in *Proceedings, 11th Conference on Coastal Engineering, American Society of Civil Engineers, London*, pp. 86–107, 1968.

Definitions

Airy / Linear wave theory: Classic analytical method to find expressions for the wave kinematics below a given sea surface, up to mean sea level. Assumes that frequency components do not interact, and that the wave steepness and amplitude are small. Therefore, stretching techniques are required to obtain wave kinematics up to the actual surface.

Apparent frequency: Wave frequency observed in the stationary frame of reference, as experienced by a support structure when a wave travels on a steady current.

Crest: The local maximum of a wave. If the sea surface is highly irregular, wave crests may occur below the mean sea level as well.

Deterministic wave: An extreme wave with a prescribed wave height and period, which is modeled by a separate (regular) wave model.

Doppler shift: Wave frequency shift between relative and apparent frame of reference, when a wave is traveling on a steady current.

Fatigue damage: Degradation of a material due to long-term cyclic loading, which may eventually lead to failure.

Irregular wave: Periodic wave that consists of many frequency components with unique amplitudes and phases. Since the amplitudes and phases are drawn from frequency dependent probability distributions, the wave irregular record is stochastic.

Nonlinear effects: Interaction effects between wave frequency components due to a relatively small water depth. This results in a nonharmonic wave shape. In this case, the assumptions in linear wave theory are not valid and lead to errors.

Peak period (T_P): Period at which the peak of the wave spectrum is located.

Regular wave: Periodic (harmonic) wave with a unique frequency.

Relative / Intrinsic frequency: Wave frequency in the relative frame of reference, as experienced by an observer traveling on a steady current. In this frame of reference, linear wave theory is applied.

Significant wave height (H_S): The mean of the highest one-third of waves occuring in a wave record. The significant wave height corresponds well to the estimation of the mean wave height by a human observer.

Trough: Local minimum of a wave. Similarly as for crests, wave troughs may locally occur above the mean sea level if the sea surface is highly irregular.

Variance density / Wave spectrum: A statistical representation of ocean waves, also known as the wave energy spectrum. The variance of the wave amplitude is plotted as a function of the wave frequency. As the variance is proportional to the wave energy, the variance density spectrum can be used to determine which wave frequencies are the most significant.

Wave height: Local elevation difference between two consecutive down- or upward crossings of the mean sea level.

Wheeler stretching: Technique to redistribute the wave kinematics from linear wave theory over the actual water column below the sea surface, at each time step.

Zero-crossing wave period (T_Z): The time passed between two consecutive down- or upcrossings of the mean sea level by the sea surface elevation.